Chemical Science

ROYAL SOCIETY OF CHEMISTRY

EDGE ARTICLE

View Article Online
View Journal | View Issue

Cite this: *Chem. Sci.*, 2024, **15**, 14273

All publication charges for this article have been paid for by the Royal Society of Chemistry

Received 10th June 2024
Accepted 5th August 2024

DOI: 10.1039/d4sc03788j

rsc.li/chemical-science

Structure–function relationships in pure archaeal bipolar tetraether lipids†

Ahanjit Bhattacharya, [ab] Isaac D. Falk,[a] Frank R. Moss III, [c] Thomas M. Weiss,[d] Khoi N. Tran, [a] Noah Z. Burns *[a] and Steven G. Boxer *[a]

Archaeal bipolar tetraether lipids (BTLs) are among the most unusual lipids occurring in nature because of their presumed ability to span the entire membrane to form a monolayer structure. It is believed that because of their unique structural organization and chemical stability, BTLs offer extraordinary adaptation to archaea to thrive in the most extreme milieus. BTLs have also received considerable attention for development of novel membrane-based materials. Despite their fundamental biological significance and biotechnological interests, prior studies on pure BTLs are limited because of the difficulty to extract them in pure form from natural sources or to synthesize them chemically. Here we have utilized chemical synthesis to enable in-depth biophysical investigations on a series of chemically pure glycerol dialkyl glycerol tetraether (GDGT) lipids. The lipids self-assemble to form membrane-bound vesicles encapsulating polar molecules in aqueous media, and reconstitute a functional integral membrane protein. Structural properties of the membranes were characterized *via* small-angle X-ray scattering (SAXS) and cryogenic electron microscopy (cryo-EM). SAXS studies on bulk aqueous dispersions of GDGT lipids over 10–90 °C revealed lamellar and non-lamellar phases and their transitions. Next we asked whether vesicles overwhelmingly composed of a single GDGT species can undergo fusion as it is difficult to conceptualize such behavior with the assumption that such membranes have a monolayer structure. Interestingly, we observed that GDGT vesicles undergo fusion with influenza virus with lipid mixing kinetics comparable to that with vesicles composed of monopolar phospholipids. Our results suggest that GDGT membranes may consist of regions with a bilayer structure or form bilayer structures transiently which facilitate fusion and thus offer insight into how archaea may perform important physiological functions that require dynamical membrane behavior.

Introduction

Archaea are an enigmatic group of prokaryotic organisms. Originally thought to be extremophiles, archaea have been found in every realm of the biosphere including the human microbiome.[1] Archaea constitute ~1.3% of the total biomass on the Earth,[2] yet they have remained quite underexplored. While archaea resemble bacteria in certain superficial ways, fundamental differences in their biochemistry led to their classification as a separate domain of life. For instance, archaeal lipids differ significantly from the lipids found in bacteria (and eukaryotes) in terms of structural features, such as, absolute stereochemistry of the glycerol moiety, and the nature of the hydrocarbon chains and their linkages to the same.[3,4] These distinctions between the lipids of archaea and bacteria (and eukarya) form the basis of a dichotomy known as the "lipid divide" (Fig. 1A).[5] In archaeal lipids, the hydrocarbon chains have multiple methyl branches and are of isoprenoid origin – lacking any unsaturation in most cases. Their hydrocarbon chains are connected to the *sn*-glycerol-1-phosphate backbone *via* ether linkages. In bacterial lipids, the hydrocarbon chains are fatty acid-based, contain various degrees of unsaturation, and the hydrocarbon chains are connected to the *sn*-glycerol-3-phosphate backbone through ester linkages. Typical lack of unsaturation and the presence of ether linkages make the archaeal lipids extremely stable to aerial oxidation and hydrolysis respectively. Due to this exceptional chemical stability, archaeal lipids serve as excellent biomarkers for biogeochemical and climate studies.[6]

Remarkably, a major class of archaeal lipids has a bipolar structure – which is analogous to two monopolar lipids covalently joined at the ends of their hydrocarbon tails. Bipolar

[a]*Department of Chemistry, Stanford University, Stanford, CA 94305, USA. E-mail: sboxer@stanford.edu; nburns@stanford.edu*

[b]*Stanford Center for Innovation in Global Health, Stanford University, Stanford, CA 94305, USA*

[c]*Linac Coherent Light Source, SLAC National Accelerator Laboratory, Menlo Park, CA 94025, USA*

[d]*Stanford Synchrotron Radiation Lightsource, SLAC National Accelerator Laboratory, Menlo Park, CA 94025, USA*

† Electronic supplementary information (ESI) available. See DOI: https://doi.org/10.1039/d4sc03788j

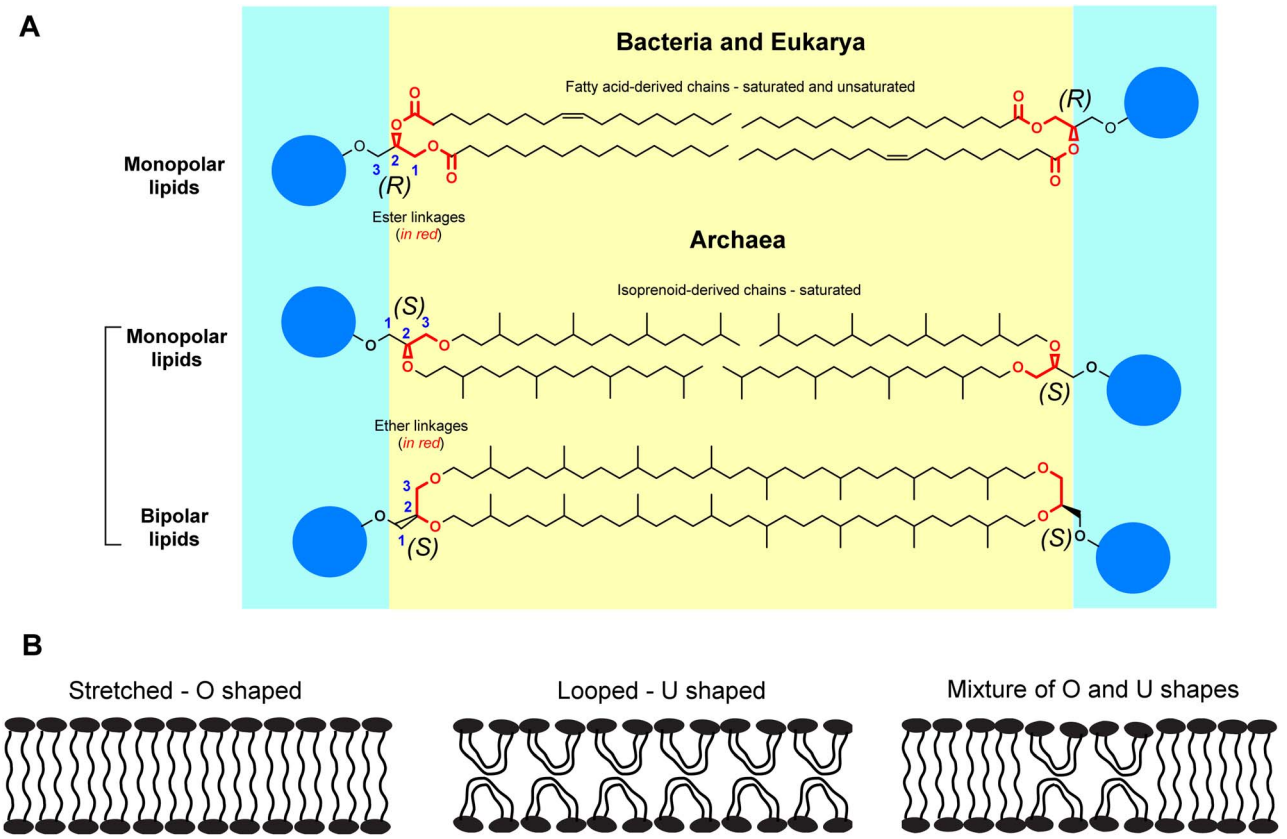

Fig. 1 Structure of GDGT lipids. (A) Schematic diagram illustrating the concept of the "lipid divide" between bacterial/eukaryotic and archaeal lipids. The carbons on glycerol moieties are marked (1–3) according to stereochemical numbering (*sn*) convention. (*R*) and (*S*) denote the absolute stereochemistries of the glycerol moieties. The blue spheres denote generic polar headgroups. For simplicity, the stereochemistries of the branched chains are not shown. (B) Three possibilities of shapes adopted by archaeal bipolar tetraether lipids in a membrane.

lipids render archaeal membranes mechanically stable and impermeable even at high temperatures and at highly acidic pH.[7,8] Although bipolar lipids are found in some bacteria, those are fatty acid-derived, and usually do not constitute the major lipid species in a membrane.[9] Glycerol dialkyl glycerol tetraethers (GDGT) are one of the primary bipolar tetraether lipids (BTLs) found in archaea. Thermoacidophilic archaea possess GDGTs alongside other BTLs while methanogenic archaea possess GDGTs alongside monopolar lipids.[10]

A wealth of information on bacterial and eukaryotic membrane biology has been obtained from biophysical studies on model phospholipid membranes. Similarly, fundamental understanding of structure–function relationships in GDGTs through biophysical studies can further our understanding of the membrane-based cellular processes of archaea. For example, the bipolar nature of the GDGTs gives rise to the question of how these molecules are organized within a membrane and how such organization influences membrane function? Three types of limiting molecular arrangements can be imagined (Fig. 1B): (1) stretched – the lipid molecules are O-shaped and span the entire width of the membrane to form a monolayer; (2) looped – the lipid molecules are bent (*i.e.*, U-shaped) at the hydrocarbon region so that the two headgroups face the same side of the membrane, and the membrane more closely resembles a bilayer; and (3) mixed – where both O- and U-shaped lipids coexist. There is considerable evidence that suggests that a majority of the lipids occur in a stretched conformation. For instance, in contrast to bilayer membranes, freeze-fracture electron microscopy studies on crude archaeal tetraether lipid vesicles have revealed the absence of a preferential fracture plane, which can be explained by considering that the lipids adopt a stretched conformation.[11–13] Although there is a report mentioning exclusive formation of U-shaped bilayers of crude GDGTs on a solid substrate *via* transfer of Langmuir films,[14] evidence of such structures in biological membranes or model vesicles is lacking. The possibility of a small percentage of U-shaped lipids coexisting with O-shaped lipids has been speculated.[15,16] Nevertheless, functional evidence of the presence of such structures in compositionally well-defined GDGT systems is lacking.

Unlike bacterial or eukaryotic lipids, the inaccessibility of pure archaeal BTLs such as GDGTs poses a roadblock to comprehensive biophysical studies which typically require many milligrams of lipids. Moreover, access to pure archaeal BTL standards will facilitate discovery of archaeal lipids biosynthetic enzymes and their mechanistic studies – an area where fundamental understanding has started to deepen only recently.[17,18] Although a few model monopolar archaeal lipids in

the form of ester- or ether-linked diphytan(o)yl phospholipids are commercially available, pure GDGT lipids are difficult to access. Also, the presence of multiple stereocentres makes these lipids challenging to synthesize chemically. To date, no GDGT lipids can be purchased from commercial vendors in pure form. Therefore, most biophysical studies until now have been performed on crude BTL extracts[19–23] or model bipolar lipids.[24–29] There are a few reports of semisynthetic approaches where headgroups were installed onto a heterogeneous mixture of core GDGTs extracted from microbial cultures.[30,31] Only a handful of examples exist where pure species of polar GDGT lipids have been accessed *via* total synthetic approaches.[32–34] In addition, a few pure hemi-macrocyclic tetraether lipids were previously reported which differed in molecular architecture as compared to the natural macrocyclic counterparts.[24,27] Also, the previous works were primarily focused at advancing the synthetic methodology and not for carrying out comprehensive biophysical studies on those lipids. In this work we took advantage of synthetic chemistry to generate a series of four parallel GDGT-0 lipids in multi-milligram quantities (Fig. 2). Among these, two lipids are symmetric (**P2** and **PG2**) and two are unsymmetric (**P1Glc** and **PG1Glc**) in terms of head group composition. The headgroups (phosphate, phosphoglycerol, glucose) that are present in the GDGTs in this study can be found naturally although symmetric combinations of those headgroups on an individual lipid are not yet reported to occur naturally. We studied the self-assembly behaviour of these GDGT lipids in various aqueous buffers and identified conditions in which membrane-bound giant vesicles are formed. We characterized the structural properties of GDGT membranes using small-angle X-ray scattering (SAXS), and cryogenic electron microscopy. We used SAXS also to characterize the transitions between various mesophases under a range of conditions of ionic strengths, divalent cation, and pH over a wide temperature range. Interestingly, we identified non-lamellar phases such as hexagonal and cubic phases under many conditions which inspired us to explore whether they have any functional implications, especially in processes like membrane fusion which are thought to proceed through non-lamellar intermediates. Indeed, we found that membranes composed of GDGT lipids undergo facile acidic pH-induced fusion with influenza-virus. To the best of our knowledge, this is the first demonstration of membrane fusion of compositionally well-defined macrocyclic BTLs. Our results provide mechanistic insight into how archaeal membranes undergo fundamental dynamical processes such as fusion.

Experimental section

Preparation of buffers

The following buffers were used and the osmolalities were measured using an Advanced Instruments Model 3320 osmometer:

Tris buffer: 50 mM tris, pH 7.5. Osmolality: 88 mOsmol kg^{-1}.

HB buffer: 20 mM HEPES–Na, 150 mM NaCl, pH 7.2. Osmolality: 316 mOsmol kg^{-1}.

Vesicle buffer: 10 mM Na–phosphate, 90 mM sodium citrate, and 150 mM NaCl (pH 7.4). Osmolality: 545 mOsmol kg^{-1}.

Fusion buffer: 10 mM Na–phosphate, 90 mM sodium citrate, and 150 mM NaCl (pH 5.1). Osmolality: 510 mOsmol kg^{-1}.

Optical microscopy

Fluorescence images were acquired with a Nikon Ti–U microscope using a 100× oil immersion apochromat TIRF objective (NA = 1.49) (Nikon Instruments, Melville, NY). A Spectra-X LED Light Engine (Lumencor, Beaverton, OR) was used for illumination, and an Andor iXon 897 EMCCD camera (Andor Technologies, Belfast, UK) with 16 bit image settings. Images were captured with Metamorph software version 7.10.4 (Molecular Devices, Sunnyvale, CA).

Negative-staining transmission electron microscopy (TEM)

Formvar-coated Cu grids (300 mesh, Catalog #FCF300-Cu, Electron Microscopy Sciences) were glow-discharged using a Denton BenchTop™ Turbo setup and used freshly. 5 μL of a vesicle sample was added to formvar-coated Cu grid surface and allowed to sit for 3 min. The grids were washed by touching the surface of 2 drops of Milli-Q placed on a parafilm sheet. 3 drops of 1% uranyl acetate in ultrapure water were then added

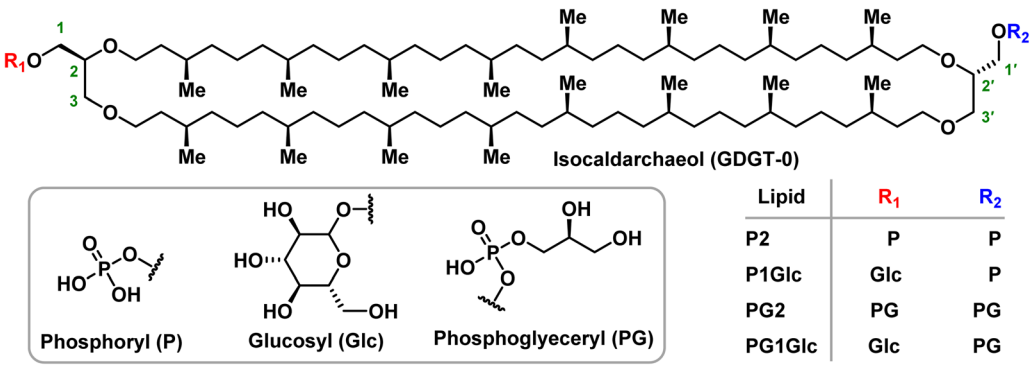

Lipid	R_1	R_2
P2	P	P
P1Glc	Glc	P
PG2	PG	PG
PG1Glc	Glc	PG

Fig. 2 Structures of the GDGT lipids described in this study. The carbons on glycerol moieties are marked (1–3) according to stereochemical numbering (*sn*) convention. It is notable that in isocaldarcheaol, the isopranoid chains are linked in a parallel fashion (2 → 2′ and 3 → 3′). The glucosyl derivatives were synthesized as mixtures of anomers.

to the grid and the 3rd drop was allowed to sit on the grid for 1 min. Afterward, the excess staining solution was blotted into a filter paper. The grids were dried in air. Finally, the grids were imaged on a JEOL JEM-1400 microscope equipped with a Gatan OneView (4k × 4k resolution) camera.

Expression, purification, and reconstitution of photosynthetic reaction centres (RCs) in GDGT membranes

Rhodobacter spheroides RCs (M252V mutant which does not assemble with Q_A) were isolated as previously described.[35] The protein was stored in 10 mM tris (pH 8.0), containing 0.03% (w/v) LDAO. For reconstitution into vesicles, detergent removal method was used. Briefly, a film was prepared in a glass vial by evaporating solvents from 80 μL of 5 mg mL^{-1} solution of **PG2** (or **PG1Glc**) in 1 : 1 $CHCl_3$: MeOH. The vial was kept in the desiccator for 12 h. The film was hydrated by gently tapping with 400 μL of a solution consisting of 10 mM tris (pH 8.0), 30 mM octyl glucoside, 0.26 mM LDAO, and 6 μM RC. The protein to GDGT lipid ratio was about 1 : 100. The lipid/detergent/protein mixture was added to 18 mg of pre-cleaned wet BioBeads SM-2 resin (soaked in Milli-Q water) and allowed to tumble for 30 min at RT. Afterwards, the solution was separated from the beads and taken in a 10 kDa MWCO dialysis cassette. Dialysis was carried out against 10 mM tris buffer (pH 8.0) for 48 h with 2 changes of buffer in between and a clear light purple dispersion is collected. No residual detergents were detected by mass spectrometry. transient (fs ps^{-1}) absorption spectroscopy measurements for RCs shown in Fig. S3† were obtained in the laboratory of Professor Dewey Holten and Christine Kirmaier by Dr Kaitlin Faries at Washington University using previously described methods. We are indebted to them for providing this data.

Surface pressure-area isotherms

Surface pressure-area isotherms of monomolecular layers were recorded at room temperature (22 °C) using a KSV NIMA KN 2002 (Biolin Scientific) Langmuir trough equipped with a Teflon trough (243 cm^2 or 555 cm^2) and symmetric delrin barriers. A Wilhelmy plate made of a 30 mm × 14 mm piece of Whatman #1 filter paper was used to monitor the surface pressure. At first, the trough surface was rinsed with methanol. Next, Milli-Q water was used to thoroughly clean the trough. Typically, a solution of the lipids of known concentration in chloroform (or 9 : 1 chloroform : methanol) was slowly added dropwise onto the surface of the water using a glass microsyringe. The solvent was allowed to evaporate for at least 20 min. The barriers were then compressed at a rate of 10 mm min^{-1} and pressure-area isotherms were recorded.

Small-angle X-ray scattering (SAXS)

SAXS data were collected at the Beamline 4-2 of Stanford Synchrotron Radiation Lightsource. The distance between the sample and the detector (Pilatus3 X 1 M) was 1.2 m and the energy of the X-rays was 11 keV (λ = 1.127 Å). Momentum transfer (q) was measured over a range of 0.01–0.75 $Å^{-1}$, where q is modulus of the scattering vector defined as follows:

$$q = \frac{4\pi \sin\theta}{\lambda}$$

where θ = scattering angle, λ = wavelength of the X-rays.

Two kinds of experiments were performed:

(1) Scattering from unilamellar vesicles. Small unilamellar vesicles of **P2**, **PG2**, and **PG1Glc** were prepared by extruding a multilamellar dispersion in tris buffer through a 50 nm polycarbonate membrane filter. In the case of **P1Glc**, the lipid dispersion contained a significant amount of insoluble aggregates which could not be fully dispersed by bath sonication and those stuck to the membrane filters during extrusion. Therefore, the dispersion was subject to probe ultrasonication which helped to break down the larger aggregates. ~30 μL volumes of the vesicle dispersions were taken in 0.2 mL microtubes and loaded onto an automated sample loader at the beamline. Samples were exposed for a variable time (1 s or 2 s) and variable number of scans (24–50) were taken depending on the concentration of the lipids. Each sample was measured after storing at room temperature for up to a day and identical scattering profiles were obtained. Details of the SAXS data fitting is provided in the ESI† ("Fitting of SAXS data from unilamellar vesicles" section).

(2) Scattering from bulk dispersions. In these experiments, a thin film of a GDGT lipid was deposited on the walls of a glass vial. The film was hydrated with an aqueous buffer (typically 50 mM tris, pH 7.5) by a combination of vortexing and bath sonication. Additional components such as salt (NaCl), or $MgCl_2$ were included in the hydration buffer. The resulting lipid dispersion was loaded into capillaries (Quartz capillaries from Hampton Research having the following specifications: length – 80 mm, outer diameter – 1.5 mm, wall thickness – 0.01 mm) and placed in a custom designed temperature-controlled capillary holder. Temperature was raised typically in steps of 10 °C over the range 10–90 °C. About 20 min was allowed at each temperature before collection of data. Typically, 20 consecutive 1 s scans were taken and averaged. Lipid phases were identified from the ratios of q-values of the Bragg peaks.

Cryogenic transmission electron microscopy (cryo-TEM)

Unilamellar vesicles were prepared in a manner identical to that for SAXS experiments. Cryo-TEM was carried out at the Stanford Cryo-Electron Microscopy Center (cEMc). 3–5 μL of an SUV dispersion was applied to a Quantifoil holey carbon grid (Quantifoil Micro Tools GmbH) that was previously glow discharged, blotted for 1–2 seconds, and plunge-frozen in liquid ethane using a Vitrobot Mark IV System (Thermo Scientific). The frozen grids were imaged with an FEI Tecnai F20 electron microscope (FEI Company) equipped with a Gatan K2 Summit direct detection device (Gatan Inc.) with a dose rate of 6–10 e^- per px per s. A low pass filter of 0.1 and mean shrink of 4 were applied to the raw images for visualization only. The raw images were processed with RELION 3.0. Overlapping regions of the bilayers (particles) were picked with the manual picking tool, extracted, CTF-corrected, and 2D averaged. The 2D classes with good alignment were reclassified into a single 2D class. These particles were randomly divided into 2 subsets and each subset was aligned and averaged independently. The electron scattering profiles of the bilayers

were calculated by taking a line profile of the 2D classes through the centre in FIJI. The peak-to-peak distances were calculated by fitting each profile to 2 Gaussian functions and computing the difference between each peak (https://terpconnect.umd.edu/%7Etoh/spectrum/CurveFittingC.html). The uncertainty was calculated as the standard deviation between the peak-to-peak distances of each independent half of each dataset.

Fusion of GDGT vesicles with influenza virus

Previously described experimental design and methodology of data analysis for viral membrane fusion was employed here.[36,37]

Influenza virus preparation. IAV (strain X-31, A/Aichi/68, H3N2) grown in the allantoic cavity of SPF eggs was purchased from Charles River Laboratories (Wilmington, MA). The main stock (HA titre: 32768/0.05 mL, EID_{50}: $10^{9.5}$ per mL, protein content: 2 mg mL^{-1}) was stored as 20 μL aliquots at −80 °C till use. IAV is a Biosafety Level 2 agent and was handled following an approved biosafety protocol at Stanford University. Texas Red-DHPE was incorporated into the IAV envelope by incubating virus sample with 10 μM of Texas Red-DHPE in HB buffer at 4 °C on ice overnight such that the total EtOH (necessary for dissolving Texas Red-DHPE) concentration in the labelling mixture did not exceed 2% v/v. The labelled virus suspension was directly diluted in vesicle buffer for use in lipid mixing experiments. For content mixing experiments, the commercially available virus suspension was directly diluted in vesicle buffer.

Vesicle preparation and fusion chamber. Large unilamellar vesicles (compositions summarized in Fig. 7A) were prepared by extrusion of a multilamellar dispersion through 100 nm polycarbonate filters. For content mixing experiments, self-quenching concentration (30 mM) of sulforhodamine B was included in the hydration buffer and the vesicles were separated from the free dye by size exclusion chromatography. All viral experiments were carried out using a simple microfluidic flow cell prepared from glass and polydimethylsiloxane (PDMS) by plasma-bonding. The glass surfaces of the flow cell's channels were passivated with co-polymers PLL-PEG/PLL-biotin-PEG. The vesicles were tethered to the passivated surface *via* NeutrAvidin, and excess vesicles were removed by flowing vesicle buffer through the channel.

Viral fusion experiments. Virus particles (labelled or unlabelled) were added to the flow cell and allowed to bind to the tethered vesicles for 15 min. Unbound virus particles were removed by flowing in vesicle buffer. pH was dropped by adding fusion buffer (pH 5.1) and a continuous video stream was acquired over 1200 frames at 3.47 fps. In the event of a lipid mixing or content mixing, signal from self-quenched Texas Red-DHPE or sulforhodamine B respectively turned brighter. The wait times between lowering of pH and appearance of a bright spot were calculated and compiled into cumulative distribution functions.

Results and discussion

Synthesis of GDGT lipids

In earlier work led by the Burns group, an efficient synthetic route to the core structure of parallel GDGT-0 (iso-caldarchaeol) was described.[34] In the same work, the synthesis of **P2** and **P1Glc** were reported. In this work, along with **P2** and **P1Glc**, the synthesis of two additional GDGT lipids – **PG2** and **PG1Glc** was achieved (Fig. 2, ESI Schemes S1–S7†). It should be noted that the glucosyl groups in **P1Glc** and **PG1Glc** are present as a mixture of anomers. **PG1Glc** is closest in structure to the naturally occurring archaeal lipid β-L-gulose-GDGT-PG.[38]

Self-assembly of GDGTs in aqueous media

We found that the GDGTs spontaneously self-assembled into giant vesicles (~1–20 μm diameter) in aqueous media upon hydration of a thin lipid film (typically after incubating at 65 °C) and the membranes were visualized by staining with the lipophilic dye-labelled Texas Red-DHPE (Fig. 3A and S1†). If a water-soluble fluorescent dye such as pyranine (HPTS) was added to the hydration solution, the vesicles encapsulated the dye in the inner aqueous volume (Fig. 3A and S1†). The GDGT vesicle membranes were observed under the microscope to display fluid-like behaviour such as shape fluctuations (Fig. 3B). However, it is noteworthy that unlike typical fluid phase phospholipids (*e.g.* POPC), the GDGT lipid films required increased mechanical forces (*i.e.*, scratching, vortexing, sonication) to disperse into vesicles, suggesting that the lipids are tightly packed in the thin films. Thin films of the glucose-containing lipids (**P1Glc** and **PG1Glc**) were harder to hydrate likely because of extensive intermolecular hydrogen-bonding among the sugar headgroups.[10] We empirically observed that the efficiency of hydration of the lipid films depended on the nature and ionic strengths of the buffers. Tris buffer (50 mM, pH 7.5) was found to be the most suitable for hydration of all the lipids studied. Only **PG2** films could readily hydrate in several other buffers like HEPES, PBS, and even in pure water to form vesicles. Also, only **PG2** could hydrate to form giant vesicles in the presence of proteins such as superfolder green fluorescent protein (sfGFP) and encapsulate the protein (Fig. 3C) while other GDGTs lipids formed aggregates. Next, we tested whether the multilamellar lipid dispersions can be extruded into smaller vesicles *via* extrusion through membrane filters. Using negative-staining TEM we confirmed the presence of vesicles having diameters less than 200 nm (Fig. S2†).

Given the large difference in intermolecular packing as compared to typical phospholipids, it is not obvious whether integral membrane proteins of non-archaeal origin can be reconstituted into GDGT vesicles. There are only a few examples of reconstitution of non-archaeal integral membrane proteins into crude archaeal GDGT lipid membranes. Elferink *et al.* reconstituted bovine cytochrome c-oxidase in lipid extracts from *Sulfolobus acidocaldarius* primarily composed of bipolar lipids.[11,39] Curiously, archaea are not known to be involved in photosynthesis, which is a heavily membrane-dependent process.[5] Therefore, we chose to reconstitute a bacterial photosynthetic reaction centre (RC) protein into GDGT membranes. First, we reconstituted RC in **PG2** membranes using detergent removal method. We then performed negative-staining TEM on the protein-lipid dispersion and detected spherical or nearly spherical structures of diameters 40–370 nm

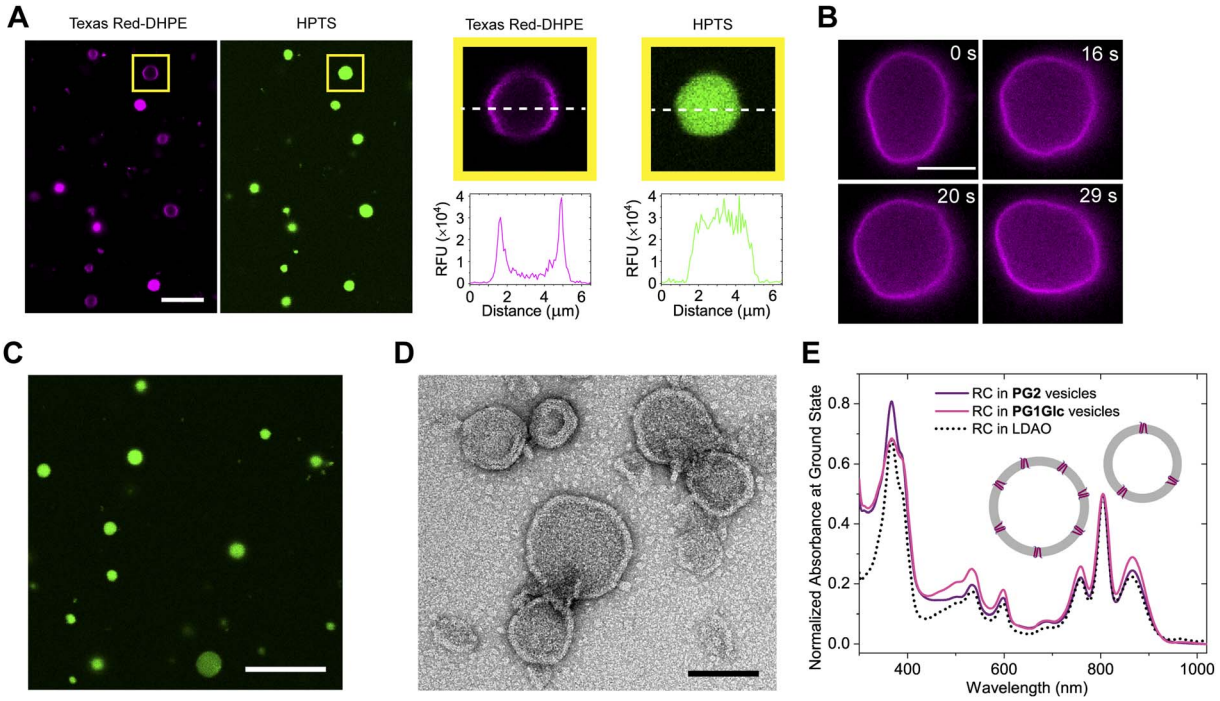

Fig. 3 Self-assembly of GDGTs in aqueous media. (A) Giant vesicles of **PG1Glc** consisting of unilamellar and multilamellar architectures formed by hydration of a thin film in tris buffer (50 mM, pH 7.5) imaged by laser-scanning confocal microscopy. Membranes were stained with 0.1 mol% Texas Red-DHPE (left) or the water-soluble dye pyranine (HPTS) was encapsulated inside (right). Scale bar: 10 μm. A single giant unilamellar vesicle (GUV) indicated in a box is enlarged and the corresponding fluorescence intensity profiles along a line across the centre in two channels are shown. (B) GDGT vesicles undergo shape fluctuations as observed with a **PG1Glc** GUV. Membranes were visualized with 0.1 mol% Texas Red-DHPE. Scale bar: 10 μm. (C) Encapsulation of sfGFP in giant vesicles of **PG2** imaged by laser scanning confocal microscopy. Scale bar: 15 μm. (D) Negative-staining TEM images of **PG2** vesicles reconstituting photosynthetic RC prepared by detergent removal method. Scale bar: 100 nm. (E) Ground state absorption spectrum of photosynthetic reaction centre (from *Rhodobacter spheroides*) reconstituted in **PG2** and **PG1Glc** vesicles (solid lines). For comparison, the spectrum of the same protein in detergent (LDAO) micelles is overlaid (dotted line).

(mean: 119 ± 63 nm, $n = 108$) corresponding to the proteoliposomes (Fig. 3D). To ascertain that the RC is still intact and functional after reconstitution into archaeal lipid, we first recorded the UV-Vis spectra, which confirmed that the protein is still properly assembled, and that the chromophores are still in place (Fig. 3E). We obtained a spectrum with similar features when the RCs were reconstituted into **PG1Glc** vesicles using similar methodology (Fig. 3E) suggesting that the protein is properly folded in these membranes too. Finally, we performed ultrafast transient absorption spectroscopy to see whether the RC is still able to perform primary electron transfer in this new environment. The results showed that RC can still undergo charge transfer, and the kinetics and mechanism are largely unchanged (Fig. S3A and B†).

Self-assembly of GDGTs at the air–water interface

Amphiphilic molecules self-assemble at the air–water interface to form insoluble monomolecular layers with the polar headgroup facing water and the hydrophobic region positioned in air. Since GDGTs have two polar head groups we were curious to test how they self-assemble at the air–water interface and therefore understand how flexible these molecules are conformationally. Using a Langmuir–Blodgett trough, we found that GDGT lipids form stable monomolecular layers at the air–water interface as evident from measurements of surface pressure–area (π–A) isotherms obtained by the Wilhelmy plate method (Fig. 4A and S4†). The isotherms exhibited stable liquid expanded behaviour lacking any first order transitions. In the case of **P2**, **P1Glc**, **PG2**, and **PG1Glc**, the surface pressure reached a plateau at significantly high values of 36 mN m^{-1}, 30 mN m^{-1}, 42 mN m^{-1}, and 41 mN m^{-1} respectively, which is indicative of monolayer stability.

The results were compared with those obtained with monopolar phospholipids having straight chains (POPC, DPPC) and archaeal-inspired branched-chain phospholipids (DPhPA, DPhPC, DoPhPC, DPhPG) (Fig. 4A and S4†). We found that the GDGTs display significantly higher mean molecular areas (MMA) as compared to monopolar lipids (Fig. 4B). At the lift-off point, the GDGTs display MMA considerably higher than 300 Å^2 while at a surface pressure of 25 mN m^{-1}, all GDGTs display MMA of approximately 250 Å^2. The corresponding values for monopolar lipids are at least 3–4 times smaller. The high MMA values of the GDGTs can be explained by suggesting that these lipids have the conformational flexibility to loop into a U-shaped conformation at the air–water interface – *i.e.*, with both headgroups facing water and the hydrocarbon chains forming an arch (Fig. 4C).

A

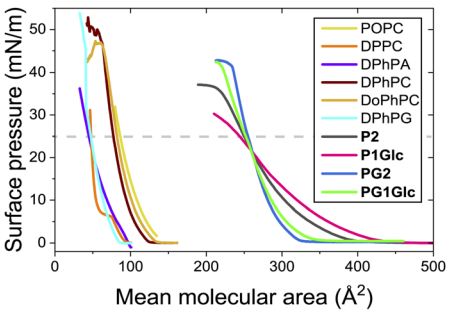

B

Lipid	Lift-off area (Å²)	MMA at 25 mN/m (Å²)
POPC	142	86
DPPC	94	48
DPhPA	97	45
DPhPC	88	77
DoPhPC	133	82
DPhPG	85	47
P2	385	251
P1Glc	425	243
PG2	326	252
PG1Glc	348	255

C

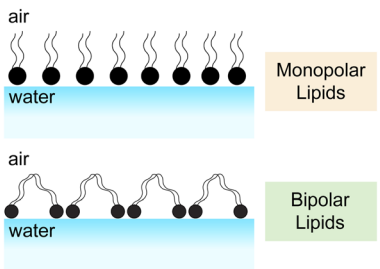

Fig. 4 Self-assembly at air–water interface. (A) Surface pressure–area (π–A) isotherms of various monopolar and bipolar (GDGT) lipids measured using a Langmuir–Blodgett trough and Milli-Q water as subphase. (B) Table showing lift-off areas (A_0) and mean molecular areas (MMA) measured at 25 mN m^{-1} from a single measurement. (C) Schematic diagram showing the likely arrangements of monopolar and bipolar lipids at the air–water interface.

Measurement of structural properties of GDGT membranes

There are well-established X-ray based methods for elucidating the structure of lipid bilayers.[40,41] Here we measured the thicknesses of the GDGT membranes from small-angle X-ray scattering (SAXS) on unilamellar vesicles in solution. In this method, only diffuse scattering is obtained from uncorrelated membranes and therefore no Bragg peaks are observed.[42] The observed scattering intensity profiles result from the difference in scattering length densities between the lipids and the buffer.[42] In a typical experiment, we obtained scattering intensity profiles from GDGT unilamellar vesicles characterized by three broad lobes (Fig. 5A). The profiles were fitted to a well-established model based on a simulated annealing algorithm that has been previously used to compute asymmetric bilayer electron density profiles (EDP);[42–44] all fitting parameters are provided in Table S1.† A typical EDP is characterized by two peaks corresponding to the electron-rich lipid headgroup regions separated by a trough corresponding to the electron-deficient hydrocarbon region (Fig. 5B). Therefore, the head-to-head distances in a lipid membrane can be readily measured from the peak-to-peak distances of the EDPs which ranged between 38–40 Å for the GDGT lipids (Fig. 5B). The measurements are in good agreement with a previous study where lamellar repeat distances (which includes thickness of water layer too) of ~49–50 Å were measured in crude tetraether lipid dispersions[7] or multilamellar vesicles.[45] Cryogenic transmission electron microscopy was used to confirm the unilamellar nature of the vesicles and measure the thicknesses of the membranes. Small unilamellar vesicles of GDGTs were vitrified on holey carbon grids using standard techniques and imaged by cryo-EM. The overwhelming majority of the vesicles were unilamellar displaying uni-vesicular or multi-vesicular (or "vesicle-in-vesicle") architectures (Fig. 5C, S5A and B†). In addition, some sponge-like morphologies comprising of an interconnected network of membranes[46] were observed in case of **P2** and **PG1Glc** which were excluded from bilayer profile analysis (Fig. S5C†). We measured the thickness of each membrane by segmenting vesicles into small regions and aligning and averaging the segments to derive 2D class averages (Fig. 5C). The linear profile of each membrane was measured across the centre of the aligned and averaged images to obtain corresponding electron scattering profiles (ESPs) (Fig. 5D). In agreement with the SAXS results, we found that the membrane thicknesses for all GDGT lipids were similar. Congruent with previous work, measured membrane thicknesses were approximately 8 Å thinner than those measured by SAXS (Fig. 5D), likely due to the different physics of X-ray and electron scattering, the different resolutions of the two methods, and the influence of the contrast transfer function (CTF) of the electron microscope on the process of image formation.[47] Regarding the latter, the strong Fresnel fringe adjacent to the outer leaflet indicates that the CTF is incompletely corrected, and this trough of negative intensity likely affects the measured peak-to-peak distance.[47] We also note that the membrane profiles obtained from cryo-EM have a different shape than those obtained from SAXS because they represent the projection of the spherical density rather than the EDP normal to the plane of the bilayer. Regardless of the absolute membrane thickness, cryo-EM can measure the relative thicknesses of membranes composed of GDGT analogues with sub-Ångström precision. Together, the SAXS and cryo-EM data demonstrate that the thicknesses of GDGT membranes is primarily determined by their hydrocarbon chains rather than their headgroups.

Characterization of mesophases formed by GDGTs

Lipid molecules self-assemble into supramolecular structures called mesophases (*e.g.* lamellar, hexagonal, cubic) depending on their molecular geometry and external factors. Functional roles of lipids are dictated by their propensity to form specific mesophases. For example, the tendency of phosphoethanolamine lipids to form inverted non-lamellar phases has been associated with their role in facilitating fusion of biological membranes *via* induction of negative curvature.[48] SAXS on bulk lipid dispersions produces characteristic diffraction patterns from which specific mesophases can be ascertained (Fig. 6A).[49]

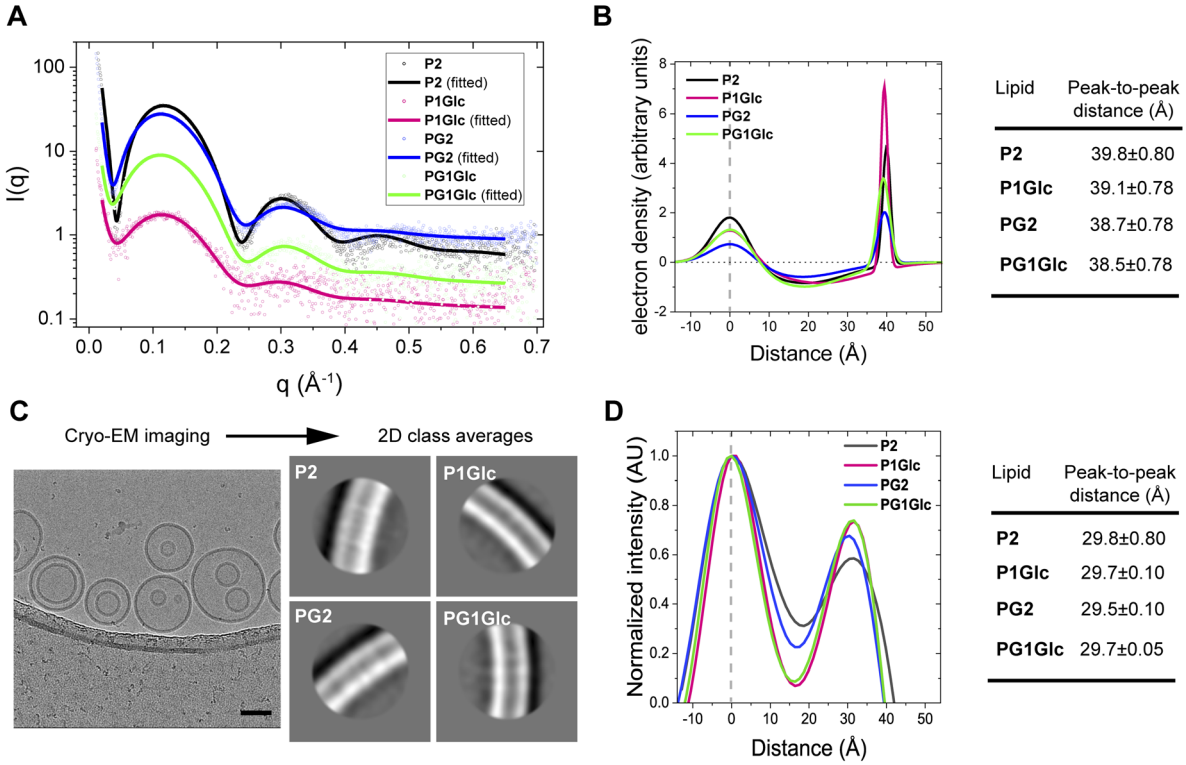

Lipid	Peak-to-peak distance (Å)
P2	39.8±0.80
P1Glc	39.1±0.78
PG2	38.7±0.78
PG1Glc	38.5±0.78

Lipid	Peak-to-peak distance (Å)
P2	29.8±0.80
P1Glc	29.7±0.10
PG2	29.5±0.10
PG1Glc	29.7±0.05

Fig. 5 Structural characterization of GDGT membranes. (A) Small-angle X-ray scattering (SAXS) intensity profiles from unilamellar vesicles of GDGTs in tris buffer (50 mM, pH 7.5) at room temperature. The solid lines correspond to the data fitted to the raw data points (open circles). (B) Electron density profiles (EDP) of GDGT membranes calculated from the SAXS intensity profiles. The peak-to-peak distance corresponds to the head-to-head distances of lipids in a membrane. The centres of the 1st peaks of all EDPs were arbitrarily set to '0'. All fit parameters are summarized in Table S1.† (C) Representative cryogenic electron microscopy images of unilamellar (and multi-compartment) vesicles of **P2** prepared in tris buffer (50 mM, pH 7.5). Scale bar represents 50 nm. The adjoining images show the 2D class averages for each lipid. (D) Electron scattering profiles (ESPs) of GDGT membranes calculated from cryo-EM images. The peak-to-peak distances correspond to the thicknesses of the membranes. The centres of the 1st peaks of all ESPs were arbitrarily set to '0'. All error values correspond to fitting error.

We sought to establish a link between the mesophase behaviour of the lipids across a wide temperature range and their probable functional roles in archaeal cell membranes. Differential scanning calorimetry (DSC) studies on bulk GDGT lipid mixtures from extracts typically revealed that the lipids exist in fluid phases at all temperatures and do not exhibit any endothermic lamellar phase transitions (*i.e.* gel-to-fluid).[34] However, it may be challenging to detect transitions between lamellar and non-

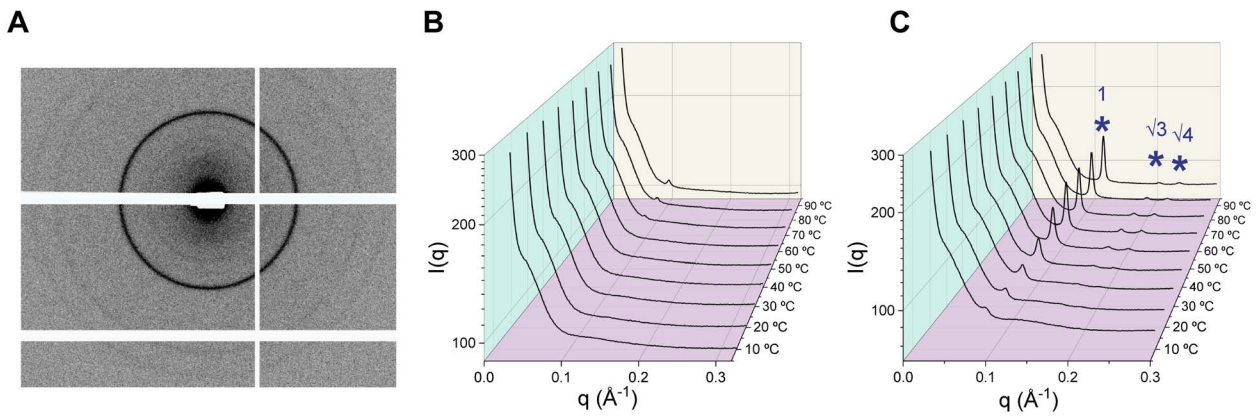

Fig. 6 Characterization of lipidic mesophases using SAXS. (A) Concentric diffraction rings (2D detector image) from a lipid dispersion are characteristic of underlying mesophases. (B) Dispersions of the lipid **PG1Glc** in 50 mM tris, pH 7.5 mostly do not exhibit any characteristic features over 10–90 °C. (C) SAXS intensity profile from **PG1Glc** dispersion in 50 mM tris, pH 7.5 containing 10 mM $MgCl_2$ over 10–90 °C. Hexagonal phase peaks (at ratios 1 : √3 : √4) are marked by blue asterisks (*).

Table 1 Summary of lipidic mesophases formed by the GDGT lipids under various buffer conditions over 10–90 °C. "buffer" refers to 50 mM tris

	Conditions	P2	P1Glc	PG2	PG1Glc
Variable salt concentration	Buffer only (pH 7.5)	Disordered lamellar (10–90 °C)	Disordered lamellar (10–30 °C), hexagonal (40–90 °C)	Disordered lamellar (10–90 °C)	Disordered lamellar (10–90 °C)
	Buffer + 0.1 M NaCl (pH 7.5)	Disordered hexagonal (10–20 °C) Hexagonal (30–70 °C) Hexagonal + cubic *Pn3m* (80–90 °C)	Disordered lamellar (10–40 °C) Hexagonal (50–90 °C)	Disordered lamellar (10–90 °C)	Disordered lamellar (10–90 °C)
	Buffer + 0.5 M NaCl (pH 7.5)	Lamellar (10–40 °C) Cubic *Ia3d* (50 °C) Hexagonal (60–90 °C)	(Not dispersible)	Disordered lamellar (10–90 °C)	Disordered lamellar (10–20 °C) Hexagonal (30–90 °C)
	Buffer + 1.0 M NaCl (pH 7.5)	Lamellar (10–30 °C) Lamellar + hexagonal (40–60 °C) Hexagonal (70–90 °C)	(Not dispersible)	Lamellar (10–20 °C) Disordered lamellar (30–90 °C)	Hexagonal (10–90 °C)
Mg^{2+}	Buffer + 10 mM Mg^{2+} (pH 7.5)	Lamellar (10–90 °C)	Lamellar phase 1 (10–90 °C) Lamellar phase 2 (10–90 °C)	Disordered lamellar (10–40 °C) Hexagonal (50–90 °C)	Hexagonal (10–90 °C)
Acidic pH	Buffer (pH 5.1)	Disordered lamellar (10–90 °C)	Disordered lamellar (10–90 °C)	Disordered lamellar (10–90 °C)	Disordered lamellar (10–90 °C)
	Buffer (pH 2.8)	(Not dispersible)	(Not dispersible)	Hexagonal (30–50 °C)	Hexagonal (10–90 °C)

lamellar phases which are typically characterized by low enthalpy changes.[50] Moreover, each DSC measurement requires a significant amount of material that is not always practical to recover. Therefore, we characterized the mesophases formed by aqueous GDGT dispersions using synchrotron SAXS over 10–90 °C under the influence of (i) varying salt concentration; (ii) presence of Mg^{2+}; and (iii) acidic pH. The results are summarized in Table 1.

In a low ionic strength buffer such as 50 mM tris (pH 7.5), the SAXS intensity profiles of **P2**, **PG2**, and **PG1Glc** were mostly featureless (Fig. 6B, S6, S8 and S9†) over the entire temperature range. Lack of features suggest that the lipids mostly formed uncorrelated bilayers in tris buffer due to repulsive forces between the charged headgroups. Repulsive forces may also arise from mutual steric hindrance between undulating membranes stacked in a liquid crystalline multilayer.[51] **P1Glc** exhibited a weak hexagonal phase at 30 °C which gradually increased in intensity with temperature (Fig. S7†). Addition of salts is expected to screen the electrostatic repulsion and generate more ordered structures. Therefore, we investigated the effect of 0.1 M, 0.5 M, and 1 M NaCl added to 50 mM tris buffer (pH 7.5). Among all lipids, **P2** exhibited the most complex behaviour at varying salt concentrations (Fig. S6†). In the presence of 0.1 M NaCl, somewhat broad and low intensity H_{II} peaks were observed at 10–20 °C which became sharper and more intense over 30–70 °C. Over 80–90 °C, a *Pn3m* cubic phase coexisted with the H_{II} phase. In 0.5 M NaCl, strong lamellar peaks were seen at 10 °C which fully transitioned to H_{II} peaks at 60 °C and above *via* an *Ia3d* cubic phase at 50 °C. In 1.0 M NaCl, strong lamellar peaks existed over 10–30 °C which coexisted with an H_{II} phase at 40–60 °C and an H_{II} phase only was observed at higher temperatures. **P1Glc** was difficult to disperse even in the presence of 0.1 M NaCl and a hexagonal phase was detectable at 50 °C and above (Fig. S7†). **P1Glc** film could not be hydrated at higher salt concentrations. **PG2** exhibited disordered phases at all salt concentrations except a small degree of lamellar ordering over 10–30 °C in the presence of 1 M NaCl (Fig. S8†). These observations are in good agreement with microscopy studies where we see facile formation of **PG2** vesicles in buffers having a similar range of ionic strengths. **PG1Glc** displayed disordered phases in 0.1 M NaCl, but a hexagonal phase started to appear above 30 °C in the presence of 0.5 M NaCl (Fig. S9†). In the presence of 1 M NaCl, a small hexagonal phase peak was detectable even at 10 °C which increased in intensity with temperature (Fig. S9†). It is noteworthy that formation of non-lamellar phases (hexagonal and/or cubic) at high temperatures have been observed in crude archaeal bipolar lipid mixtures[52] or archaeal-inspired model bipolar lipids[27] as well. Our results suggest that such behaviour can be retained in pure individual GDGT species too.

Next, we studied the effect of Mg^{2+} ions on the phase behaviour of GDGTs (Fig. S10A–D†). Both phosphate-containing lipids **P2** and **P1Glc** exhibited strong lamellar ordering at all temperatures in the presence of $MgCl_2$. **P2** exhibited sharp Bragg peaks at all temperatures with lamellar *d*-spacing of 4.95 nm at 10 °C which monotonically decreased to 3.93 nm at 90 °C. **P1Glc** exhibited Bragg peaks corresponding to a mixture of two lamellar phases having lamellar *d*-spacing of 4.67 nm and 4.49 nm at 10 °C likely arising from a mixture of stiff and disordered hydrocarbon chains as previously observed with crude archaeal BTL extracts.[52] The spacings monotonically decreased to 3.99 nm and 3.95 nm respectively at 90 °C. On the

other hand, the phosphoglycerol-containing lipids **PG2** and **PG1Glc** exhibited hexagonal phases in the presence of $MgCl_2$. In the case of **PG2**, a weak and broad hexagonal phase peak appeared at 50 °C and it became more prominent at higher temperatures. For **PG1Glc**, a poorly resolved broad 1st H_{II} peak appeared at 10 °C which increased in prominence with temperature, and the 2nd and 3rd H_{II} peaks could be unambiguously assigned only above 50 °C. We reason that upon binding of Mg^{2+} to the PG headgroup phosphates, they bridge together. Consequently, the volume of the headgroup region becomes smaller in comparison to the hydrocarbon region and the molecules organize into a hexagonal phase. Interestingly, we also observed Mg^{2+}-induced H_{II} phase formation in the monopolar diphytanoyl archaeal lipid DPhPG (which has a negative spontaneous curvature) at all temperatures (Fig. S11†), which supports the idea that bridging of PG-headgroups by Mg^{2+} ions is the primary driver of H_{II} phase formation.

Since GDGT lipids occur in thermoacidophilic archaea, we investigated the effect of acidic pH on their mesophase behaviour. The phosphate containing lipids **P2** and **P1Glc** could not be dispersed in 50 mM tris (pH 2.8) likely because of partial protonation of the phosphate groups. Interestingly, both the phosphoglycerol containing lipids **PG2** and **PG1Glc** were found to form hexagonal phases at pH 2.8 over the temperature range (30–90 °C) surveyed (Fig. S10E and F†). For **PG1Glc**, the H_{II} peaks were sharp and three H_{II} peaks (ratios of $1:\sqrt{3}:\sqrt{4}$) were detected at all temperatures. We reason that due to protonation of the PG groups ($pK_a \sim 3$)[53] they become less hydrated and therefore decrease in volume. Notably, we did not observe hexagonal phase in **PG2** and **PG1Glc** at pH 5.1, where the PG headgroups are expected to be fully deprotonated.

Fusion behaviour of membranes composed of GDGTs

Like any organism, archaea must perform dynamical membrane processes such as fission and fusion during cell division, membrane vesicle budding, or viral entry/egress. However, there is a lack of clarity regarding how archaeal membranes primarily composed of bipolar lipids can undergo fusion (or fission). In a canonical model of bilayer membrane fusion, the outer leaflets of apposing membranes first merge to form a stalk-like hemifusion intermediate.[48] This step is triggered by fusogenic agents like divalent cations, acidic pH, polyethylene glycol, or fusion peptides which help overcome the energetic barriers associated with various intermediate steps along the fusion pathway. In the next step, the inner leaflets merge *via* transient non-lamellar intermediates to open a fusion pore and the two membranes completely fuse along with mixing of inner aqueous contents. In the case where GDGT lipids form a monolayer membrane with all lipids in membrane-spanning conformation, there would likely be high energy barriers and geometrical constraints to forming various fusion intermediates as compared to bilayer membranes. Therefore, we hypothesize that at least some regions of the GDGT membrane should have a bilayer structure which is only possible if some lipids adopt a looping or U-shaped conformation (Fig. 1B). Whether the bipolar lipid membranes can undergo fusion or not and how such behaviour is related to the conformations of lipids (O *vs.* U) has been a subject of intense investigation. A theoretical study predicted that membrane fusion of bipolar lipid membranes take place through regions consisting of U-shaped lipids.[54] Leriche and coworkers demonstrated that vesicles composed purely of an acyclic bipolar lipid can undergo Ca^{2+}-induced fusion without loss of contents.[55] They further probed lipid ordering using ^{2}H-NMR and concluded that the bipolar lipids adopt both O- and U-shapes in membranes although precise percentages were not determined. ^{2}H-NMR experiments on model acyclic bipolar lipid membranes suggest that 90% of the lipids exist in O-shape and 10% in U-shape.[29] In principle, atomic force microscopy (AFM) may be used to visualize O- and U- shaped regions since they will be expected to have different thicknesses;[56] however, such studies will ideally need to be performed on planar supported membranes or GUV patches. Given that the GDGTs in our study are anionic, planar supported membranes or membrane patches could not be generated on clean glass surface (which is negatively charged) *via* vesicle fusion or rupture of GUVs. Many studies on archaeal lipid mixtures attempted to establish a rational link between the lipid structures and membrane fusion (or the lack thereof) induced by Ca^{2+} or PEG.[13,57–59] For example, Relini *et al.* noted that vesicles formed from archaeal lipid extracts which displayed transformations between lamellar and non-lamellar phases underwent fusion implying that lipids that can form non-lamellar phases are necessary to induce membrane curvature during fusion.[13]

In previous sections, we showed that under the influence of temperature, salt concentration, pH, or divalent cations, GDGTs show diverse mesophases, especially the formation of inverted non-lamellar phases. Although those lamellar to non-lamellar phase transitions were observed in bulk lipid dispersions, the presence of non-lamellar phase lipids in membranes likely increase the propensity to form local transient non-lamellar structures essential for fusion to take place. Therefore, we asked whether the tendency of GDGT lipids to form non-lamellar phases is related to membrane fusion. To test the fusion behaviour of GDGT vesicles, we devised a novel assay where we chose influenza virus as a fusogenic agent as the latter possesses an efficient fusion machinery embedded in a bilayer lipid membrane that triggers a fusion pathway representative of many biological fusion processes.[60]

We followed a widely utilized fluorescence microscopy assay to observe fusion of viruses with lipid vesicles on a single particle level.[36,37] In this method, the vesicles are allowed to undergo pH-induced fusion with bound influenza virus labelled with self-quenching concentrations of Texas Red-DHPE (Fig. 7A). 100 nm vesicles composed overwhelmingly of GDGT lipids (PG2 mix – **PG2** : GD1a : Biotin-DPPE : Atto 647N-DMPE 98.45 : 1 : 0.5 : 0.05; PG1Glc mix – **PG1Glc** : GD1a : Biotin-DPPE : Atto 647N-DMPE 98.45 : 1 : 0.5 : 0.05 by molar ratio) were prepared in a pH 7.4 buffer. The vesicles were tethered to a functionalized glass slide through interaction of neutravidin with Biotin-DPPE (Fig. 7A). Next, influenza virus particles labelled with a self-quenching concentration of Texas Red-

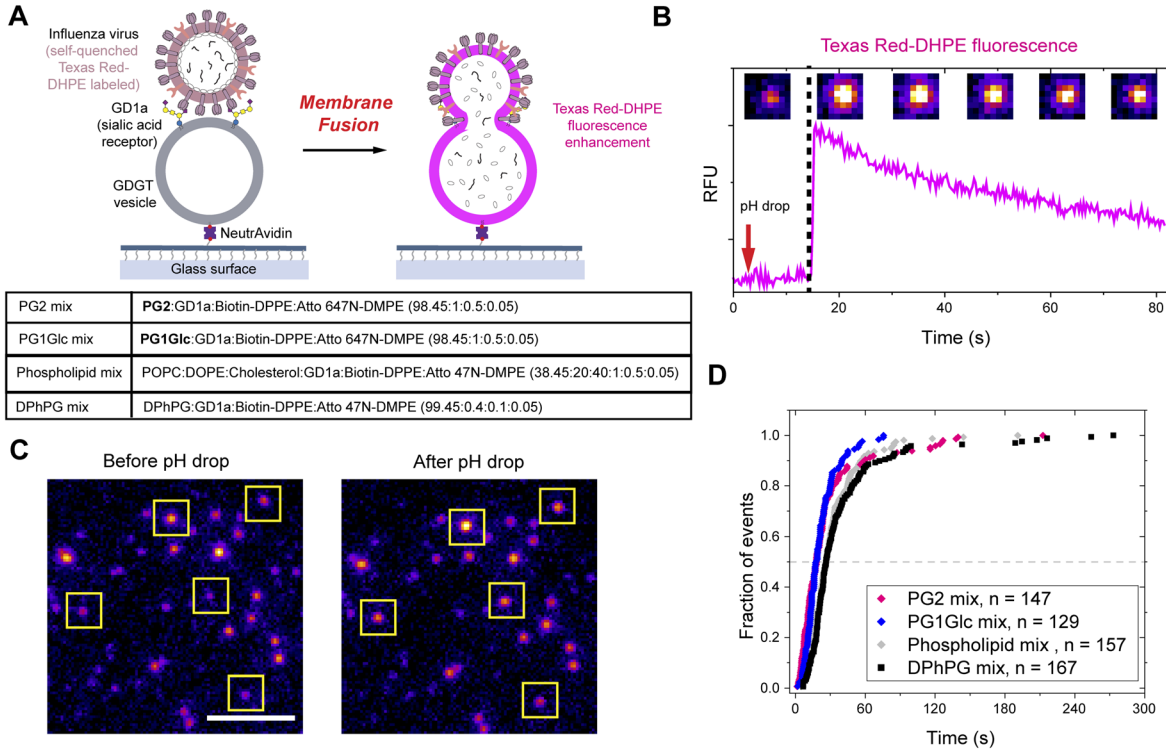

PG2 mix	**PG2**:GD1a:Biotin-DPPE:Atto 647N-DMPE (98.45:1:0.5:0.05)
PG1Glc mix	**PG1Glc**:GD1a:Biotin-DPPE:Atto 647N-DMPE (98.45:1:0.5:0.05)
Phospholipid mix	POPC:DOPE:Cholesterol:GD1a:Biotin-DPPE:Atto 47N-DMPE (38.45:20:40:1:0.5:0.05)
DPhPG mix	DPhPG:GD1a:Biotin-DPPE:Atto 47N-DMPE (99.45:0.4:0.1:0.05)

Fig. 7 Acidic pH-induced fusion of GDGT vesicles with influenza virus. (A) Schematic diagram showing vesicles tethered to glass surface *via* Biotin-DPPE binding to influenza virus particles (labelled with a self-quenching concentration of Texas Red-DHPE) *via* a sialoglycolipid receptor GD1a. Upon lowering of pH, the self-quenched Texas Red-DHPE undergoes dilution, and its fluorescence is enhanced. (B) Fluorescence intensity trace (Texas Red channel, 561 nm emission) of a single fusion event between influenza virus and "PG2 mix" vesicles are shown along with corresponding microscopy images at various time points. (C) Microscopy images showing many fusion events (indicated in yellow boxes) between influenza virus particles and "PG2 mix" vesicles are observed. Scale bar: 5 μm. (D) Cumulative distribution functions corresponding to wait times to individual lipid mixing events for viral fusion with 100 nm vesicles composed of monopolar lipids ("phospholipid mix" and "DPhPG mix") and bipolar lipids ("PG2 mix" and "PG1Glc mix").

DHPE were added. The α2,3-silaic acid containing sialoglycolipid GD1a served as the receptor for influenza hemagglutinin binding. The pH was lowered by flowing in an acidic buffer (pH 5.1). Upon hemifusion, the outer leaflets of viral and vesicle membranes merge and the Texas Red-DHPE gets diluted. Consequently, its fluorescence quenching is relieved as evident from a sudden spike in fluorescence intensity (Fig. 7B).

Interestingly, we observed on a single particle level that many dim fluorescent spots (corresponding to a virus particle labelled with self-quenched TR-DHPE) turned brighter (Fig. 7C). We plotted the time to the onset of lipid mixing into cumulative distribution function for many vesicle populations and found that the fusion of GDGT vesicles follow a kinetics comparable to that with vesicles composed of monopolar phospholipids and cholesterol ("phospholipid mix")[33] or vesicles composed primarily of monopolar archaeal-type lipids ("DPhPG mix") (Fig. 7D). Next, we tested whether the small percentage (1.55 mol%) of monopolar lipids (*i.e.* bilayer forming) added to the GDGT vesicles in the previous experiments necessary for viral attachment and surface tethering have any significant influence over the outcome of membrane fusion. We prepared **PG2** vesicles containing even smaller percentages (1 mol% and 0.5 mol%) of monopolar lipids and still observed many lipid mixing events (Fig. S12†). The kinetics of those events were nearly identical to that observed with "DPhPG mix" (having 100 mol% of monopolar lipids) vesicles (Fig. S12†). Therefore, we reason that the tiny percentages of monopolar lipids necessary to functionalize the GDGT vesicles do not have any significant influence on the outcome of the membrane fusion process and the fusion of GDGT vesicles is likely mediated by bilayer regions formed from U-shaped lipids.

Next, we asked whether the fusion events led to full fusion or whether they were arrested at the hemifusion stage. To address this question, we prepared "PG2 mix" vesicles encapsulating self-quenching concentration of the water-soluble dye sulforhodamine B (SRB) (Fig. S13A†). In the event of a full fusion, the interiors of the virus and vesicle compartments become one and the fluorescence of SRB is enhanced upon dilution.[61] We allowed unlabelled influenza virus particles to bind to tethered GDGT vesicles and then lowered the pH to 5.1. We observed many events where a dim fluorescent spot turned brighter indicating transfer of SRB from vesicle to virus through the fusion pore with nearly identical kinetics as compared to vesicles composed of monopolar phospholipids ("phospholipid mix") (Fig. S13B and C†).

Conclusions

We have described the synthesis of a series of chemically pure GDGT-0 lipids which enabled in-depth biophysical investigations on those. Although symmetric combinations of headgroups (such as in **P2** and **PG2**) are not yet reported to occur naturally, overall, we found that their self-assembly and structural properties share many parallels with those of their unsymmetric counterparts (*i.e.* **P1Glc** and **PG1Glc** respectively). Therefore, for many bottom-up biophysical studies, symmetric GDGTs, which are easier to synthesize, should serve as reasonably good model lipids. Symmetric GDGT lipids are also of interest to computational researchers likely because of the ease of theoretical modelling.[62,63] Therefore, availability of experimental data on such lipids will be beneficial for future computational studies. Archaeal BTLs have long been considered as excellent building blocks of liposomal drug delivery systems, lipid nanoparticles for mRNA delivery, synthetic cell membranes, or as matrix for membrane protein reconstitution with exceptional long-term structural and thermal stabilities.[10,64–66] It is notable that the lipid **PG2** (followed by **PG1Glc**) offered the most optimal properties (such as ease of dispersion and tolerance to many buffers and macromolecules) for broad applicability akin to typical glycerophospholipids, and therefore may find many applications as a model GDGT such as mentioned above. Although **P2** and **P1Glc** are not ideal for forming vesicles on their own, they can nevertheless be used as minor components in lipid mixtures.

In this work, we also addressed the question of what conformations GDGT lipids adopt in a membrane and how those impact the functional behaviour of the membranes. While it is generally considered that archaeal BTLs adopt a membrane-spanning conformation (O-shape), we have provided structural and functional evidence that GDGT-0 lipids possess the conformational flexibility to fold into U-shapes in a membrane. First, we showed that the GDGT-0 lipids adopt U-shapes in monomolecular films at the air–water interface as evident from the significantly higher mean molecular area occupied by these lipids in comparison to monopolar lipids. Conformational flexibility is further evident from the rich mesophase behaviour for each GDGT lipid which were found to transform between lamellar and non-lamellar phases at various combinations of buffer and temperature conditions. Next, we developed a novel assay where we showed that vesicles primarily composed of a single GDGT lipid species can undergo pH-induced fusion with influenza virus particles at kinetic rates comparable to that measured with conventional monopolar lipid vesicles. Such behaviour can be explained by considering that the GDGT membranes at least partially consist of bilayer regions composed of U-shaped lipids that act as sites of fusion. Whether the influenza fusion protein (hemagglutinin) has any direct role in inducing local bilayer structures that allow membrane hemifusion will require further investigation. Previous reports suggest that viral fusion peptides can induce inverted non-lamellar phases in phosphoethanolamine lipids which have a tendency to form hexagonal phases at high temperatures.[67,68] Similarly, the tendency of GDGT-0 lipids to form inverted non-lamellar phases possibly allows stabilization of fusion intermediates upon interaction with influenza viral fusion peptide.

Examples from archaeal biology indeed support our idea that GDGT-0 lipids have a greater tendency to adopt U-shapes and play a pivotal role in membrane dynamics. For instance, it has been observed that enveloped archaeal viruses such as Sulfolobus Spindle-Shaped Virus 1 (SSV1) consist of a disproportionately larger fraction (68.1%) of GDGT-0 lipids in their envelope as compared to its host *Sulfolobus solfataricus* (0.8%).[69] The presence of high fraction of GDGT-0 lipids in the viral membranes potentially facilitates their fusion with the host membranes both during entry and budding. Another matter that will be interesting to investigate in the future is the impact of the cycloalkane rings in the hydrocarbon region of the higher order GDGT-n ($n \geq 1$) lipids. GDGTs containing n cyclopentane rings are expected to be conformationally rigid and less likely to loop into a U-shape. Future studies involving fusion of archaeal enveloped viruses with model membranes consisting of GDGTs with variable number of rings ($n \geq 0$) will indeed provide deeper insights into fusion mechanisms of such viruses.

Finally, the observation that GDGT vesicles can fuse with influenza virus also opens the possibility of their application as novel chemically stable components of optical sensing devices for cell-free detection of infectious virus particles, and such efforts are currently underway.

Data availability

Data presented in this article are available in the main manuscript and the ESI.† Additional data can be available upon reasonable request made to the corresponding authors.

Author contributions

AB performed the biophysical experiments under the guidance of SGB. IDF carried out the synthesis of GDGT lipids under the guidance of NZB. FRM and AB performed the cryo-EM experiments. TMW collaborated on the SAXS experimental setup and data analysis software. KNT purified photosynthetic reaction centre. AB, FRM, NZB and SGB wrote the paper with inputs from all authors.

Conflicts of interest

There are no conflicts to declare.

Acknowledgements

This work was carried out with support from the NSF (MCB-1915727) and NIH (R35GM118044) grants awarded to SGB and from the NSF (CAREER CHE-1846512) grant awarded to NZB. AB acknowledges an Education & Outreach Grant offered by nano@stanford (which is supported by the National Science Foundation as part of the National Nanotechnology Coordinated Infrastructure under award ECCS-2026822) for partial

financial support. Part of this work was performed at the Stanford Nano Shared Facilities (SNSF), supported by the National Science Foundation under award ECCS-2026822. Electron microscopy imaging carried out at the Cell Sciences Imaging Facility (CSIF) at Stanford University was supported, in part, by ARRA Award Number 1S10RR026780-01 from the National Center for Research Resources (NCRR). Use of the Stanford Synchrotron Radiation Lightsource (SSRL), SLAC National Accelerator Laboratory, is supported by the US Department of Energy (DOE), Office of Science, Office of Basic Energy Sciences under Contract DE-AC02-76SF00515. The SSRL Structural Molecular Biology Program is supported by the DOE Office of Biological and Environmental Research and by the National Institutes of Health, National Institute of General Medical Sciences (P30GM133894). The Pilatus detector at beamline 4-2 at SSRL was funded under National Institutes of Health Grant S10OD021512. We thank Profs. Dewey Holten and Christine Kirmaier, and Dr Kaitlin Faries of Washington University for providing the ultrafast spectroscopic measurements on photosynthetic reaction centre shown in Fig. S3.† We thank Sawan Kumar Jha (Red Horse Lab, Stanford) and Suraj Borkar (Gerald Fuller Lab, Stanford) for collaborating with for collaborating with confocal microscopy and Langmuir trough experiments respectively. We thank Srijit Mukherjee (Boxer Lab) for insightful suggestions regarding the manuscript.

Notes and references

1 N. O. Medina-Chávez and M. Travisano, *Front. Genet.*, 2022, **12**, 693193.
2 Y. M. Bar-On, R. Phillips and R. Milo, *Proc. Natl. Acad. Sci. U. S. A.*, 2018, **115**, 6506–6511.
3 A. Caforio and A. J. M. Driessen, *Biochim. Biophys. Acta, Mol. Cell Biol. Lipids*, 2017, **1862**, 1325–1339.
4 A. Bhattacharya, *Emerging Top. Life Sci.*, 2022, **6**, 571–582.
5 V. Sojo, *BioEssays*, 2019, **41**, 1800256.
6 S. Schouten, E. C. Hopmans and J. S. Sinninghe Damsté, *Org. Geochem.*, 2013, **54**, 19–61.
7 P. L. G. Chong, *Chem. Phys. Lipids*, 2010, **163**, 253–265.
8 A. Bonanno, R. C. Blake and P. L. G. Chong, *Int. J. Mol. Sci.*, 2019, **20**, 5308.
9 J. S. Sinninghe Damsté, W. I. C. Rijpstra, E. C. Hopmans, J. W. H. Weijers, B. U. Foesel, J. Overmann and S. N. Dedysh, *Appl. Environ. Microbiol.*, 2011, **77**, 4147–4154.
10 G. D. Sprott, Archaeal Membrane Lipids and Applications, *eLS*, 2011, DOI: **10.1002/9780470015902.a0000385.pub3**.
11 M. G. L. Elferink, J. G. De Wit, R. Demel, A. J. M. Driessen and W. N. Konings, *J. Biol. Chem.*, 1992, **267**, 1375–1381.
12 T. J. Beveridge, C. G. Choquet, G. B. Patel and G. D. Sprott, *J. Bacteriol.*, 1993, **175**, 1191–1197.
13 A. Relini, D. Cassinadri, Q. Fan, A. Gulik, Z. Mirghani, M. De Rosa and A. Gliozzi, *Biophys. J.*, 1996, **71**, 1789–1795.
14 S. Dante, M. De Rosa, *et al.*, *Thin Solid Films*, 1996, **285**, 459–463.
15 A. Gliozzi, R. Rolandi, M. De Rosa and A. Gambacorta, *J. Membr. Biol.*, 1983, **75**, 45–56.
16 M. De Rosa, A. Gambacorta and B. Nicolaus, *J. Memb. Sci.*, 1983, **16**, 287–294.
17 C. T. Lloyd, D. F. Iwig, B. Wang, M. Cossu, W. W. Metcalf, A. K. Boal and S. J. Booker, *Nature*, **609**, 197–203.
18 Z. Zeng, H. Chen, H. Yang, Y. Chen, W. Yang and P. V Welander, *Nat. Commun.*, 2022, **13**, 1545.
19 S. Dante, F. Rustichelli, B. Yang, M. De Rosa, A. Morana, E. Maccioni, C. Nicolini and V. I. Troitsky, *Mol. Cryst. Liq. Cryst. Sci. Technol., Sect. A*, 1995, **262**, 191–207.
20 C. Dietrich, L. A. Bagatolli, Z. N. Volovyk, N. L. Thompson, M. Levi, K. Jacobson and E. Gratton, *Biophys. J.*, 2001, **80**, 1417–1428.
21 P. L. G. Chong, M. Sulc and R. Winter, *Biophys. J.*, 2010, **99**, 3319–3326.
22 H. Shimada and A. Yamagishi, *Biochemistry*, 2011, **50**, 4114–4120.
23 M. L. Bode, S. R. Buddoo, S. H. Minnaar and C. A. du Plessis, *Chem. Phys. Lipids*, 2008, **154**, 94–104.
24 G. Lecollinet, J. W. G. Annette Gulik, G. Mackenzie, T. Benvegnu and D. Plusquellec, *Chem.–Eur. J.*, 2002, **8**, 585–593.
25 T. Benvegnu, G. Lecollinet, J. Guilbot, M. Roussel, M. Brard and D. Plusquellec, *Polym. Int.*, 2003, **52**, 500–506.
26 M. Brard, W. Richter, T. Benvegnu and D. Plusquellec, *J. Am. Chem. Soc.*, 2004, **126**, 10003–10012.
27 A. Jacquemet, C. Mériadec, L. Lemiègre, F. Artzner and T. Benvegnu, *Langmuir*, 2012, **28**, 7591–7597.
28 Y. H. Kim, G. Leriche, K. Diraviyam, T. Koyanagi, K. Gao, D. Onofrei, J. Patterson, A. Guha, N. Gianneschi, G. P. Holland, M. K. Gilson, M. Mayer, D. Sept and J. Yang, *Sci. Adv.*, 2019, **5**, eaaw4783.
29 D. P. Brownholland, G. S. Longo, A. V. Struts, M. J. Justice, I. Szleifer, H. I. Petrache, M. F. Brown and D. H. Thompson, *Biophys. J.*, 2009, **97**, 2700–2709.
30 M. De Rosa, *Thin Solid Films*, 1996, **284–285**, 13–17.
31 G. Schwarzmann, B. Breiden and K. Sandhoff, *J. Lipid Res.*, 2015, **56**, 1861–1879.
32 T. Eguchi, K. Arakawa, K. Kakinuma, G. Rapp, S. Ghosh, Y. Nakatani and G. Ourisson, *Chem.–Eur. J.*, 2000, **6**, 3351–3358.
33 K. Arakawa, T. Eguchi and K. Kakinuma, *Chem. Lett.*, 2001, **30**, 440–441.
34 I. D. Falk, B. Gál, A. Bhattacharya, J. H. Wei, P. V. Welander, S. G. Boxer and N. Z. Burns, *Angew. Chem., Int. Ed.*, 2021, **60**, 17491–17496.
35 J. B. Weaver, C. Y. Lin, K. M. Faries, I. I. Mathews, S. Russi, D. Holten, C. Kirmaier and S. G. Boxer, *Proc. Natl. Acad. Sci. U. S. A.*, 2021, **118**, e2116439118.
36 R. J. Rawle, S. G. Boxer and P. M. Kasson, *Biophys. J.*, 2016, **111**, 123–131.
37 K. N. Liu and S. G. Boxer, *Biophys. J.*, 2020, **118**, 2426–2433.
38 M. Swain, J. R. Brisson, G. D. Sprott, F. P. Cooper and G. B. Patel, *Biochim. Biophys. Acta, Lipids Lipid Metab.*, 1997, **1345**, 56–64.
39 M. G. L. Elferink, J. G. de Wit, A. J. M. Driessen and W. N. Konings, *Eur. J. Biochem.*, 1993, **214**, 917–925.

40 J. A. Bouwstra, G. S. Gooris, W. Bras and H. Talsma, *Chem. Phys. Lipids*, 1993, **64**, 83–98.
41 J. F. Nagle and S. Tristram-Nagle, *Biochim. Biophys. Acta, Biomembr.*, 2000, **1469**, 159–195.
42 M. R. Brzustowicz and A. T. Brunger, *J. Appl. Crystallogr.*, 2005, **38**, 126–131.
43 F. R. Moss, S. R. Shuken, J. A. M. Mercer, C. M. Cohen, T. M. Weiss, S. G. Boxer and N. Z. Burns, *Proc. Natl. Acad. Sci. U. S. A.*, 2018, **115**, 9098–9103.
44 F. R. Moss, G. E. Cabrera, G. M. McKenna, G. J. Salerno, S. R. Shuken, M. L. Landry, T. M. Weiss, N. Z. Burns and S. G. Boxer, *ACS Chem. Biol.*, 2020, **15**, 2986–2995.
45 P. L. G. Chong, M. Zein, T. K. Khan and R. Winter, *J. Phys. Chem. B*, 2003, **107**, 8694–8700.
46 A. Bhattacharya, H. Niederholtmeyer, K. A. Podolsky, R. Bhattacharya, J.-J. Song, R. J. Brea, C.-H. Tsai, S. K. Sinha and N. K. Devaraj, *Proc. Natl. Acad. Sci. U. S. A.*, 2020, **117**, 18206–18215.
47 F. A. Heberle, M. Doktorova, H. L. Scott, A. D. Skinkle, M. N. Waxham and I. Levental, *Proc. Natl. Acad. Sci. U. S. A.*, 2020, **117**, 19943–19952.
48 A. Joardar, G. P. Pattnaik and H. Chakraborty, *J. Membr. Biol.*, 2022, **255**, 211–224.
49 C. V. Kulkarni, W. Wachter, G. Iglesias-Salto, S. Engelskirchen and S. Ahualli, *Phys. Chem. Chem. Phys.*, 2011, **13**, 3004–3021.
50 J. M. Seddon, G. Cevc and D. Marsh, *Biochemistry*, 1983, **22**, 1280–1289.
51 W. Helfrich, *Z. Naturforsch.*, 1978, **33**, 305–315.
52 A. Gulik, V. Luzzati, M. De Rosa and A. Gambacorta, *J. Mol. Biol.*, 1985, **182**, 131–149.
53 D. Marsh, *Handbook of Lipid Bilayers*, CRC Press, 2nd edn, 2013.
54 T. R. Galimzyanov, P. I. Kuzmin, P. Pohl and S. A. Akimov, *Soft Matter*, 2016, **12**, 2357–2364.
55 G. Leriche, D. Stengel, D. Onofrei, T. Koyanagi, G. P. Holland and J. Yang, *Sci. Rep.*, 2019, **9**, 19359.
56 S. Vidawati, J. Sitterberg, U. Bakowsky and U. Rothe, *Colloids Surf., B*, 2010, **78**, 303–309.
57 A. Relini, D. Cassinadri, Z. Mirghani, O. Brandt, A. Gambacorta, A. Trincone, M. De Rosa and A. Gliozzi, *Biochim. Biophys. Acta, Biomembr.*, 1994, **1194**, 17–24.
58 M. G. L. Elferink, J. Van Breemen, W. N. Konings, A. J. M. Driessen and J. Wilschut, *Chem. Phys. Lipids*, 1997, **88**, 37–43.
59 R. Kanichay, L. T. Boni, P. H. Cooke, T. K. Khan and P. L. G. Chong, *Archaea*, 2003, **1**, 175–183.
60 M. Kielian, *Annu. Rev. Virol.*, 2014, **1**, 171–189.
61 K. N. Liu and S. G. Boxer, *Biophys. J.*, 2021, **120**, 4832–4841.
62 W. Shinoda, K. Shinoda, T. Baba and M. Mikami, *Biophys. J.*, 2005, **89**, 3195–3202.
63 A. O. Chugunov, P. E. Volynsky, N. A. Krylov, I. A. Boldyrev and R. G. Efremov, *Sci. Rep.*, 2014, **4**, 7462.
64 A. C. Jacobsen, S. M. Jensen, G. Fricker, M. Brandl and A. H. Treusch, *Eur. J. Pharm. Sci.*, 2017, **108**, 101–110.
65 V. L. Sedlmayr, S. Schobesberger, S. Spitz, P. Ertl, D. J. Wurm, J. Quehenberger and O. Spadiut, *Eur. J. Pharm. Biopharm.*, 2024, **197**, 114213.
66 H. P. Rahn, J. Sun, Z. Li, R. M. Waymouth, R. Levy and P. A. Wender, *Biomacromolecules*, 2024, **25**, 4305–4316.
67 B. G. Tenchov, R. C. Macdonald and B. R. Lentz, *Biophys. J.*, 2013, **104**, 1029–1037.
68 S. T. Smrt, A. W. Draney and J. L. Lorieau, *J. Biol. Chem.*, 2015, **290**, 228–238.
69 E. R. J. Quemin, M. K. Pietilä, H. M. Oksanen, P. Forterre, W. I. C. Rijpstra, S. Schouten, D. H. Bamford, D. Prangishvili and M. Krupovic, *J. Virol.*, 2015, **89**, 11681–11691.

Supplementary Information

Structure-Function Relationships in Pure Archaeal Bipolar Tetraether Lipids

Ahanjit Bhattacharya,[a, b] Isaac D. Falk,[a] Frank R. Moss III,[c] Thomas M. Weiss,[d] Khoi N. Tran,[a] Noah Z. Burns,[a,] * Steven G. Boxer[a,*]

[a]Department of Chemistry, Stanford University, Stanford, CA 94305

[b]Stanford Center for Innovation in Global Health, Stanford University, Stanford, CA-94305

[c]Linac Coherent Light Source, SLAC National Accelerator Laboratory, Menlo Park, CA 94025

[d]Stanford Synchrotron Radiation Laboratory, SLAC National Accelerator Laboratory, Menlo Park, CA 94025

* Correspondence to: sboxer@stanford.edu, nburns@stanford.edu

Materials and Methods

Chemicals and general considerations

All organic synthesis reactions were conducted in oven-or flame-dried glassware under an atmosphere of nitrogen or argon unless otherwise noted. Commercial reagents and solvents were used as received unless otherwise noted with the exception of the following: DMF, toluene, tetrahydrofuran, methanol, benzene, and dichloromethane were dried by passing through a bed of activated alumina in a JC Meyer Solvent System. Glucosyl donor **Glc1** was prepared as described previously.[1] Flash column chromatography was performed using F60 silica gel (40-63 μm, 230-400 mesh, 60 Å) purchased from Silicycle. DPhPA, DPhPC, DoPhPC, DPhPG, dipalmitoyl phosphatidylcholine (DPPC), palmitoyl oleoyl phosphatidylcholine (POPC), dioleoyl phosphatidylethanolamine (DOPE), cholesterol, and 16:0 Biotinyl Cap PE were purchased from Avanti Polar Lipids (Alabaster, AL). DPhPC was purchased from Cayman Chemicals. Texas Red-1,2-dihexadecanoyl-*sn*-glycero-3-phosphoethanolamine (TR-DHPE), Atto 647N-DMPE, and NeutrAvidin were purchased from Thermo Fisher Scientific. Sulforhodamine B (SRB), pyranine (HPTS), disialoganglioside GD1a (from bovine brain), octyl glucoside, and Sepharose CL-4B were purchased from Sigma-Aldrich. Tris.HCl, HEPES buffer, buffer salts, sucrose, and glucose were obtained from Fisher Scientific and Sigma-Aldrich. Polydimethylsiloxane was obtained from Ellsworth Adhesives (Hayward, CA). Poly(L-lysine)-graft-poly(ethylene glycol) and Poly(L-lysine)-graft-poly(ethylene glycol) biotin were purchased from SuSoS (Dübendorf, Switzerland). Structures of various non-GDGT lipids described in this study are shown below:

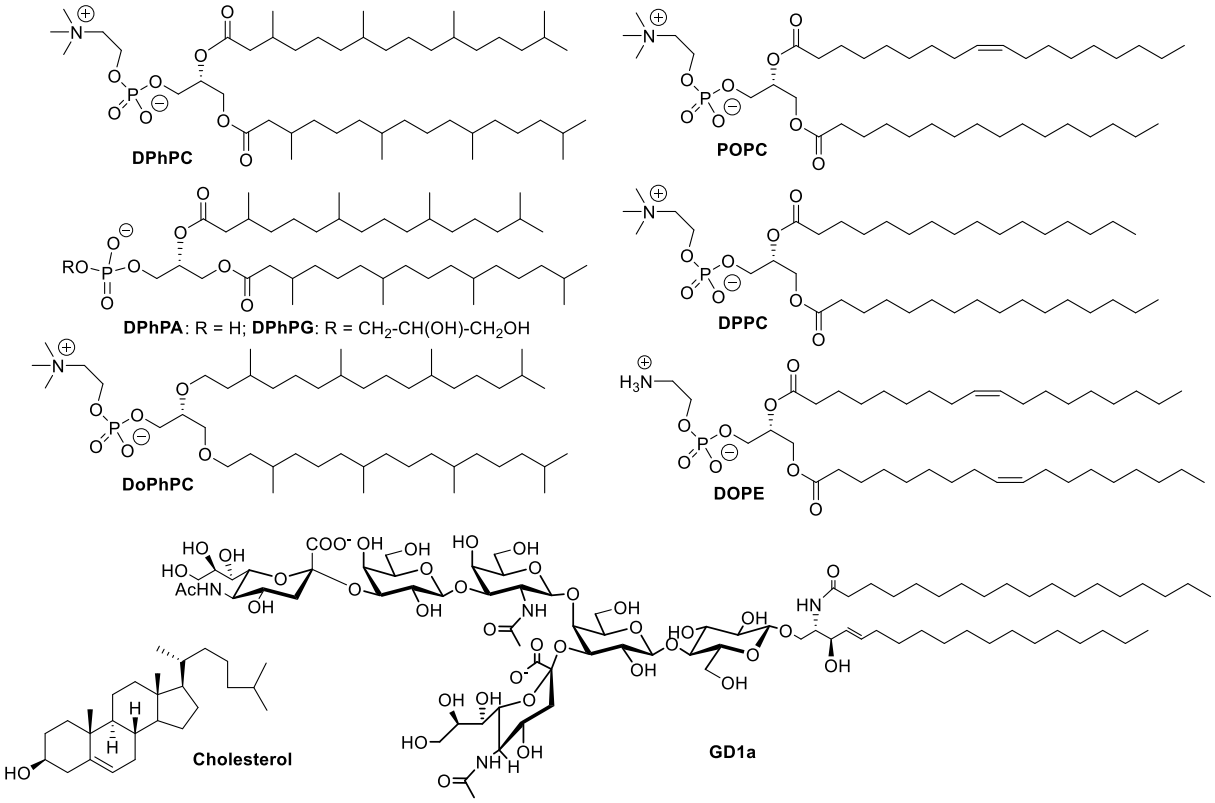

The following abbreviations have been used in synthetic methodologies for common words and phrases: RT – room temperature, sat. – saturated, equiv – equivalent, minute(s) – min, hour(s) – h.

Compound characterization

Proton nuclear magnetic resonance (^{1}H NMR), carbon nuclear magnetic resonance (^{13}C NMR), and phosphorus nuclear magnetic resonance spectra were recorded on Varian Inova 600, Varian Inova 500, or Varian Mercury 400 spectrometers operating respectively at 600, 500, and 400 MHz for ^{1}H and at 150, 125, and 100 MHz for ^{13}C and at 162 MHz for ^{31}P. Chemical shifts are reported in parts per million (ppm) with respect to residual protonated solvent for ^{1}H ($CHCl_3$ = δ 7.26, MeOH = δ 3.31) and with respect to carbon resonances of the solvent for ^{13}C ($CDCl_3$ = δ 77.0, CD_3OD = δ 49.0). Peak multiplicities are annotated as follows: app = apparent, br = broad, s = singlet, d = doublet, t = triplet, q = quartet, p = quintet, m = multiplet. Infrared (IR) spectra were recorded on a Nicolet 6700 FT-IR spectrometer. Optical rotations were measured using a JASCO P-2000 polarimeter. Standard HRMS data were collected on a Waters Micromass 70-VSE mass spectrometer, an Agilent QTOF tandem liquid chromatography-mass spectroscopy (LC-MS) instrument or a Micromass 70-VSE EI/CI/FD/FI mass spectrometer. Analytical thin-layer chromatography (TLC) was carried out on 250 μm 60-F_{254} silica gel plates purchased from EMD Millipore, and visualization was affected by observation of fluorescence-quenching with ultraviolet light and staining with *p*-anisaldehyde, phosphomolybdic acid with cerium sulfate (Seebach's stain), potassium permanganate ($KMnO_4$ stain), or cerium ammonium molybdate (CAM stain) as a developing agent.

Synthetic Procedures

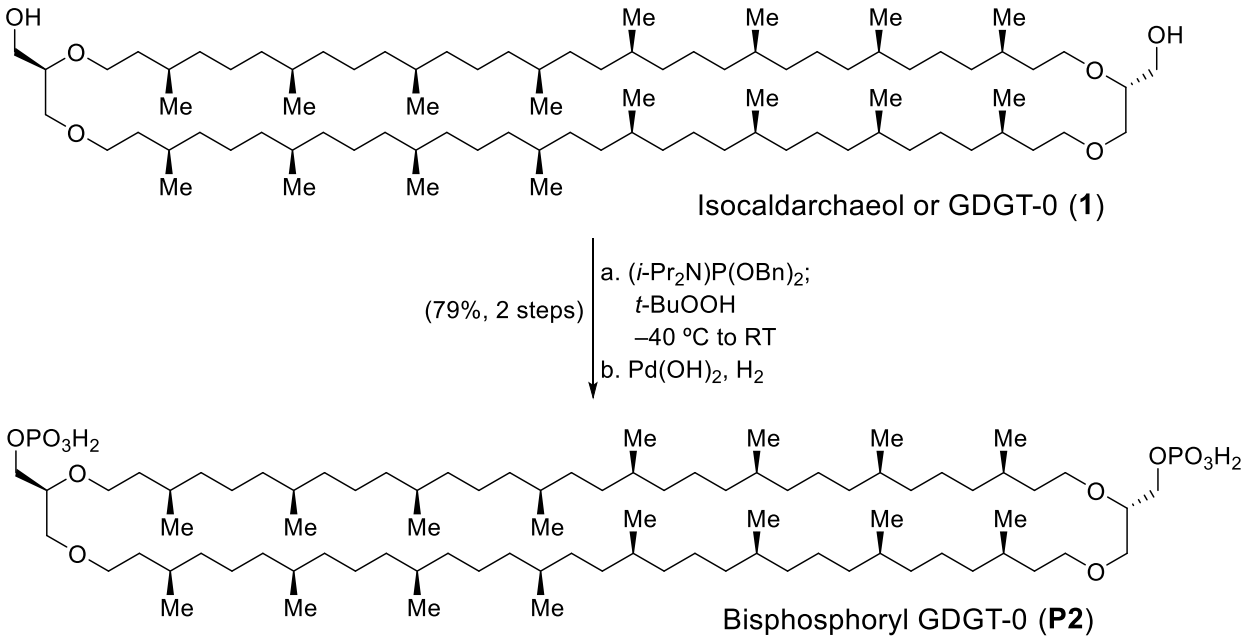

Scheme S1. Reaction scheme for synthesizing bisphosphoryl GDGT-0 (**P2**).

Bisphosphoryl GDGT-0 (**P2**) (Scheme S1): To a solution of GDGT-0 (**1**) (11.3 mg, 8.68 µmol, 1.0 equiv) in anhydrous and degassed CH_2Cl_2 (0.1 mL) in a screw cap vial was added a 0.45 M solution of tetrazole in acetonitrile (154 µL, 69.4 µmol, 8.0 equiv). To this solution was added dibenzyl *N,N*-diisopropylphosphoramidite (15.0 mg, 43.4 µmol, 5.0 equiv) as a solution in anhydrous and degassed CH_2Cl_2 (0.1 mL). The septum was replaced with a screw cap and the reaction was stirred at RT for approximately 14 h. The screw cap was replaced with a septum equipped with a balloon of argon and the reaction was cooled to -40 °C. A 5.5 M solution of *t*-butyl hydroperoxide in decane (31.6 µL, 174 µmol, 20.0 equiv) was added to the solution. The reaction was slowly warmed to RT over 4 h at which point TLC indicated full conversion. The reaction mixture was concentrated *in vacuo* and the crude residue was purified by preparative TLC on silica gel (35% EtOAc/hexanes, run twice) to afford the benzylated GDGT-0 bisphosphate (*structure not shown*) intermediate which was used directly in the next step.

The benzylated GDGT-0 bisphosphate was suspended in degassed and anhydrous solution of 1:1 THF/EtOH (1 mL). A small amount of 20% $Pd(OH)_2/C$ (~1 mg, 1.4 µmol, 0.16 equiv) was added to the solution and the reaction was sparged with H_2 for approximately 5 min after which the reaction was stirred under an atmosphere of H_2 for approximately 15 h. The reaction mixture was passed over a plug of celite with Et_2O and concentrated. The crude residue was purified using a column of Sephadex LH-20 (33-66% $CHCl_3$/MeOH) to afford the desired bisphosphoryl GDGT-0 (**P2**) (10.0 mg, 79% yield over two steps).

Spectroscopic data matched that reported in the literature.[2]

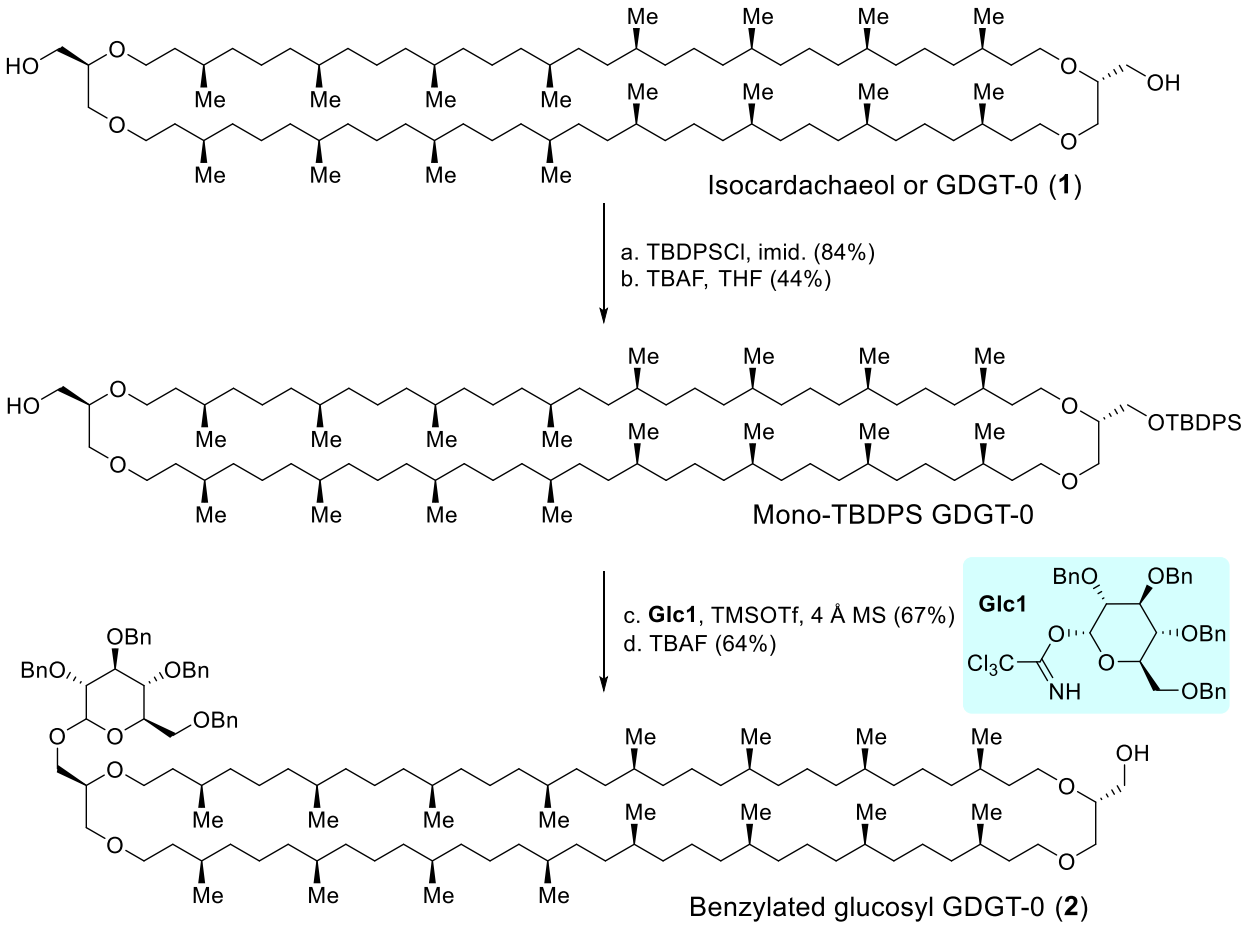

Scheme S2. Reaction scheme for synthesizing benzylated glucosyl GDGT-0 (**2**).

Benzylated glucosyl GDGT-0 (2) [Mixture of anomers]: (Scheme S2) To a solution of **1** (33.4 mg, 25.6 µmol, 1.0 equiv) in CH_2Cl_2 (0.2 mL) was added imidazole (6.9 mg, 103 µmol, 4.0 equiv) and *t*-butyl(chloro)diphenylsilane (20 µL, 76.9 µmol, 3.0 equiv). After stirring 15 h at RT, TLC indicated full conversion. The reaction mixture was diluted with CH_2Cl_2 (1 mL) and washed with 1 N HCl (1×1 mL), sat. aq. $NaHCO_3$ (1×1mL) and sat. aq. NaCl (1×1 mL). Each aqueous layer was extracted once with the same portion of CH_2Cl_2 (1×1 mL). The combined organic layers were dried over Na_2SO_4 and concentrated *in vacuo*. The crude residue was purified via flash column chromatography on silica gel (2-10% EtOAc/hexanes) to afford the desired bis-TBDPS GDGT-0 intermediate (38.4 mg, 84%) (*structure not shown*) which was used directly in the next step. The bis-TBDPS GDGT-0 (38.4 mg, 21.6 µmol, 1.0 equiv) was suspended in THF (1 mL) and a 0.1 M solution of TBAF in THF (216 µL, 21.6 µmol, 1.0 equiv) was added dropwise to the solution. The reaction was closely monitored by TLC (every 10 min) until the major species present was the desired mono-TBDPS GDGT-0 (approximately after 40 min of reaction). The reaction was quenched with a 1:1 mixture of sat. aq. $NaHCO_3$/sat. aq. NaCl (1×1 mL) and was extracted with EtOAc (3×1 mL). The combined organic layers were dried over Na_2SO_4 and concentrated *in vacuo*. The crude residue was purified using flash chromatography on silica gel (2-30% EtOAc/hexanes) to afford the desired mono-TBDPS GDGT-0 (14.7 mg, 44% yield) which was used directly in the next step. Bis-TBDPS GDGT-0 (~14 mg) and **1** (~7 mg) were also recovered from the reaction.

Mono-TBDPS GDGT-0 (14.7 mg, 8.59 μmol, 1.0 equiv) and **Glc1** (12.4 mg, 18.0 μmol, 2.1 equiv) were concentrated from toluene into a vial. 4 Å molecular sieves were added to the vial and the mixture was suspended in anhydrous CH_2Cl_2 (0.2 mL). To this solution was added a 1% v/v solution of TMSOTf in CH_2Cl_2 (15.9 μL, 0.859 μmol, 0.1 equiv). The reaction was stirred for 1.25 h at RT until TLC indicated full conversion. A few drops of Et_3N were then added to the reaction. The reaction mixture was directly purified via preparative TLC on silica (15% EtOAc/hexanes) to afford the TBDPS/benzylated glucosyl GDGT-0 (12.0 mg, 68%) (*structure not shown*) which was used directly in the next step.

The TBDPS/benzylated glucosyl GDGT-0 (12.0 mg, 5.82 μmol, 1.0 equiv) was dissolved in THF (1 mL) and a 1.0 M solution of TBAF in THF (29 μL, 29.1 μmol, 5.0 equiv) was added. After stirring at RT for 3 h, TLC indicated full conversion. The reaction mixture was diluted with EtOAc (1 mL) and washed with a 1:1 solution of sat. aq. $NaHCO_3$/sat. aq. NaCl (1×1 mL). The aqueous layer was further extracted with EtOAc (2×1 mL). The combined organic layers were dried over Na_2SO_4 and concentrated *in vacuo*. The resulting crude residue was purified using preparative TLC on silica gel (20% EtOAc/hexanes) to afford the benzylated glucosyl GDGT-0 (**2**) (6.8 mg, 64%, 1.6:1 ratio of α/β anomers as determined in the next step).

Physical Properties: Colorless oil

R_f = 0.23 (silica gel, 15% EtOAc/Hexanes, visualized CAM stain)

IR (film) 3444 (br), 2922, 2851,1712, 1456, 1376, 1260, 1093 (br), 1070, 803, 732, 696 cm^{-1}

^{1}H NMR (600 MHz, $CDCl_3$) δ 7.39-7.24 (m, 18H), 7.14 (t, *J* = 8.4 Hz, 2H), 5.02-4.40 (m, 9H), 3.97 (m, 1H), 3.87-3.39 (m, 23H), 2.14 (t, *J* = 6.3 Hz, 1H), 1.60 (m, 4H), 1.53 (m, 4H), 1.41-0.98 (m, 97H), 0.91-0.81 (m, 48H);

^{13}C NMR (126 MHz, $CDCl_3$) δ 138.90, 138.65, 138.56, 138.49, 138.42, 138.20, 138.16, 137.99, 128.36, 128.32, 128.26, 128.11, 127.94, 127.88, 127.87, 127.75, 127.70, 127.62, 127.56, 127.51, 103.91, 97.31, 84.69, 82.17, 82.01, 80.05, 78.35, 78.01, 77.84, 77.79, 77.65, 75.66, 75.61, 74.97, 74.89, 74.64, 73.50, 73.45, 72.80, 71.09, 70.92, 70.16, 70.08, 69.99, 69.92, 68.89, 68.83, 68.58, 68.48, 67.85, 63.08, 37.52, 37.40, 37.37, 37.13, 37.06, 36.71, 36.66, 36.58, 34.31, 33.06, 32.79, 29.92, 29.83, 29.79, 29.76, 29.69, 24.47, 24.40, 24.37, 19.83, 19.80 [Multiple signals are missing. There are multiple signals with greater intensity suggesting the contribution of multiple nuclei]

HRMS (ES+): calculated for $C_{120}H_{206}O_{11}Na$ $[M+Na]^+$ 1846.55, found 1846.55

$[\alpha]_D^{23}$ = +8.68 (c = 0.24, $CHCl_3$)

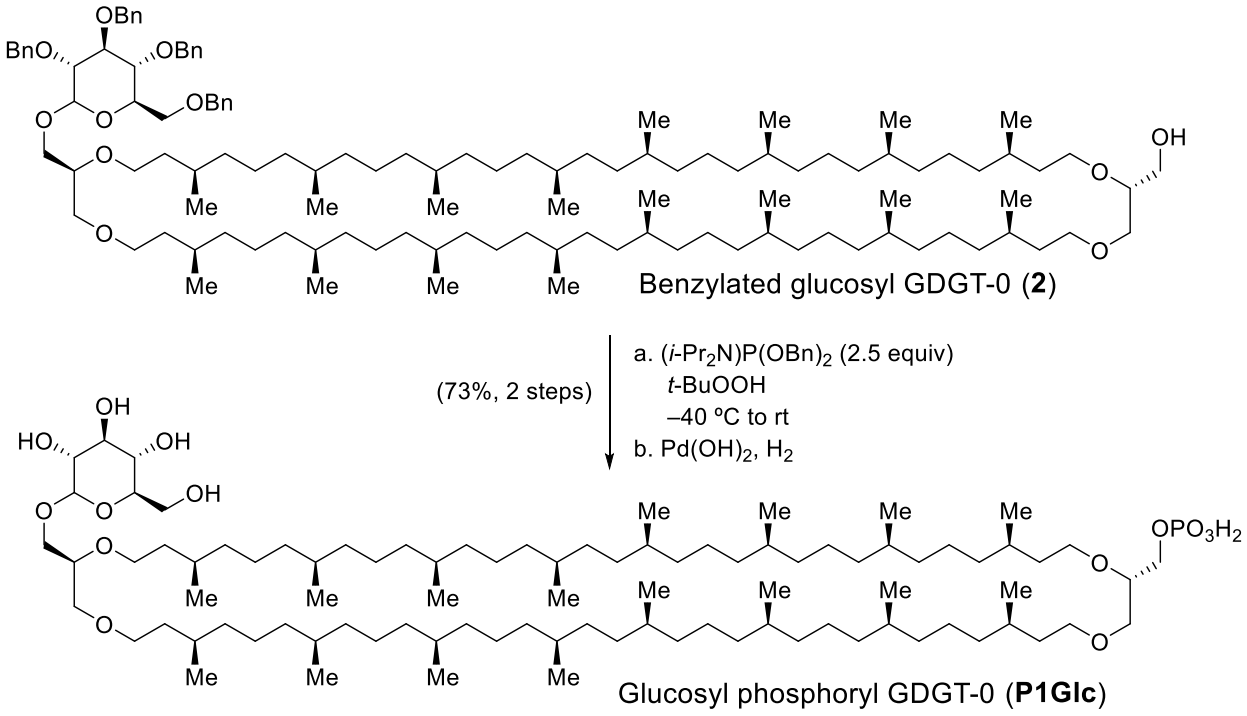

Scheme S3. Reaction scheme for synthesizing glucosyl phosphoryl GDGT-0 (**P1Glc**).

Glucosyl phosphoryl GDGT-0 (**P1Glc**) [Mixture of anomers] (Scheme S3): To a solution of benzylated glucosyl GDGT-0 (**2**) (6.8 mg, 3.7 µmol, 1.0 equiv) in anhydrous and degassed CH_2Cl_2 (0.1 mL) in a screw cap vial was added a 0.45 M solution of tetrazole in acetonitrile (33 µL, 15 µmol, 4.0 equiv). To this solution was added dibenzyl *N,N*-diisopropylphosphoramidite (3.2 mg, 9.3 µmol, 2.5 equiv) as a solution in anhydrous and degassed CH_2Cl_2 (0.1 mL) and the septum was replaced by a screw cap. The reaction was stirred at RT for ~15 h. TLC indicated full conversion and a balloon of argon gas was affixed to the vial. The reaction was subsequently cooled to -40 °C. To this solution was added a 5.5 M solution of *t*-butyl hydroperoxide in decane (10 µL, 54.4 µmol, 14.7 equiv). The reaction mixture was allowed to slowly warm to RT over 5 h. TLC indicated full conversion to the desired product and the reaction mixture was directly loaded onto a silica gel preparative TLC plate. The reaction was then purified using preparative TLC on silica gel (20% EtOAc/hexanes) to afford the benzyl-protected phosphate ester which was used directly in the next step.

The benzyl-protected phosphate ester was suspended in a 1:1 mixture of degassed THF/EtOH (1 mL). To the solution was added a small amount of 20% $Pd(OH)_2/C$ (~1 mg, 1.4 µmol, 0.38 equiv). H_2 was bubbled through the solution for 5 min and then the reaction was stirred under an atmosphere of H_2 for ~18 h. The reaction mixture was then passed over celite with MeOH and concentrated *in vacuo*. The crude residue was passed over a column of Sephadex LH-20 using 10% MeOH/$CHCl_3$ as the eluent to afford the desired product glucosyl GDGT-0 phosphate (**P1Glc**) (4.2 mg, 73% yield over 2 steps, 1.6:1 ratio of α/β anomers).

Physical Properties: Colourless oil (hygroscopic, forms white wax upon standing in air)

IR (film) 3393 (br), 2953, 2922, 2852, 1715, 1655, 1461, 1377, 1260, 1053 (br), 908, 801, 734

^{1}H NMR (600 MHz, 8:1 $CDCl_3/CD_3OD$) δ 4.74 (d, *J* = 3.6 Hz, 0.55H, α-anomer), 4.21 (d, *J* = 7.7 Hz, 0.33H β-anomer), 3.86 (m, 2H), 3.70 (m, 2H), 3.55 (m, 11H), 3.37 (m, 4H), 3.29 (m, 4H), 3.21 (m, 1H) [This region is partially obscured by the residual solvent signal of CD_3OD, attempts to

dissolve the sample in other common deuterated solvents were unsuccessful], 1.52 (m, 4H), 1.44 (m, 4H), 1.35-0.91 (m, 101H), 0.83-0.78 (m, 12H), 0.78-0.74 (m, 36H)

^{13}C NMR (126 MHz, 8:1 $CDCl_3/CD_3OD$) δ 103.25 (β-anomer), 98.76 (α-anomer), 77.67, 76.02, 75.77, 73.92, 73.37, 72.15, 71.65, 70.41, 70.20, 69.93, 69.81, 68.96, 68.75, 68.51, 67.01, 64.91, 61.66, 61.40, 37.31, 37.21, 36.73, 36.67, 36.46, 36.40, 34.11, 32.88, 32.61, 29.72, 29.59, 29.51, 24.29, 24.27, 24.23, 19.63, 19.58, 19.50, 19.47 (Due to limited amounts of material, signals were confirmed through HSQC) [Multiple signals are missing. There are multiple signals with greater intensity suggesting the contribution of multiple nuclei]

^{31}P NMR (162 MHz, 8:1 $CDCl_3/D_3COD$) δ 0.74

HRMS (ES+) calculated for $C_{92}H_{183}O_{14}NaP$ $[M+Na]^+$ 1566.33, found 1566.32

$[\alpha]_D^{23}$ = +4.1 (c = 0.1, 8:1 $CHCl_3$/MeOH)

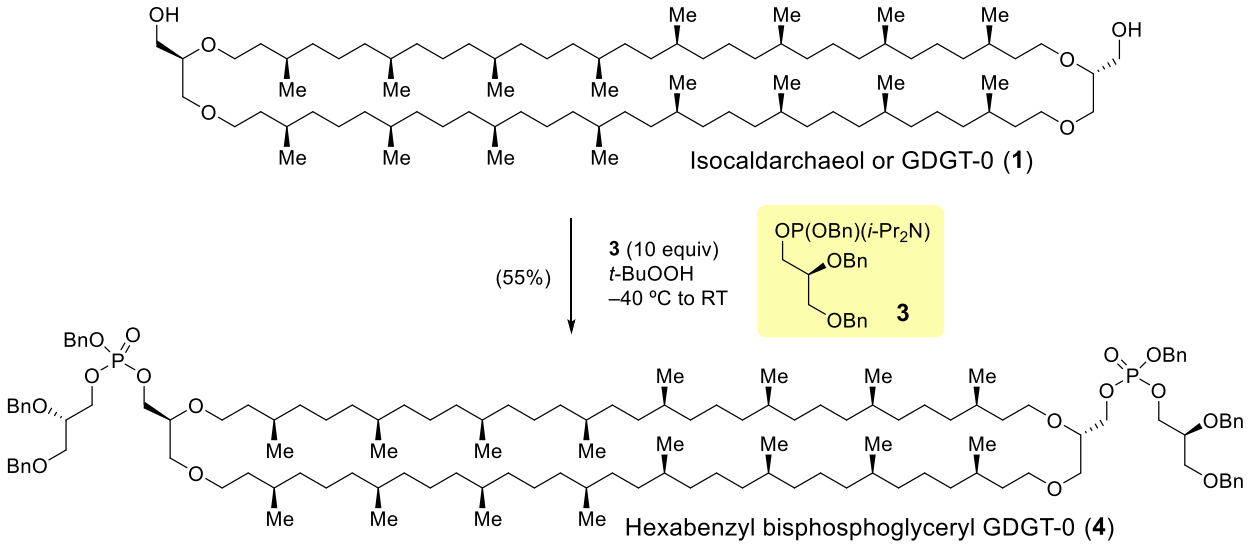

Scheme S4. Reaction scheme for synthesizing hexabenzyl bisphosphoglyceryl GDGT-0 (**4**).

Hexabenzyl bisphosphoglyceryl GDGT-0 (4) (Scheme 4): To a solution of GDGT-0 (**1**) (20.0 mg, 15.4 µmol, 1.0 equiv) in anhydrous CH_2Cl_2 (0.3 mL) in a screw cap vial was added phosphoramidite **3** (78.3 mg, 154 µmol, 10.0 equiv). To this solution was added 0.45 M solution of tetrazole in acetonitrile (600 µL, 270 µmol, 17.6 equiv) and the septum was replaced by a screw cap. The reaction was stirred at RT for ~15 h. TLC indicated full conversion and the reaction was cooled to -40 °C. To this solution was added a 5.5 M solution of *t*-butyl hydroperoxide in decane (84 µL, 460 µmol, 30 equiv). The reaction was allowed to stir at -40 °C and was then rapidly warmed to RT and allowed to react for another 3 h. The reaction mixture was concentrated *in vacuo* and directly loaded onto a silica gel preparative TLC plate. The reaction was then purified using preparative thin layer chromatography on silica gel (40% EtOAc/hexanes) to afford **4** (18.8 mg, 57% yield).

Physical Properties: Colourless oil

R_f = 0.45 (silica gel, 40% EtOAc/hexanes, visualized with CAM stain)

^{1}H NMR (600 MHz, $CDCl_3$) δ 7.40-7.20 (m, 30H), 5.05 (dd, *J* = 7.9, 4.7 Hz, 4H), 4.77-4.58 (m, 4H), 4.51 (d, *J* = 3.1 Hz, 4H), 4.22 (m, 2H), 4.18-3.95 (m, 6H), 3.86-3.75 (m, 2H), 3.65-3.49 (m, 10H), 3.43 (m, 8H), 1.68-1.44 (m, 10H), 1.43-0.97 (m, 94H), 0.85 (d, *J* = 6.4 Hz, 48H)

^{13}C NMR (126 MHz, $CDCl_3$) δ 138.12, 137.97, 135.94, 135.88, 128.52, 128.42, 128.36, 128.32, 127.84, 127.81, 127.73, 127.64, 127.58, 77.20, 76.57, 76.50, 73.42, 72.22, 70.03, 69.19, 69.16, 68.84, 67.07, 67.00, 66.93, 66.88, 37.52, 37.47, 37.40, 37.38, 36.96, 36.57, 34.29, 33.04, 32.78,

29.85, 29.65, 24.46, 24.37, 19.82, 19.77, 19.72, 19.69. [Multiple signals missing. There are multiple signals with greater intensity suggesting the contribution of multiple nuclei]
^{31}P NMR (162 MHz, $CDCl_3$) -0.86, -0.87. [Two peaks are observed due to diastereomers at phosphorus]
HRMS (ESI+); calculated for $C_{134}H_{224}O_{16}P_2$ $[M+2H]^{2+}$ 1075.8089, found 1075.8094
$[\alpha]_D^{23}$ = +0.87 (c = 0.63, $CHCl_3$)

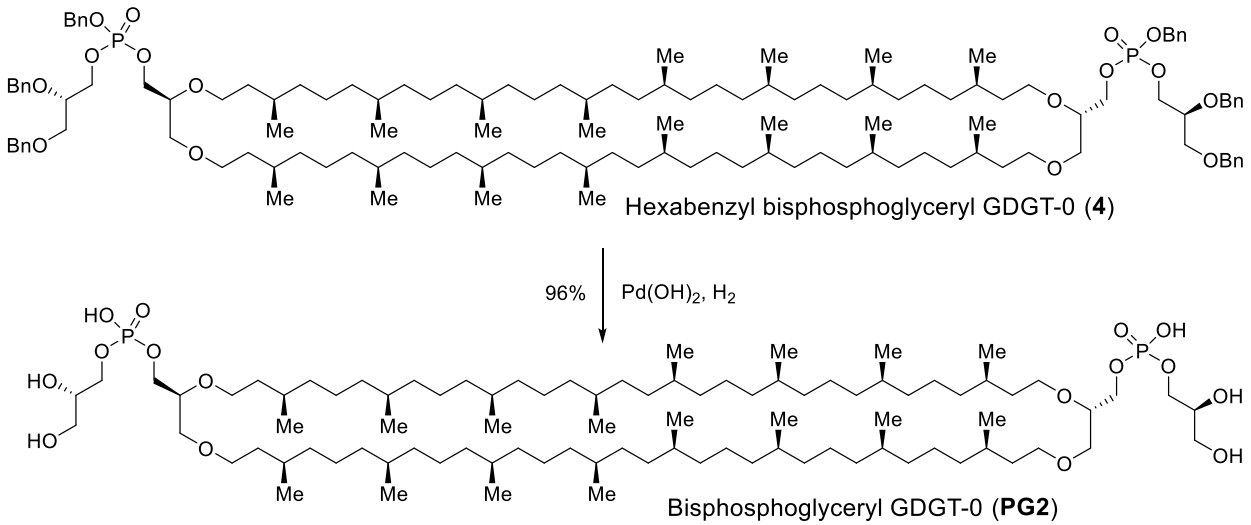

Scheme S5. Reaction scheme for synthesizing bisphosphoglyceryl GDGT-0 (**PG2**).

Bisphosphoglyceryl GDGT-0 (PG2) (Scheme 5): The benzyl-protected phosphate ester **4** (15 mg, 7.0 µmol, 1.0 equiv) was suspended in 1:1 THF/EtOH (2 mL). To the solution was added a small amount of 20% $Pd(OH)_2/C$ (~1 mg, 1.4 µmol, 0.2 equiv). H_2 was bubbled through the solution for 5 min and then the reaction was stirred under an atmosphere of H_2 for ~18 h. The reaction mixture was then passed over celite with CH_2Cl_2 and MeOH and concentrated *in vacuo*. The crude residue was passed over a column of Sephadex LH-20 using 50% MeOH/$CHCl_3$ as the eluent to afford the desired product bisphosphoglyceryl GDGT-0 (**PG2**) (10.8 mg, 96% yield).
Physical Properties: Colourless oil
^{1}H NMR (600 MHz, 1:2 $CDCl_3/CD_3OD$) δ 3.95-3.81 (m, 8H), 3.75 (p, *J* = 5.2 Hz, 2H), 3.71-3.54 (m, 12H), 3.54-3.45 (m, 6H), 1.58 (m, 9H), 1.44-1.16 (m, 74H), 1.09 (m, 27H), 0.87 (m, 48H)
^{13}C NMR (151 MHz,1:2 $CDCl_3/CD_3OD$) ^{13}C NMR (151 MHz, cd_3od) δ 78.72, 71.91, 71.75, 71.75, 70.25, 69.09, 66.77, 65.27, 65.27, 63.11, 63.11, 63.11, 37.88, 37.88, 37.54, 34.72, 34.72, 33.39, 33.39, 33.39, 32.40, 30.24, 30.07, 26.09, 24.93, 24.93, 24.93, 24.93, 23.10, 23.10, 20.11, 18.95, 14.13 δ [^{31}P coupling results in 12 shifts in the range of 60-80 ppm whereas 8 ^{13}C from the α-carbons are expected. Multiple signals are missing. There are multiple signals with greater intensity suggesting the contribution of multiple nuclei]
^{31}P NMR (162 MHz, 1:2 $CDCl_3/CD_3OD$) δ - 0.08
LRMS (ES–) calculated. for $C_{92}H_{185}O_{16}P_2$ $[M-H]^-$ 1608.3, found 1608.8
$[\alpha]_D^{23}$ = **–**3.49 (c = 0.29, 1:1 $CHCl_3$/MeOH)

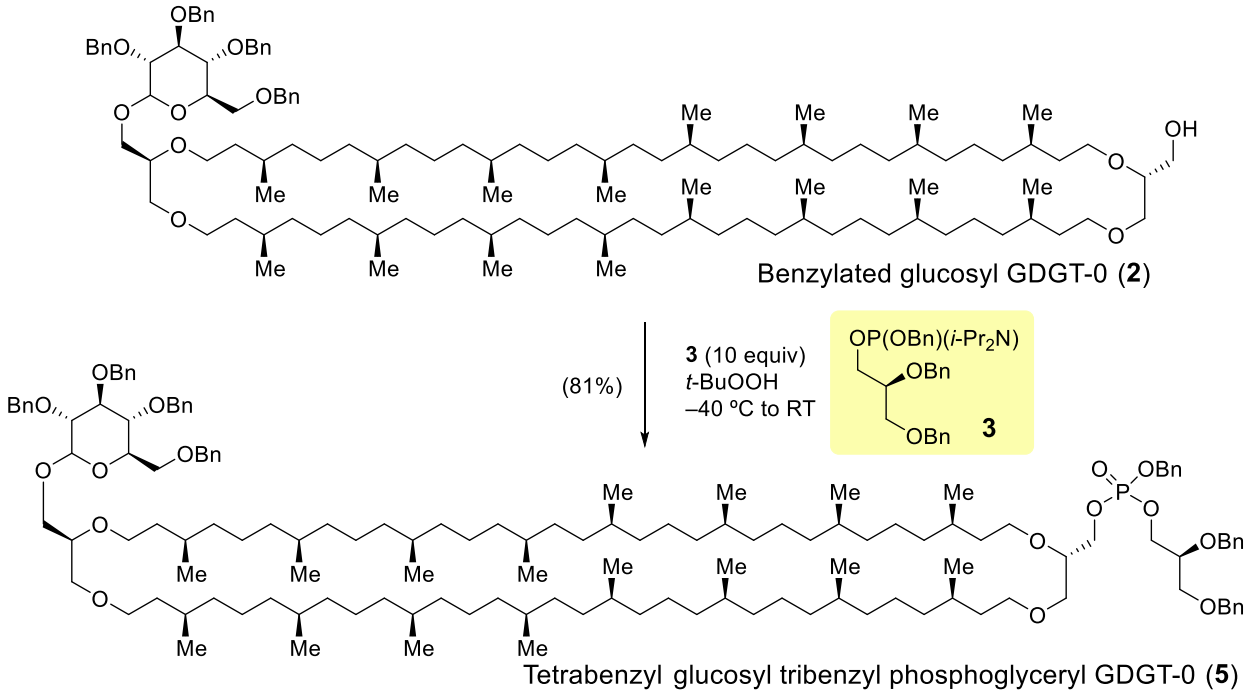

Scheme S6. Reaction scheme for synthesizing tetrabenzyl glucosyl tribenzyl phosphoglyceryl GDGT-0 (**5**).

Tetrabenzyl glucosyl tribenzyl phosphoglyceryl GDGT-0 (5) [Mixture of anomers] (Scheme S6): To a solution of benzylated glucosyl GDGT-0 (**2**) (7.0 mg, 3.8 µmol, 1.0 equiv) in anhydrous CH_2Cl_2 (0.1 mL) in a screw cap vial was added phosphoramidite **3** (20 mg, 38 µmol, 10.0 equiv). To this solution was added 0.45 M solution of tetrazole in acetonitrile (150 µL, 69 µmol, 18 equiv) and the septum was replaced by a screw cap. The reaction was stirred at room temperature for approximately 16 hours. TLC indicated full conversion and to this solution was added a 5.5 M solution of *t*-butyl hydroperoxide in decane (21 µL, 0.12 µmol, 30 equiv). After 20 min, the reaction mixture was directly loaded onto a silica gel preparative TLC plate and purified using 20% EtOAc/hexanes to afford **5** (7.0 mg, 81% Yield, 2:1 ratio of α/β anomers as determined in the next step).

Physical Properties: Colourless oil

^{1}H NMR (600 MHz, $CDCl_3$) δ 7.42-7.23 (m, 33H), 7.15 (m, 2H), 5.06-4.90 (m, 3H), 4.84-4.59 (m, 7H), 4.55-4.42 (m, 4H), 4.24-4.19 (m, 1H), 4.15-4.06 (m, 2H), 4.04-3.94 (m, 2H), 3.84-3.41 (m, 22H), 1.65-1.46 (m, 14H), 1.42-1.15 (m, 64H), 1.14-0.99 (m, 28H), 0.91-0.80 (m, 48H).

^{13}C NMR (101 MHz, $CDCl_3$) δ138.87, 138.62, 138.53, 138.46, 138.39, 138.13, 137.98, 137.95, 135.95, 128.53, 128.44, 128.37, 128.33, 128.31, 128.29, 128.26, 128.12, 127.94, 127.90, 127.87, 127.82, 127.75, 127.71, 127.65, 127.62, 127.59, 127.52, 103.90, 97.31, 84.67, 82.15, 82.00, 80.01, 77.99, 77.77, 77.61, 75.62, 74.98, 74.90, 74.65, 73.44, 72.81, 72.23, 70.92, 70.04, 69.97, 69.16, 68.86, 68.44, 67.83, 67.08, 66.90, 64.25, 37.53, 37.48, 37.39, 37.11, 36.96, 36.69, 36.58, 34.30, 33.05, 32.79, 29.85, 29.73, 29.66, 24.47, 24.38, 19.83, 19.78, 19.73, 19.70. [Multiple signals are missing. There are multiple signals with greater intensity suggesting the contribution of multiple nuclei]

^{31}P NMR (162 MHz, $CDCl_3$) δ -0.87, -0.88

HRMS (ES+) calculated for $C_{144}H_{236}NO_{16}P$ $[M+H+NH_4]^{2+}$ 1133.370550, found 1133.3723

$[\alpha]_D^{23}$ = +4.45 (c = 0.22, $CHCl_3$)

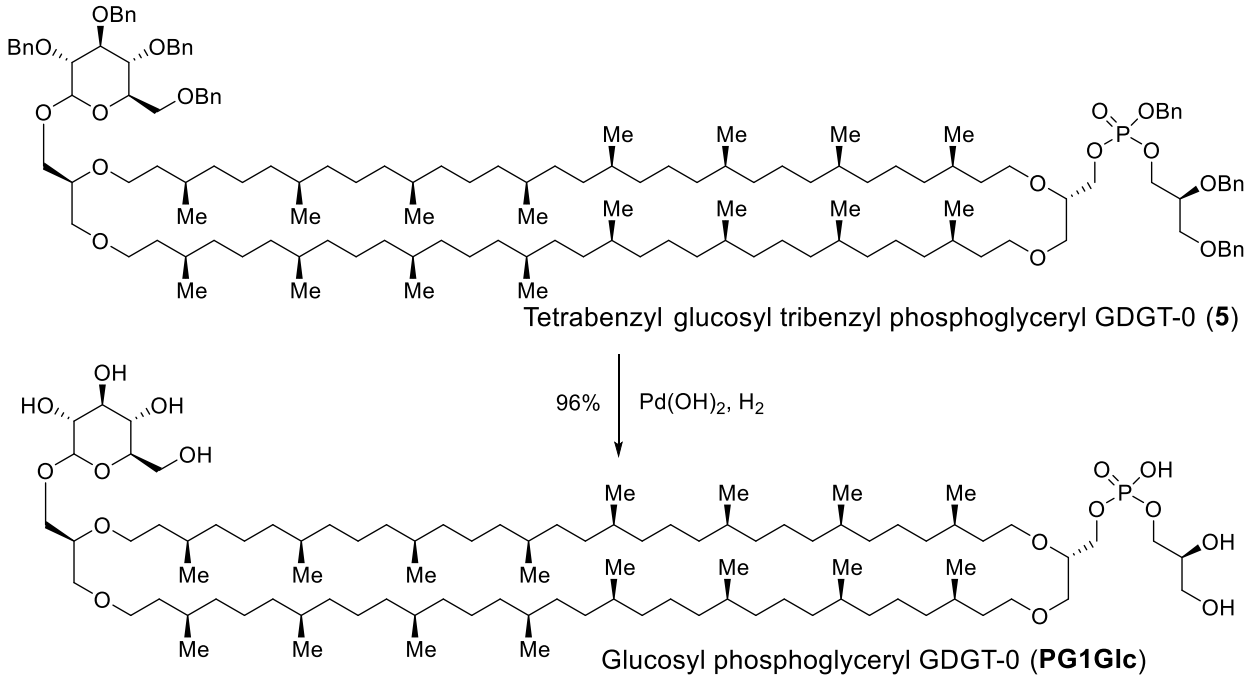

Scheme S7. Reaction scheme for synthesizing bisphosphoglyceryl GDGT-0 (**PG1Glc**).

Glucosyl phosphoglyceryl GDGT-0 (PG1Glc) [Mixture of anomers] (Scheme S7): The benzyl-protected phosphate ester **5** (15 mg, 7.0 μmol, 1.0 equiv) was suspended in a 1:1 mixture of THF/EtOH (2 mL). To the solution was added a small amount of 20% $Pd(OH)_2/C$ (~1 mg, 1.4 μmol, 0.2 equiv). H_2 was bubbled through the solution for 5 min and then the reaction was stirred under an atmosphere of H_2 for ~18 h. The reaction mixture was then passed over celite with CH_2Cl_2 and MeOH and concentrated *in vacuo*. The crude residue was passed over a column of Sephadex LH-20 using 50% MeOH/$CHCl_3$ as the eluent to afford the desired product **PG1Glc** (10.8 mg, 96% Yield, 2:1 ratio of α/β anomers).

Physical Properties: Colourless oil

^{1}H NMR (600 MHz, 1:1 $CDCl_3/CD_3OD$) δ 4.78 (d, *J* = 3.7 Hz, 0.60H, α-anomer), 4.26 (d, *J* = 7.7 Hz, 0.30H, β-anomer), 4.10-3.34 (m, 29H), 1.63-1.49 (m, 9H), 1.42-1.16 (m, 74H), 1.07 (m, 28H), 0.91-0.78 (m, 48H)

^{13}C NMR (151 MHz, 1:1 $CDCl_3/CD_3OD$) δ 103.79, 99.31, 78.22, 76.73, 76.56, 74.40, 74.40, 73.90, 72.74, 72.58, 72.41, 71.41, 71.08, 70.58, 70.25, 69.26, 69.09, 67.60, 67.43, 66.60, 65.77, 65.27, 63.61, 63.28, 61.95, 61.78, 61.62, 37.71, 37.54, 37.05, 34.56, 34.39, 33.06, 32.06, 30.07, 29.74, 25.76, 24.76, 24.76, 24.59, 24.59, 22.77, 22.77, 21.94, 19.94, 19.78, 18.95, 13.97 [Multiple signals are missing. There are multiple signals with greater intensity suggesting the contribution of multiple nuclei]

^{31}P NMR (162 MHz, 1:1 $CDCl_3/CD_3OD$) δ 0.56

HRMS (ES–) calc. For $C_{95}H_{188}O_{16}P$ $[M\text{-}H]^-$ 1616.3635, found 1616.3661

$[\alpha]_D^{23}$ = +3.65 (c = 0.195, 1:1 MeOH/$CHCl_3$)

Fitting of SAXS data from unilamellar vesicles

The buffer-subtracted and averaged data were fit using the model for unilamellar vesicles,[3] which is based on approximating the electron density of the bilayer by three Gaussian peaks corresponding to the inner and outer phosphate peak and a negative trough at the centre. The following equation was used for the fits:

$$I(q) = I_0 q^{-2} \sum_{i,j}^{n=3} (R_0 + \epsilon_i)\left(R_0 + \epsilon_j\right)\rho_i \rho_j \sigma_i \sigma_j \exp[-q^{-2}\left(\sigma_i^2 + \sigma_j^2\right)/2]\cos\left[q(\epsilon_i - \epsilon_j)\right] + a_0 + a_1 q \ldots (1)$$

where,

I_0: overall intensity of the measured profile

R_0: mean radius of the vesicle measured at the centre of the bilayer

ε: peak displacements from the bilayer centre

σ: Gaussian width of the peak

ρ: amplitude of the peak

a_0: constant background term

a_1: linear background term

The measured data were fit over the range q = 0.02 – 0.65 Å^{-1}. Data fitting was carried out based on a simulated annealing algorithm and the results were then further optimized using a non-linear least square algorithm, by using code from the open-source GNU scientific library project (https://www.gnu.org/software/gsl/). The fit parameters are summarized in Table S1.

Table S1: Fitting parameters of SAXS intensity profiles of GDGT lipids (Fig. 5A) that were used to generate the corresponding electron density profiles (Fig. 5B) according to Equation 1. The bilayer centre (ε_2) was fixed at 0. The head-to-head distances of the lipids in a membrane (d) are calculated as a difference between positions of peak maxima of the 1st (ε_1) and 3rd (ε_3) gaussians.

Lipid	ρ_1	ε_1 (Å)	σ_1 (Å)	ρ_2	σ_2 (Å)	ρ_3	ε_3 (Å)	σ_3 (Å)	I_0 (×10^{-7})	R_0 (Å)	a_0	a_1	χ^2/DOF	d = ε_3 - ε_1 (Å)
P2	1.98 ± 0.04	-19.0 ± 0.38	4.57 ± 0.09	-0.84 ± 0.02	10.7 ± 0.22	4.77 ± 0.10	20.8 ± 0.42	1.00 ± 0.02	5.12 ± 0.10	55.9 ± 1.00	0.29 ± 0.01	0.13 ± 0.00	0.08	39.8 ± 0.80
P1Glc	1.41 ± 0.03	-22.7 ± 0.44	5.00 ± 0.10	-0.84 ± 0.02	11.7 ± 0.24	7.41 ± 0.16	16.4 ± 0.34	0.90 ± 0.02	0.35 ± 0.01	47.6 ± 1.00	0.12 ± 0.00	0.00 ± 0.00	0.01	39.1 ± 0.78
PG2	0.88 ± 0.02	-17.4 ± 0.38	5.40 ± 0.10	-0.60 ± 0.02	10.7 ± 0.20	2.11 ± 0.03	21.3 ± 0.40	1.58 ± 0.01	5.27 ± 0.10	77.8 ± 1.00	0.71 ± 0.01	0.13 ± 0.00	0.08	38.7 ± 0.78
PG1Glc	1.53 ± 0.03	-18.3 ± 0.36	5.01 ± 0.10	-0.99 ± 0.02	10.7 ± 0.22	3.55 ± 0.06	20.2 ± 0.42	1.59 ± 0.04	1.15 ± 0.02	57.1 ± 1.00	0.22 ± 0.00	0.01 ± 0.00	0.01	38.5 ± 0.78

Supplementary Figures

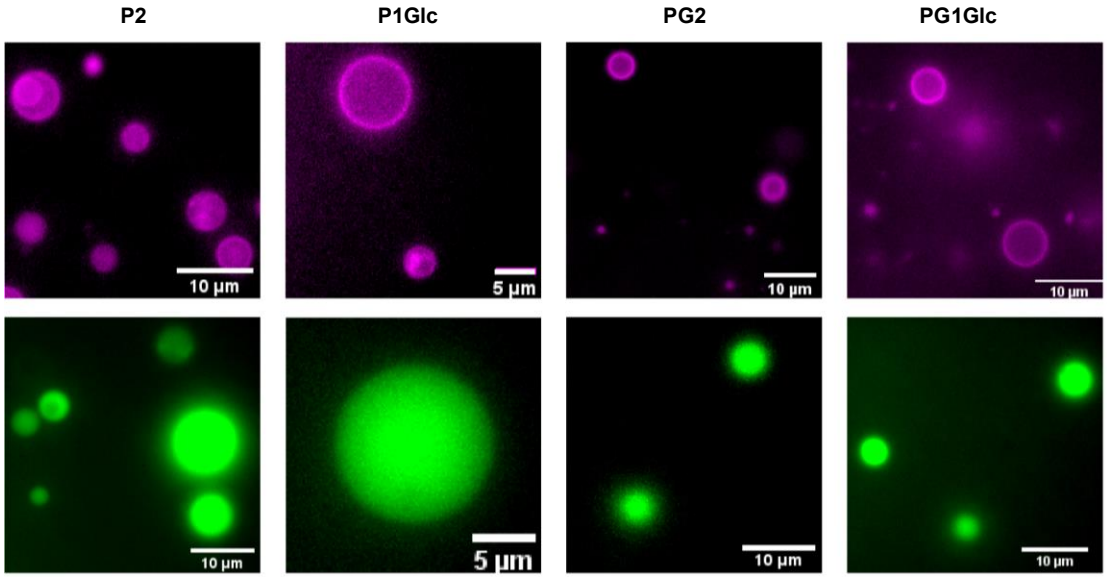

Fig. S1 Microscopy images of giant vesicles of GDGT lipids formed by gentle hydration of a thin lipid film in Tris buffer (50 mM, pH 7.5). *Upper panel*: membranes are stained by the lipophilic dye Texas Red-DHPE incorporated at 0.1 mol%. *Lower panel*: encapsulation of water-soluble dye pyranine (0.5 mM) in the interior of vesicles.

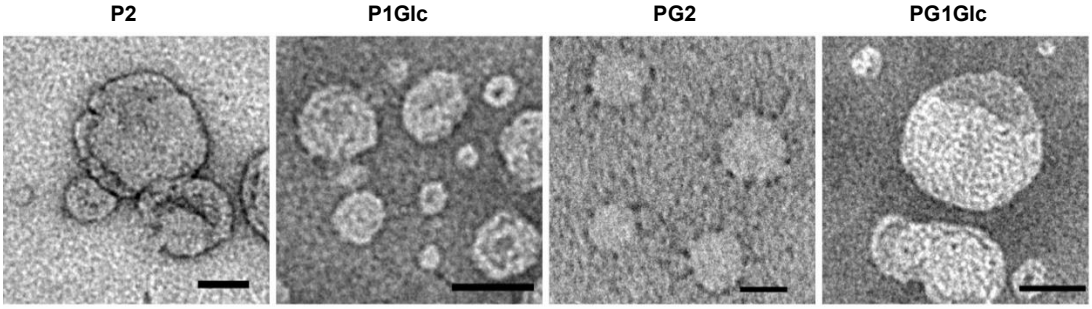

Fig. S2 Negative-staining electron microscopy images of vesicles of GDGT lipids obtained via extrusion (**P2**, **PG2**, **PG1Glc**) or ultrasonication (**P1Glc**) of multilamellar dispersions. All scale bars correspond to 50 nm.

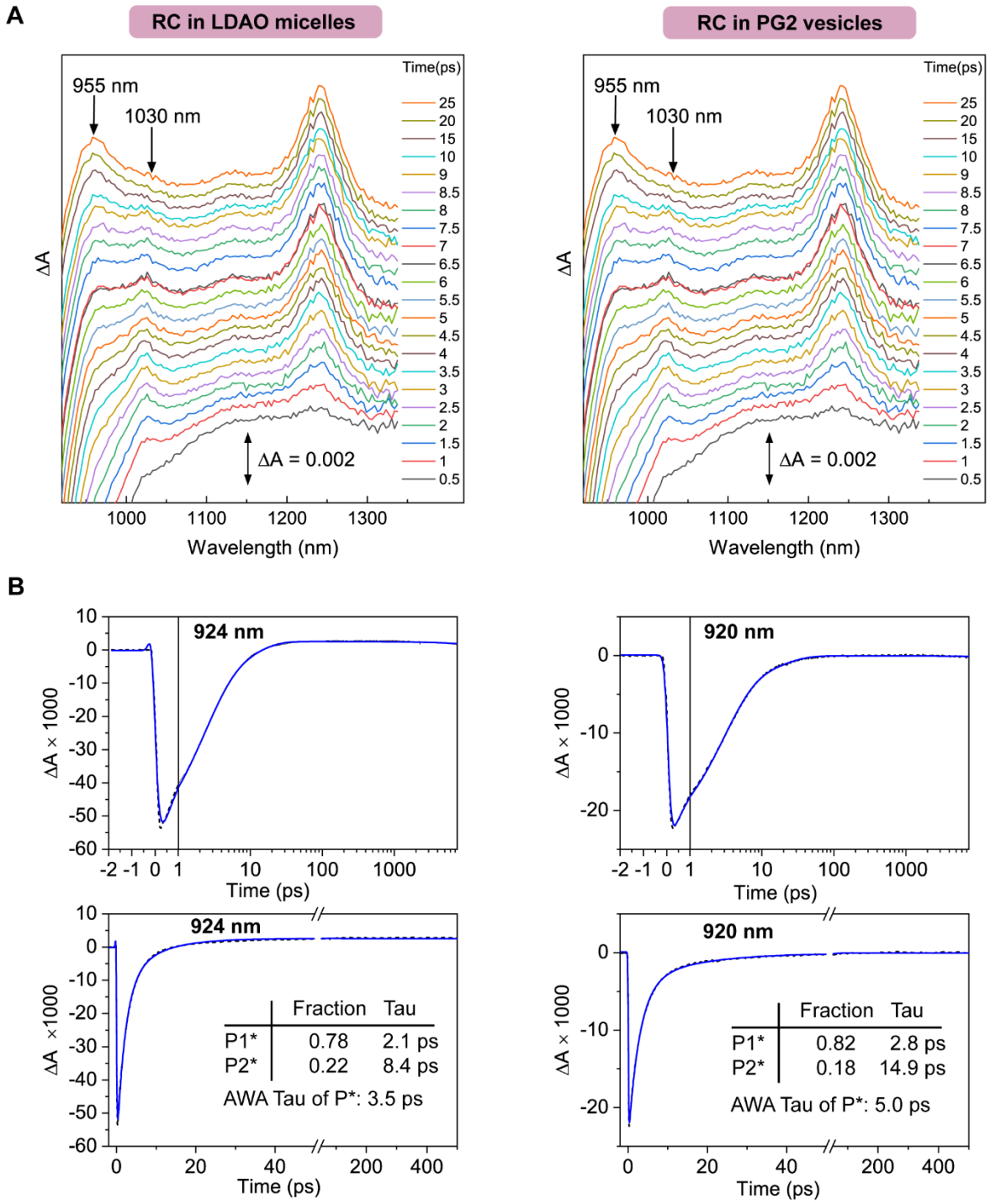

Fig. S3 Ultrafast transient absorption spectroscopy of bacterial (*Rhodobacter spheroides*) photosynthetic reaction centres (M252V mutant which assembles without Q_A) in archaeal lipid vesicles at 295 K. **A**. Time evolution of the near IR spectra at 0.5-25 ps. In both panels, there is a clear band around 1030 nm, which is characteristic of B_A^-, the primary charge transfer intermediate in RC. The difference in signal intensity is most likely due to the difference in concentration. **B**. The two panels show single wavelength kinetics fit at 920 nm for P* stimulated emission decay characterized by the lifetime tau. As P* → $P^+B_A^-$, the decay of P* corresponds to

the formation of B_A^-, hence giving the kinetics of the primary charge transfer process. The lifetimes of the two P* populations in both samples as well as the amplitude-weighted-average (AWA) lifetime are very similar between two samples, indicating that reconstitution into archaeal lipid had negligible effects on the charge transfer process of the RC.

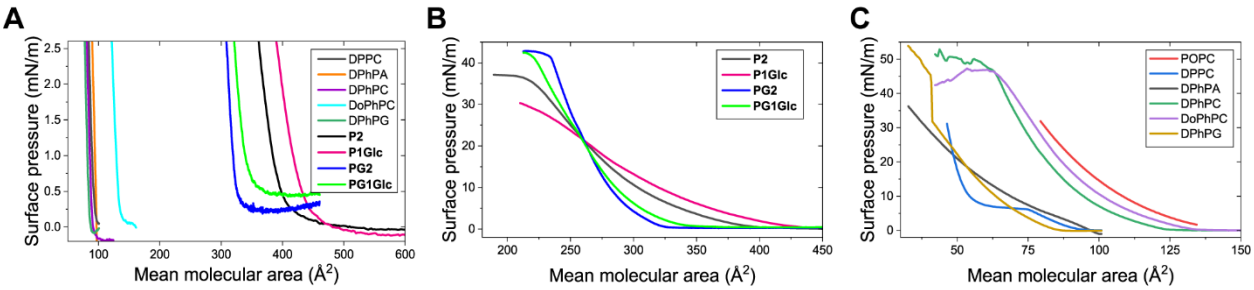

Fig. S4 Expanded plots of surface pressure-area (π-A) isotherms of GDGTs and other lipids. **A**. Lift-off areas (A_0) were calculated by extrapolating the linear regions of the isotherms in the range of surface pressure (π) = 0.5-2.5 mN/m to zero surface pressure. **B**. Zoomed in plot of the π-A isotherms of bipolar lipids described in this study. **C**. Zoomed in plot of the π-A isotherms of the monopolar lipids described in this study.

A

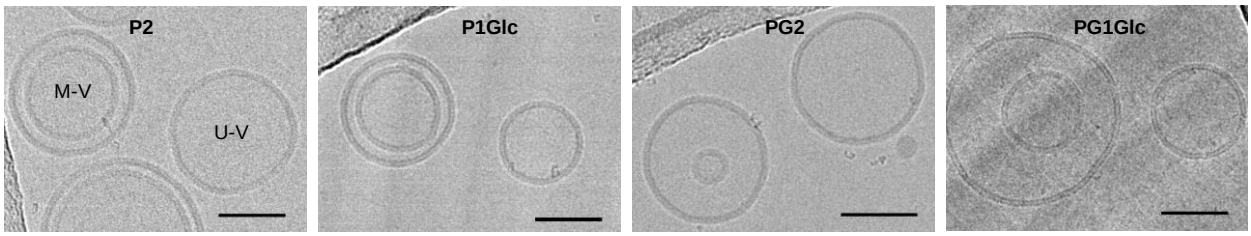

B

Lipid	Uni-vesicular (U-V) %	Multi-vesicular (M-V) %
P2 (67)	36	64
P1Glc (29)	76	24
PG2 (53)	58	42
PG1Glc (51)	76	24

C

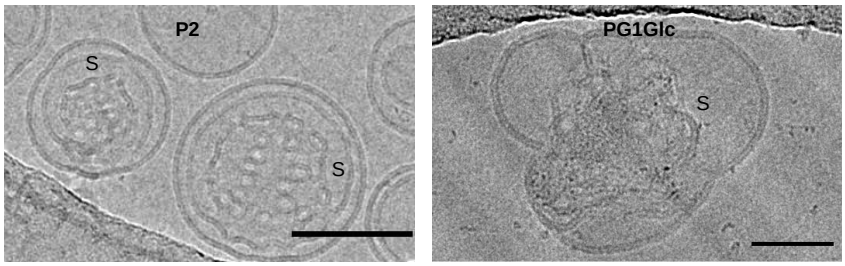

Fig. S5 Cryogenic electron microscopy images of vesicles and other lipidic structures of GDGTs formed in Tris buffer (50 mM, pH 7.5). **A**. Images of unilamellar vesicles: U-V and M-V denote uni-vesicular and multi-vesicular architectures. **B**. Percentages of uni-vesicular and multi-vesicular structures imaged for each lipid. The numbers in parentheses indicate the number of vesicles analysed. **C**. Example of sponge-like structures (denoted by 'S') observed in vesicles of **P2** and **PG1Glc**. All scale bars represent 50 nm.

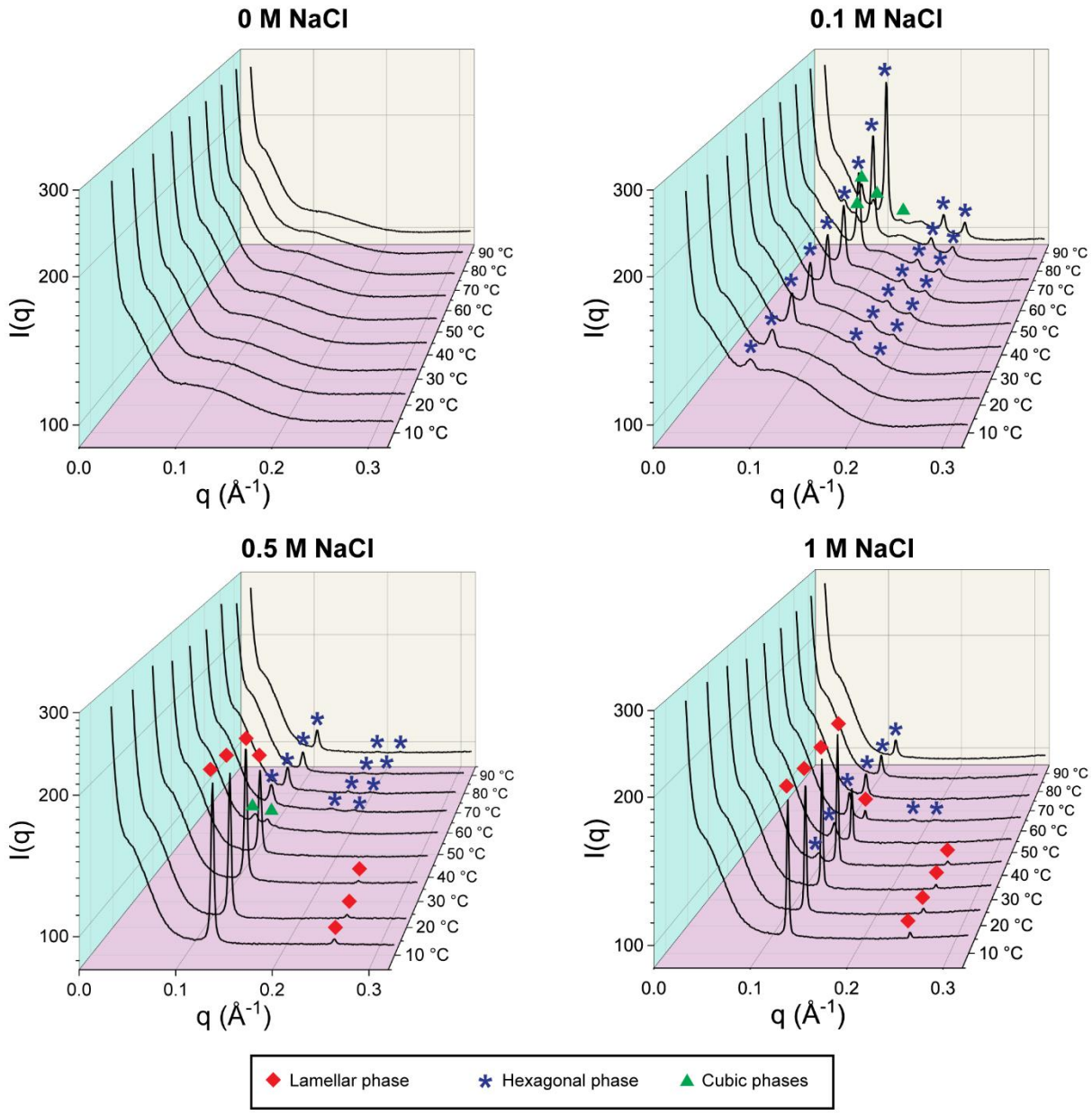

Fig. S6 SAXS intensity profiles of bulk dispersions of **P2** in Tris buffer (50 mM, pH 7.5) containing variable concentrations of salt (NaCl) over 10-90 °C.

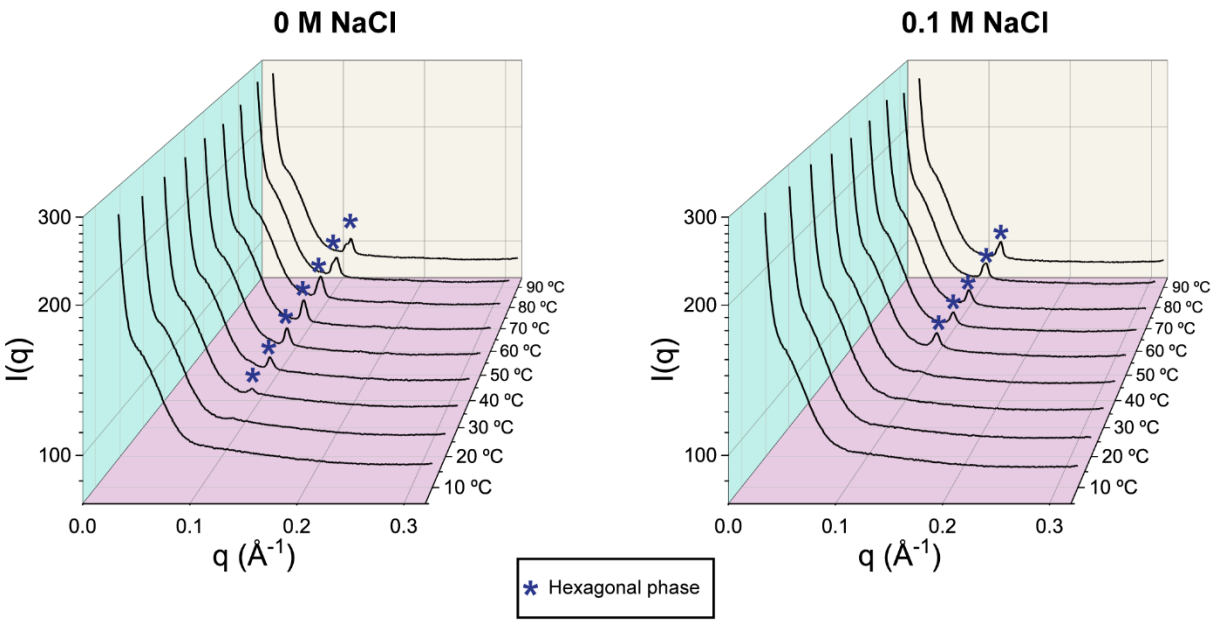

Fig. S7 SAXS intensity profiles of bulk dispersions of **P1Glc** in Tris buffer (50 mM, pH 7.5) containing variable concentrations of salt (NaCl) over 10-90 °C. The lipid films could not be dispersed at salt concentrations above 0.1 M NaCl.

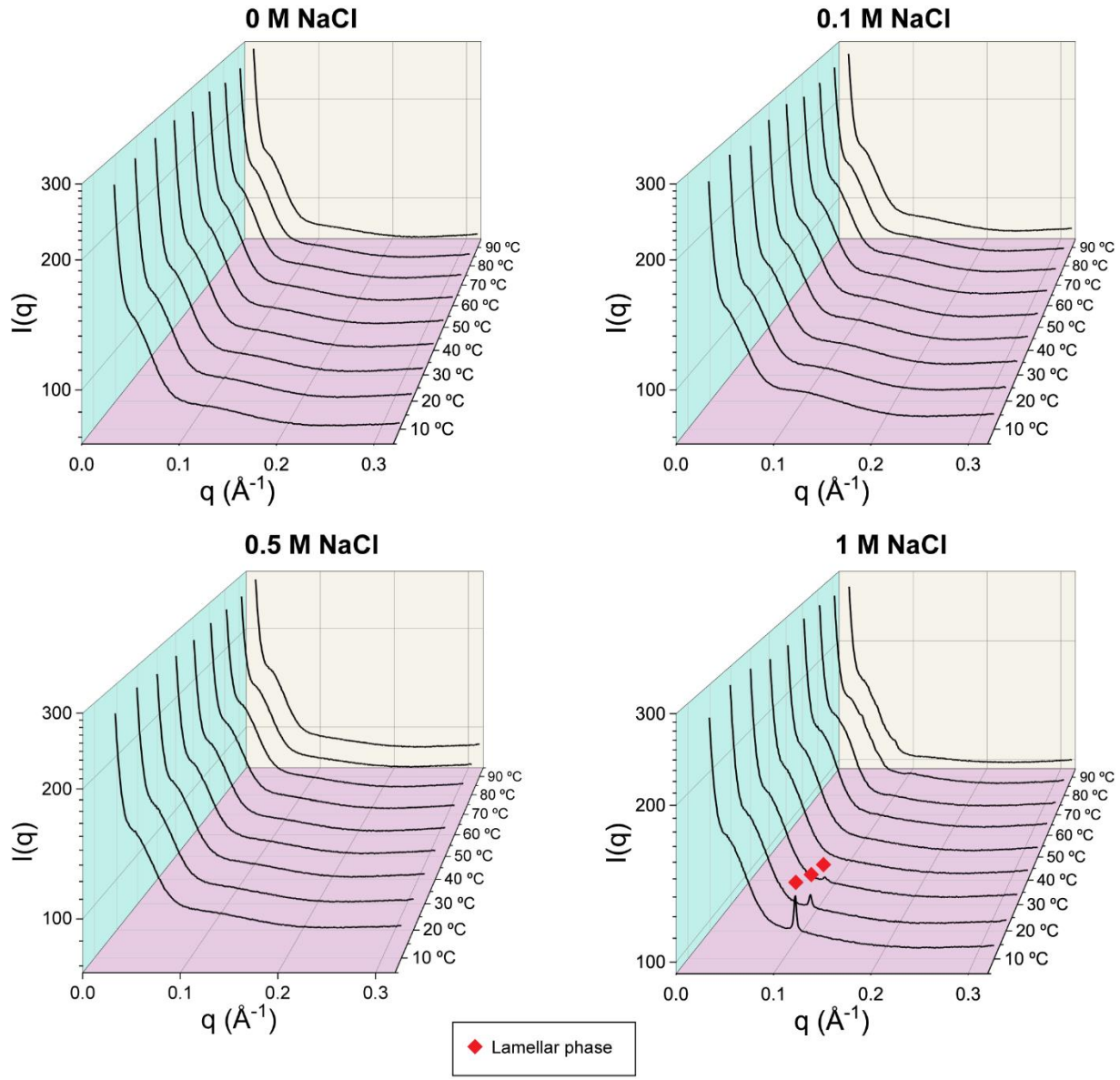

Fig. S8 SAXS intensity profiles of bulk dispersions of **PG2** in Tris buffer (50 mM, pH 7.5) containing variable concentrations of salt (NaCl) over 10-90 °C.

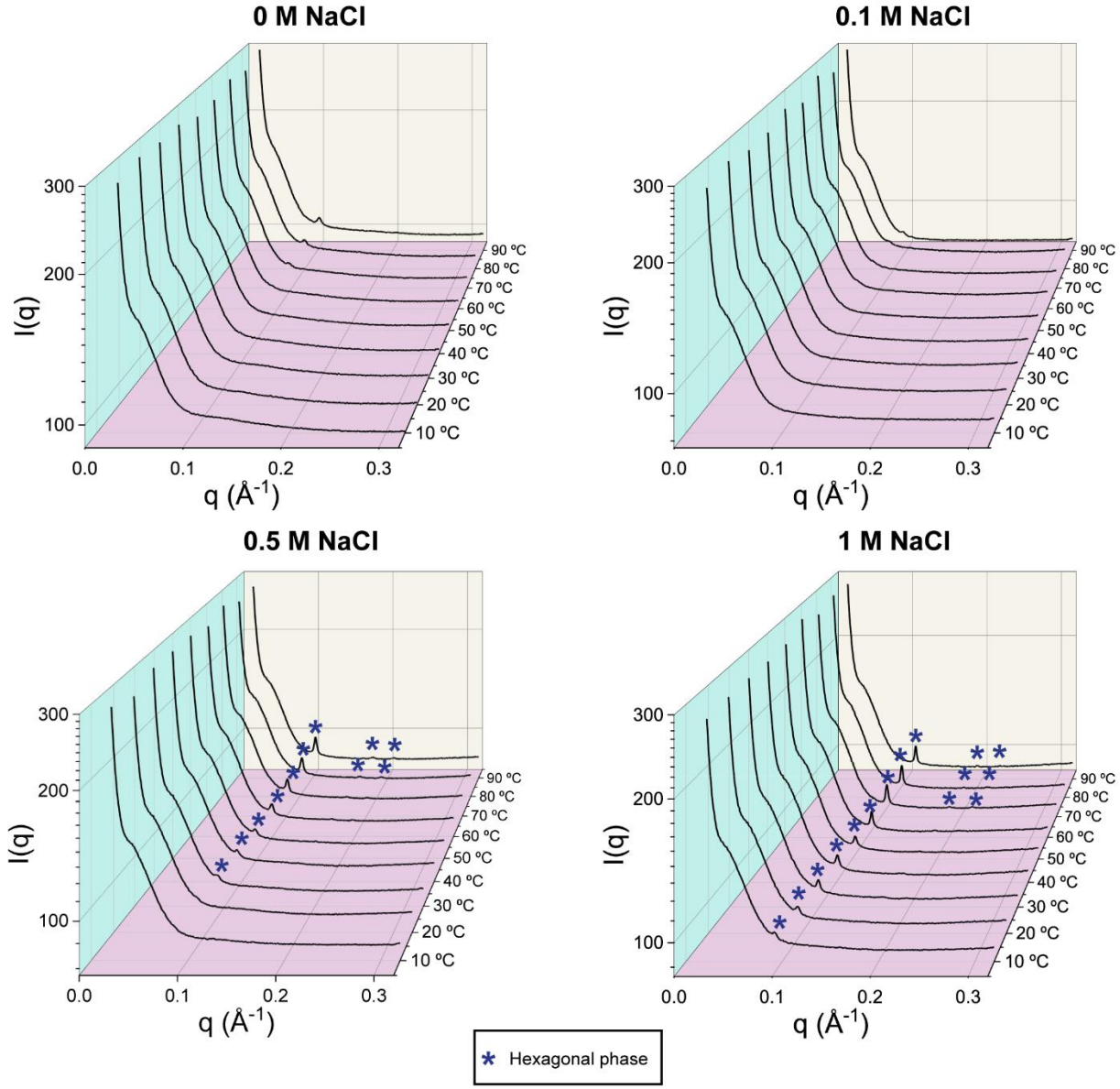

Fig. S9 SAXS intensity profiles of bulk dispersions of **PG1GlcC** in Tris buffer (50 mM, pH 7.5) containing variable concentrations of salt (NaCl) over 10-90 °C.

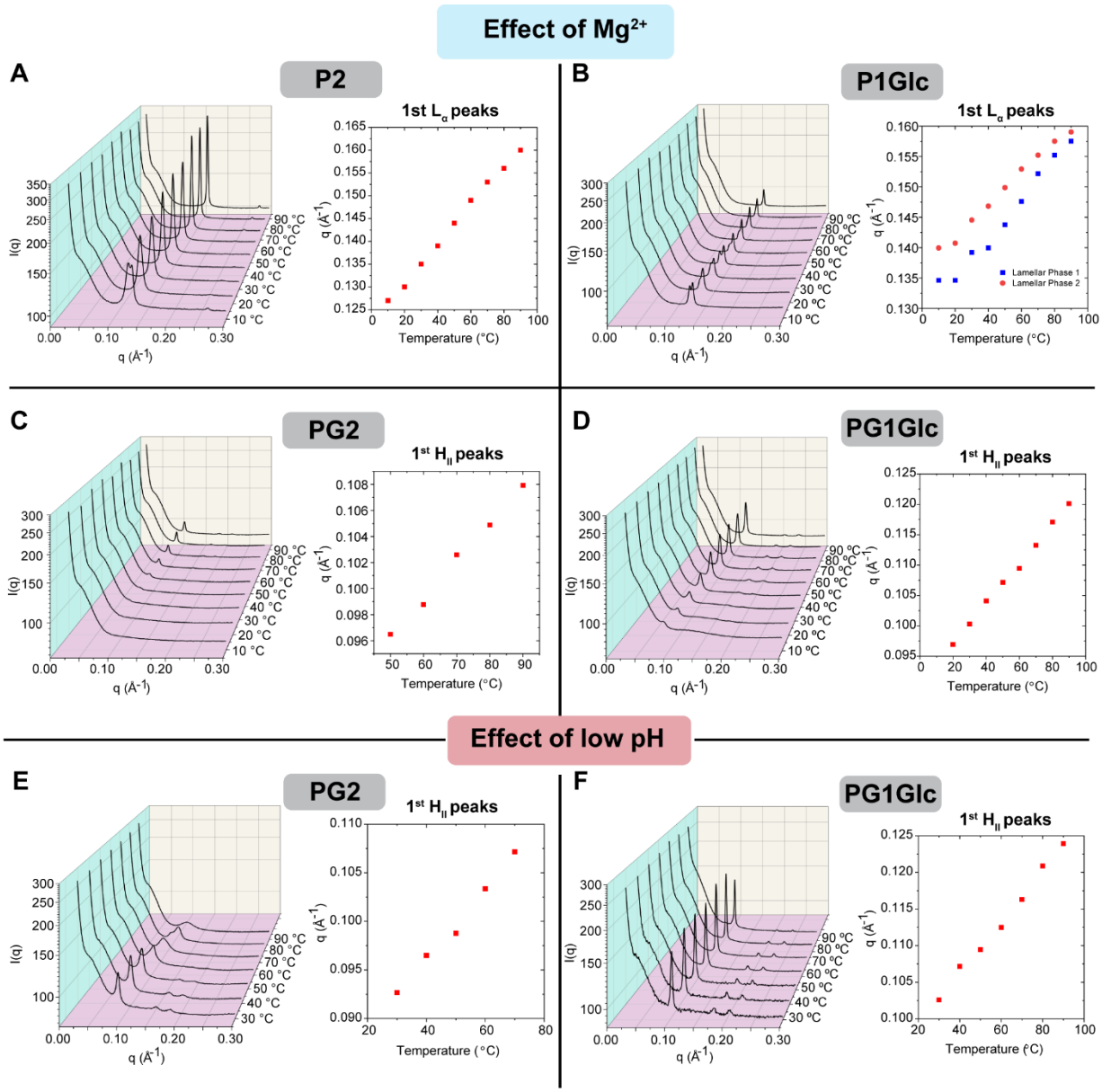

Fig. S10 Small-angle X-ray scattering (SAXS) on bulk dispersions of GDGT lipids in presence of magnesium ions ($MgCl_2$) (**A**, **B**, **C**, **D**) over 10-90 °C and low pH (2.8) (**E**, **F**) over 30-90 °C. Lipidic mesophases such as lamellar (L_α, 1:2:3:4) and inverse hexagonal (H_{II}, 1:√3:√4) were identified from the characteristic ratios of the q-values of the Bragg peaks in the intensity profiles. In all cases, the peak positions (q-value) of the 1st characteristic mesophase peak were found to increase with temperature, likely due to increasing dehydration.

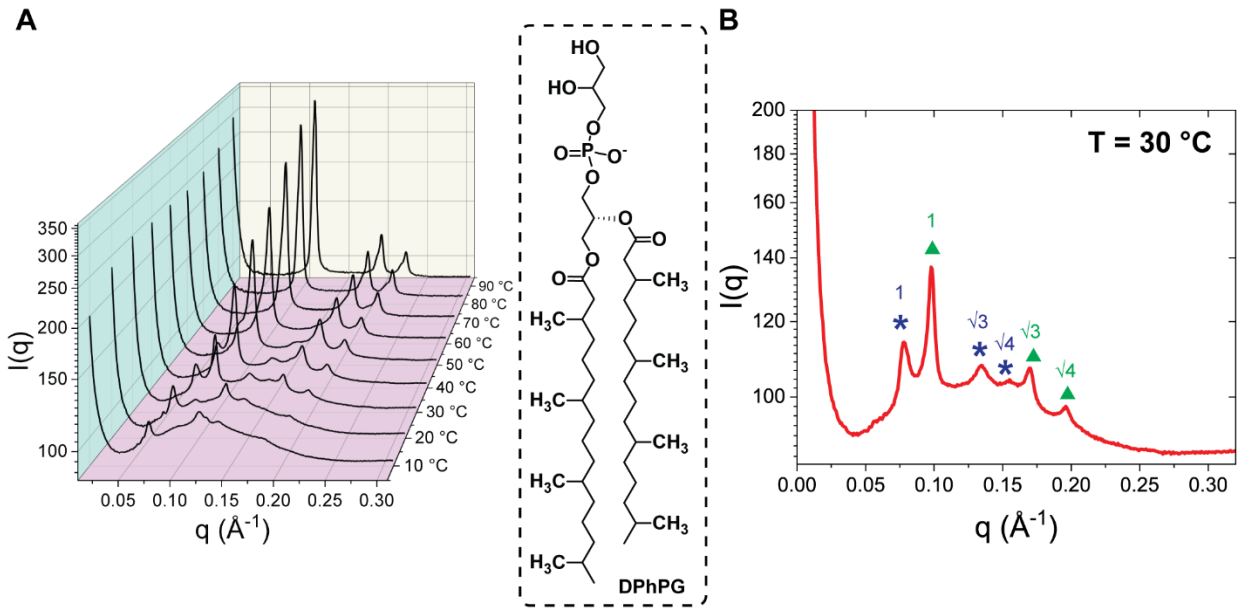

Fig. S11 Mg^{2+}-induced mesophase formation in DPhPG. **A**. SAXS intensity profiles of DPhPG dispersed in Tris buffer (pH 7.5) containing 10 mM Mg^{2+} over 10-90 °C. **B**. The intensity profile for 30 °C is shown in enlarged form to show co-existence of two sets of hexagonal phase peaks (at ratio of 1:√3:√4) – indicated by asterisk (*) and triangles (▲).

100 mol% mix	DPhPG:GD1a:Biotin-DPPE:Atto 47N-DMPE (99.45:0.4:0.1:0.05)
1 mol% mix	**PG2**:DPhPG:GD1a:Biotin-DPPE:Atto 647N-DMPE (99:0.5:0.4:0.1:0.05)
0.5 mol% mix	**PG2**:GD1a:Biotin-DPPE:Atto 647N-DMPE (99.45:0.4:0.1:0.05)

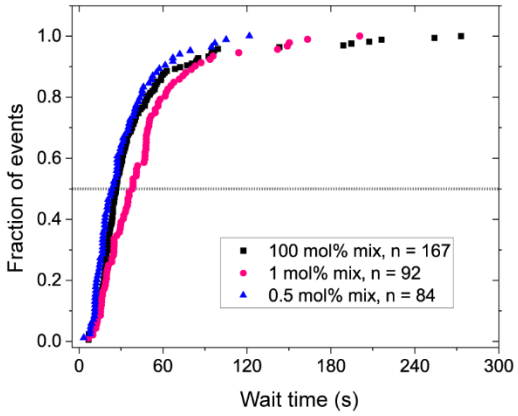

Fig. S12 Acidic pH-induced fusion of influenza virus particles with 100 nm vesicles containing varying mol percentages of monopolar lipids (100, 1, 0.5). The virus was labelled with self-quenching concentration of Texas Red-DHPE, and the vesicle lipid compositions are indicated. Cumulative distribution functions corresponding to wait times to individual lipid mixing events for viral fusion with vesicles are shown. It is notable that the “100 mol% mix” sample has also been referred to as “DPhPG mix” in the main text.

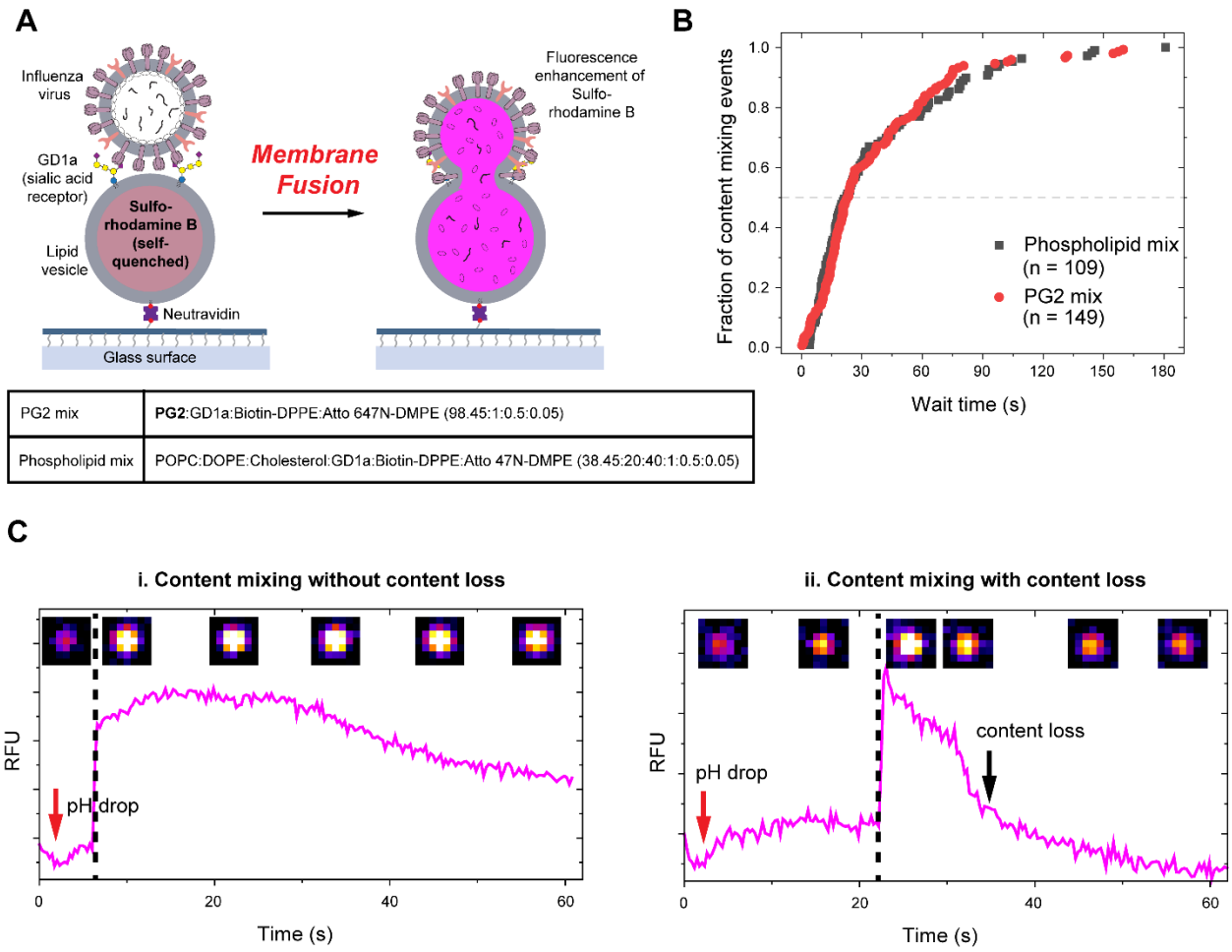

PG2 mix	**PG2**:GD1a:Biotin-DPPE:Atto 647N-DMPE (98.45:1:0.5:0.05)
Phospholipid mix	POPC:DOPE:Cholesterol:GD1a:Biotin-DPPE:Atto 47N-DMPE (38.45:20:40:1:0.5:0.05)

Fig. S13 A. Schematic diagram illustrating content mixing upon fusion of virus particles to tethered lipid vesicles as evident from increase in fluorescence signal of sulforhodamine B dye. **B**. Cumulative distribution functions corresponding to wait times for content transfer events during viral fusion with 100 nm vesicles composed of bipolar lipids ("PG2 mix") and monopolar lipids ("Phospholipid mix"). **C**. Representative fluorescence intensity traces for fusion of "PG2 mix" vesicles with influenza virus particles corresponding to two kinds of events observed: (i) content mixing without any loss (ii) content mixing with content loss.

Supplementary References

(1) Shaw, M.; Kumar, A. Visible-Light-Mediated *β*-C(sp^3)-H Amination of Glycosylimidates: En Route to Oxazoline-Fused/Spiro Nonclassical Bicyclic Sugars. *Org. Lett.* **2019**, *21* (9), 3108–3113.

(2) Eguchi, T.; Arakawa, K.; Kakinuma, K.; Rapp, G.; Ghosh, S.; Nakatani, Y.; Ourisson, G. Giant Vesicles from 72-Membered Macrocyclic Archæal Phospholipid Analogues: Initiation of Vesicle Formation by Molecular Recognition between Membrane Components. *Chem. - A Eur. J.* **2000**, *6* (18), 3351–3358.

(3) Brzustowicz, M. R.; Brunger, A. T. X-Ray Scattering from Unilamellar Lipid Vesicles. *J. Appl. Crystallogr.* **2005**, *38* (1), 126–131.

NMR Spectra

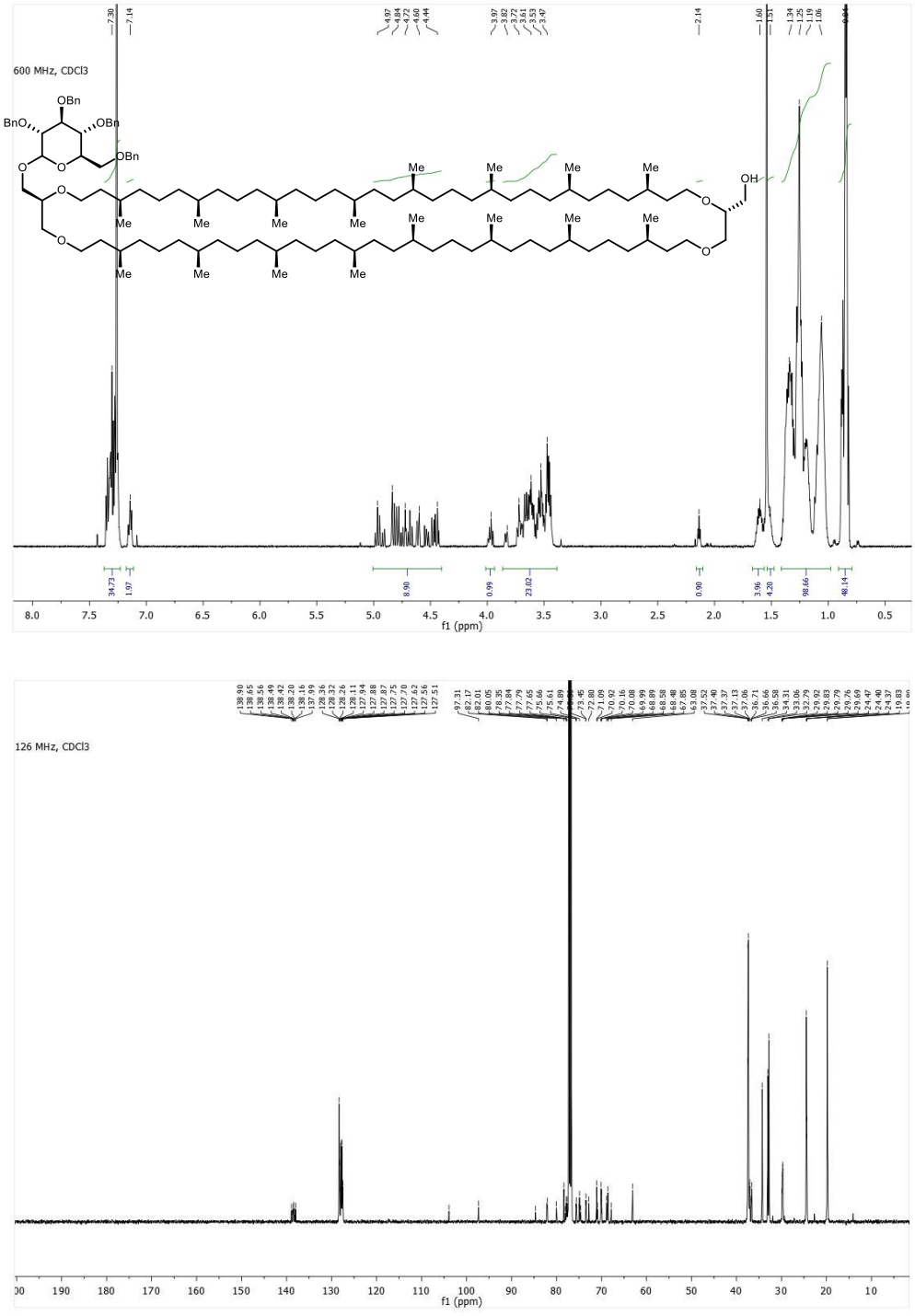

^{1}H NMR (*top*) and ^{13}C NMR (*bottom*) spectra of compound **2**.

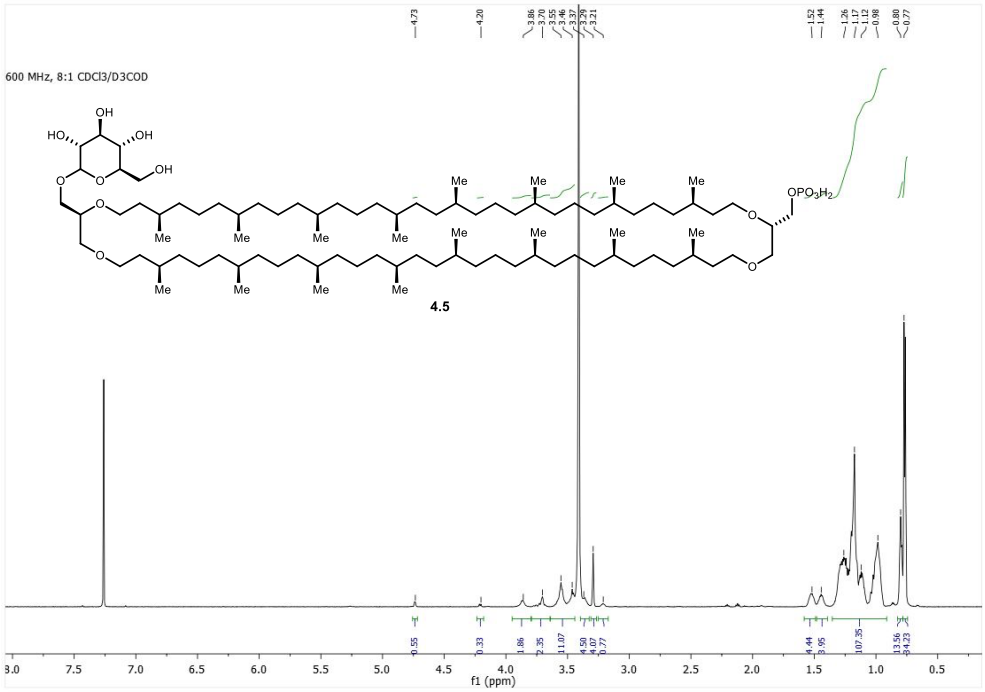

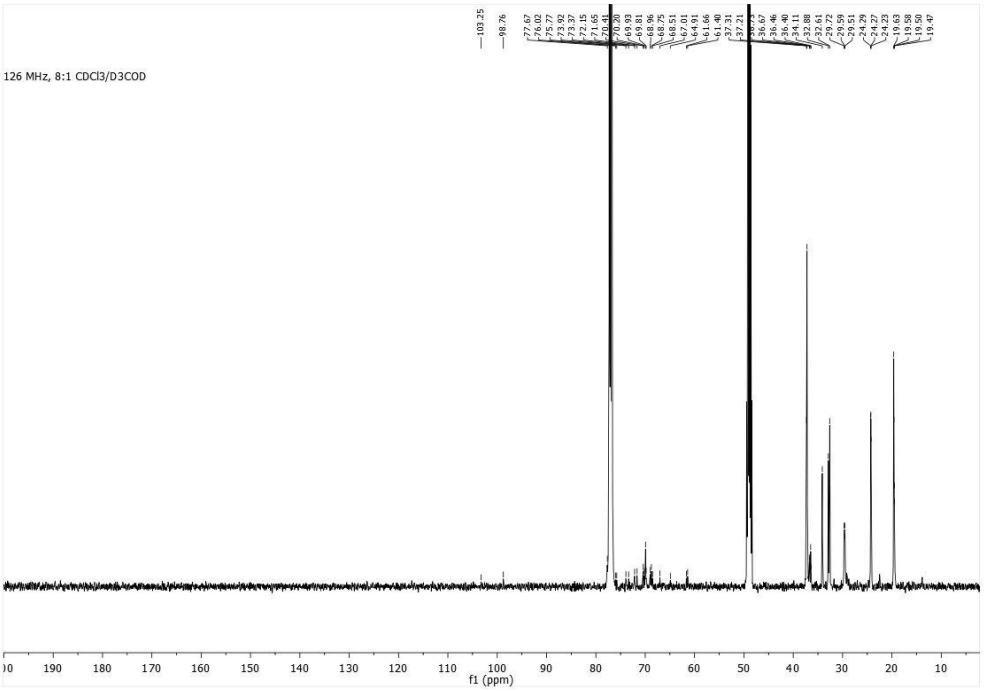

^{1}H NMR (*top*) and ^{13}C NMR (*bottom*) spectra of compound **P1Glc**.

HSQC Data for **P1Glc**:

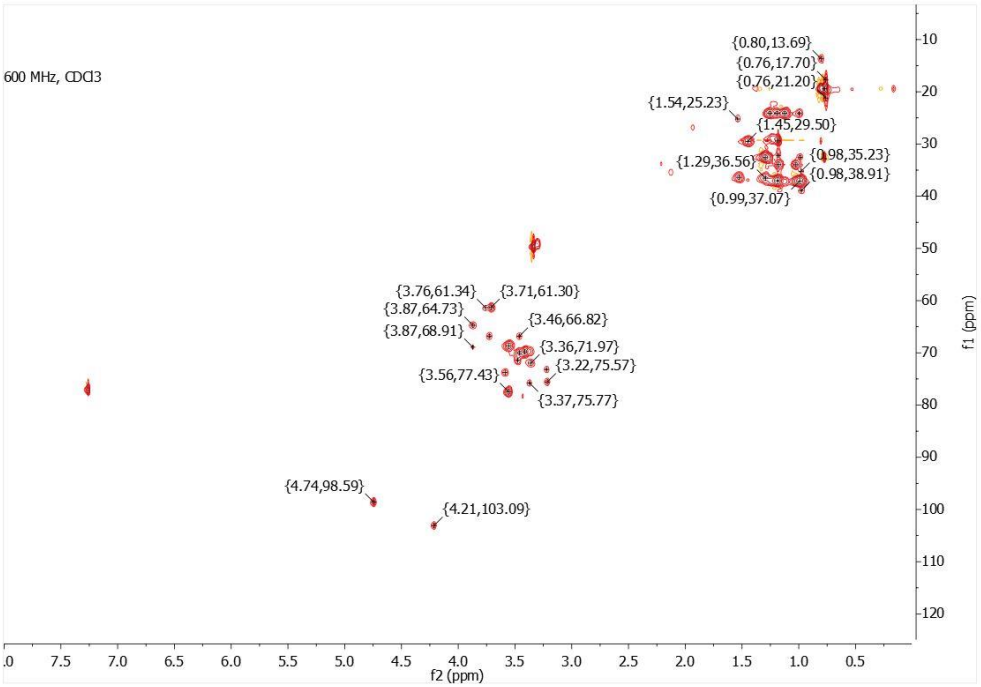

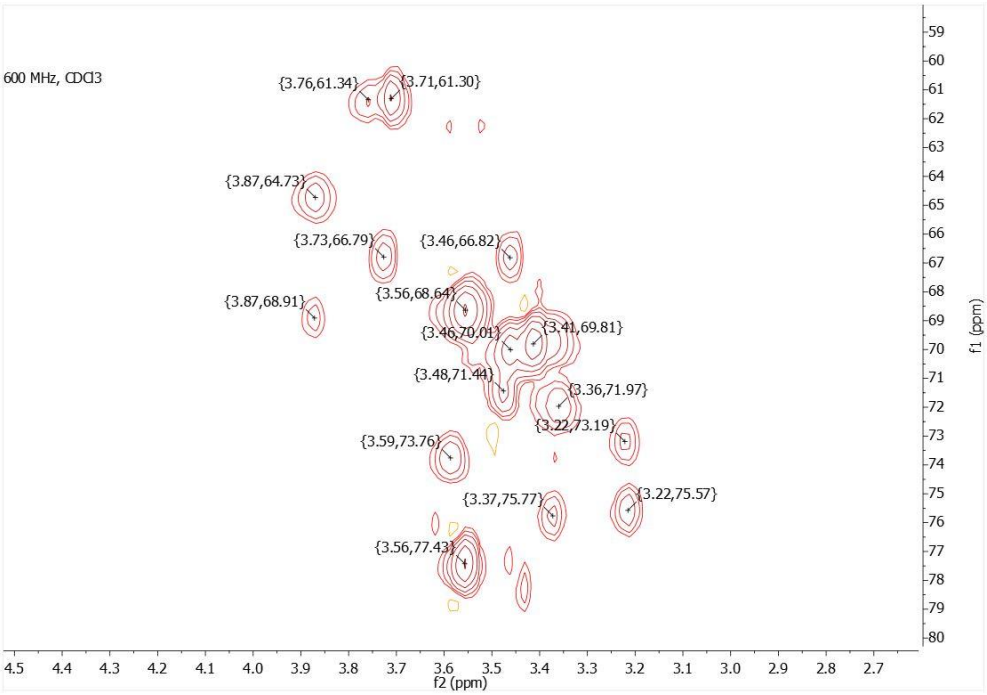

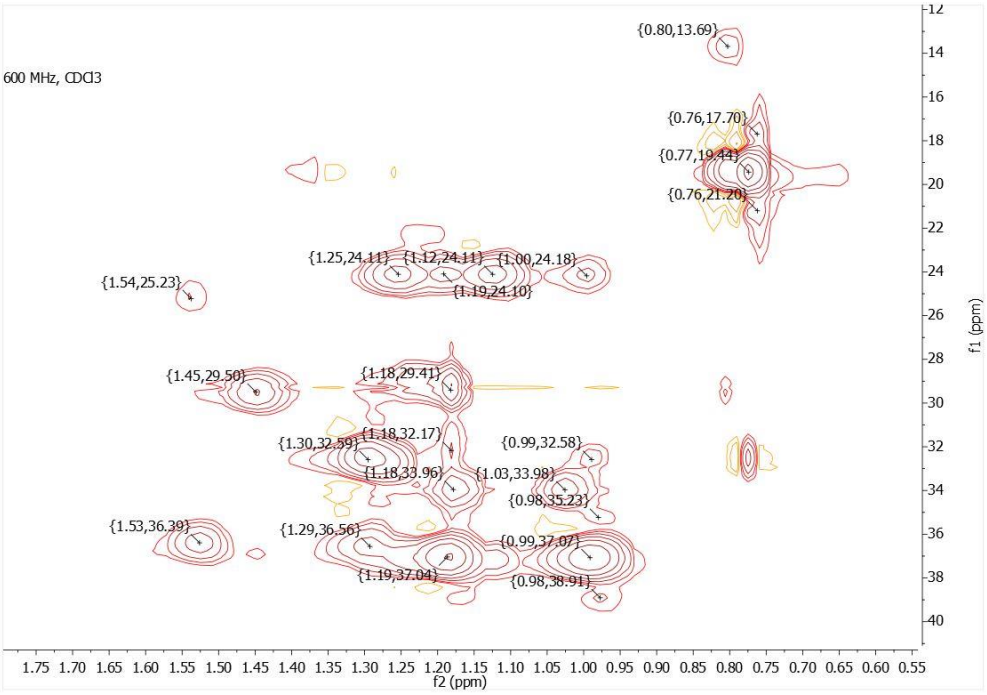

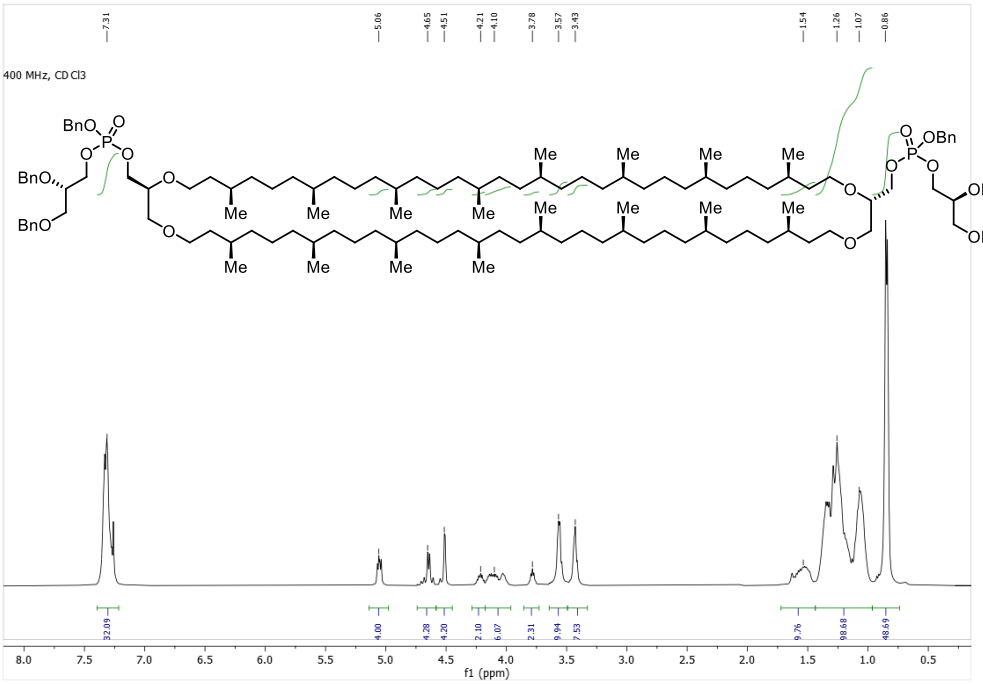

^{1}H NMR spectrum of compound **4.**

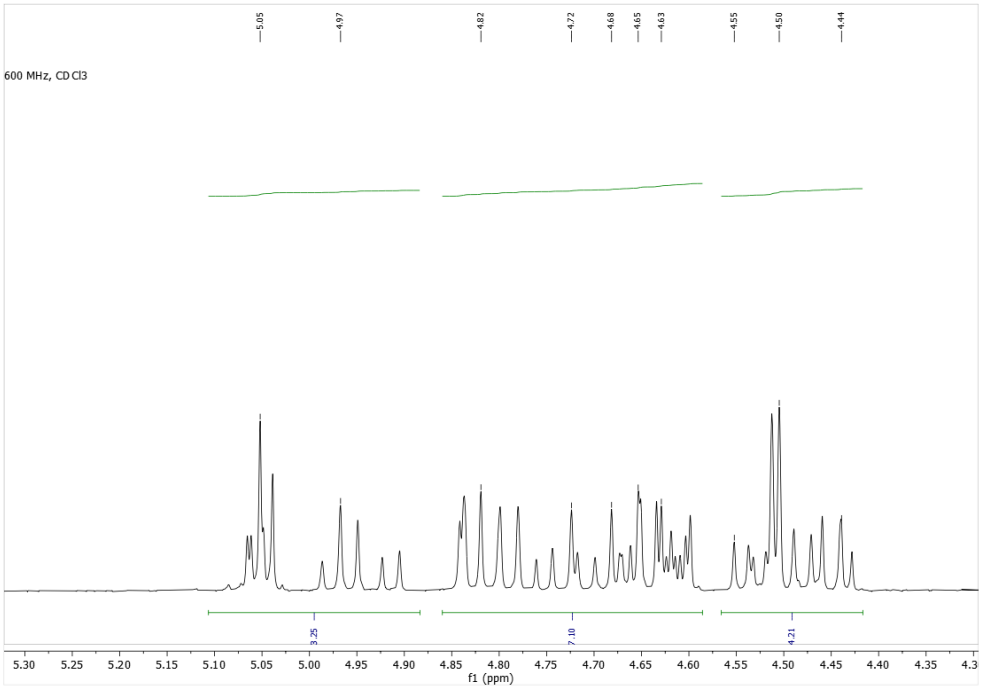

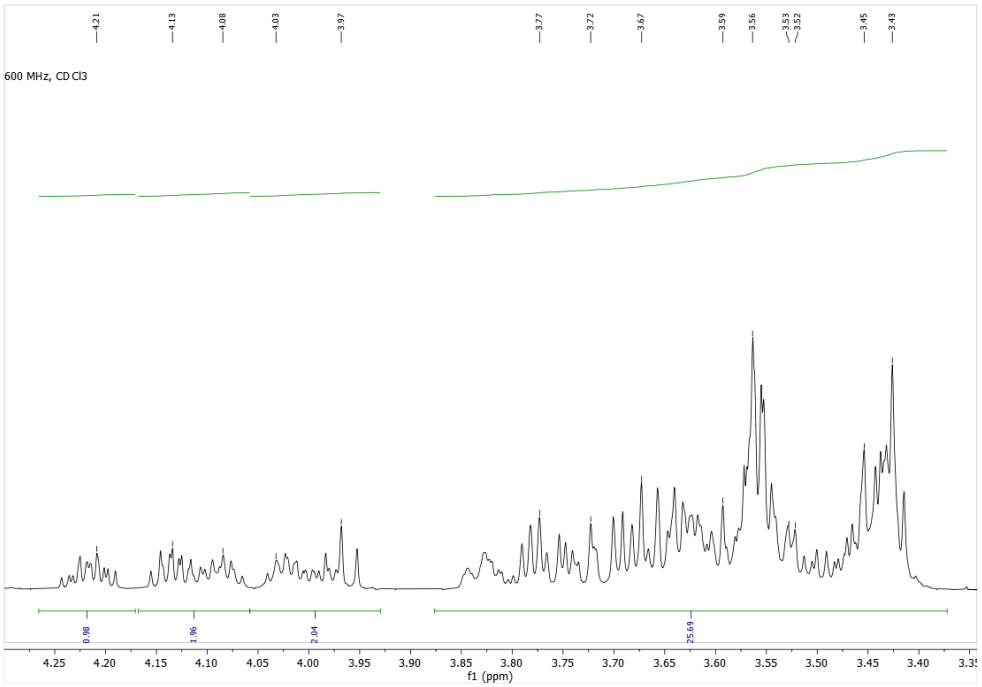

A zoomed in view of the ^{1}H NMR spectrum of compound **4** over δ 5.30-4.30 ppm (*top*) and δ 4.30-3.30 ppm (*bottom*) regions respectively.

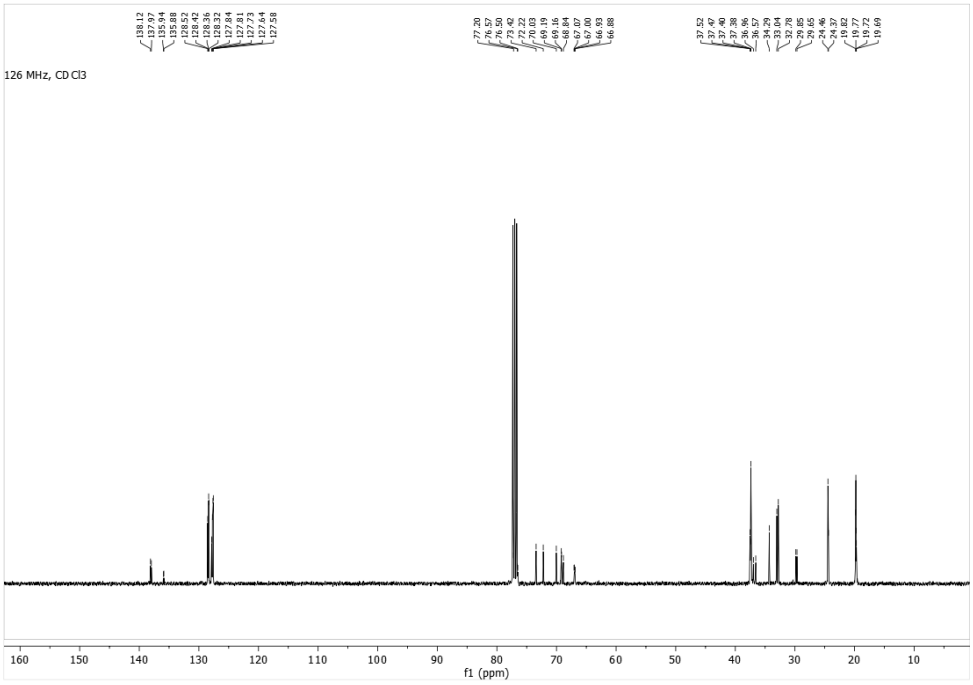

^{13}C NMR spectrum of compound **4**.

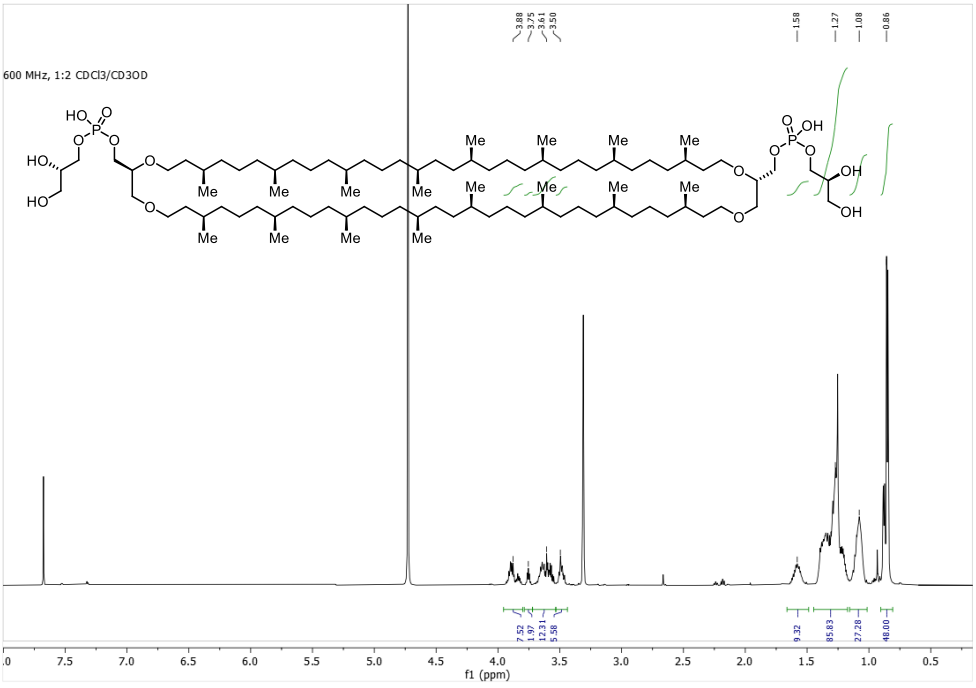

^{1}H NMR spectrum of compound **PG2.**

HSQC Data for **PG2**:

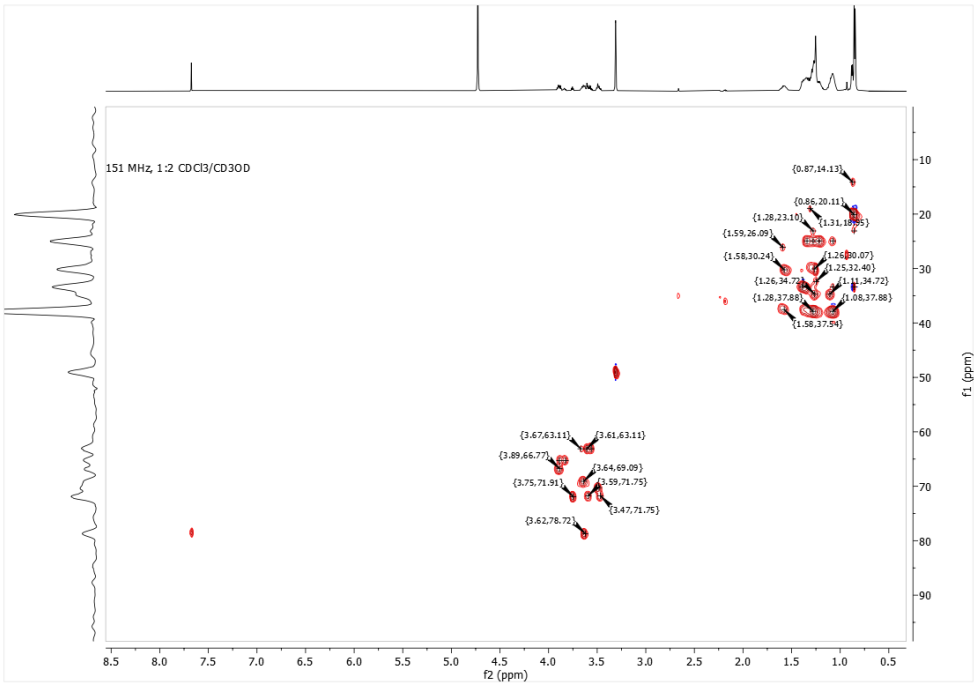

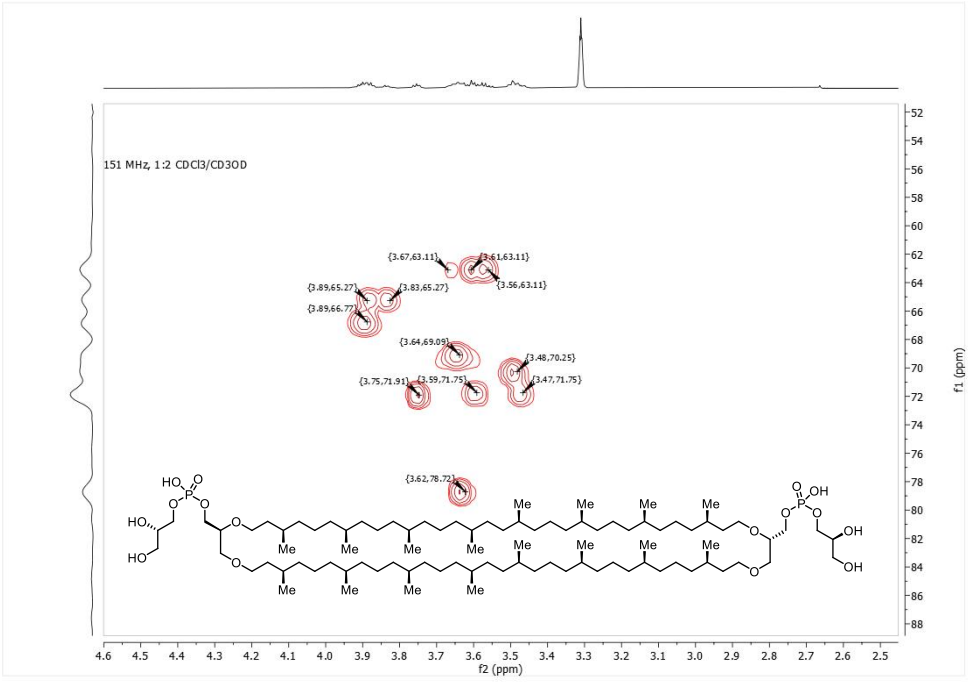

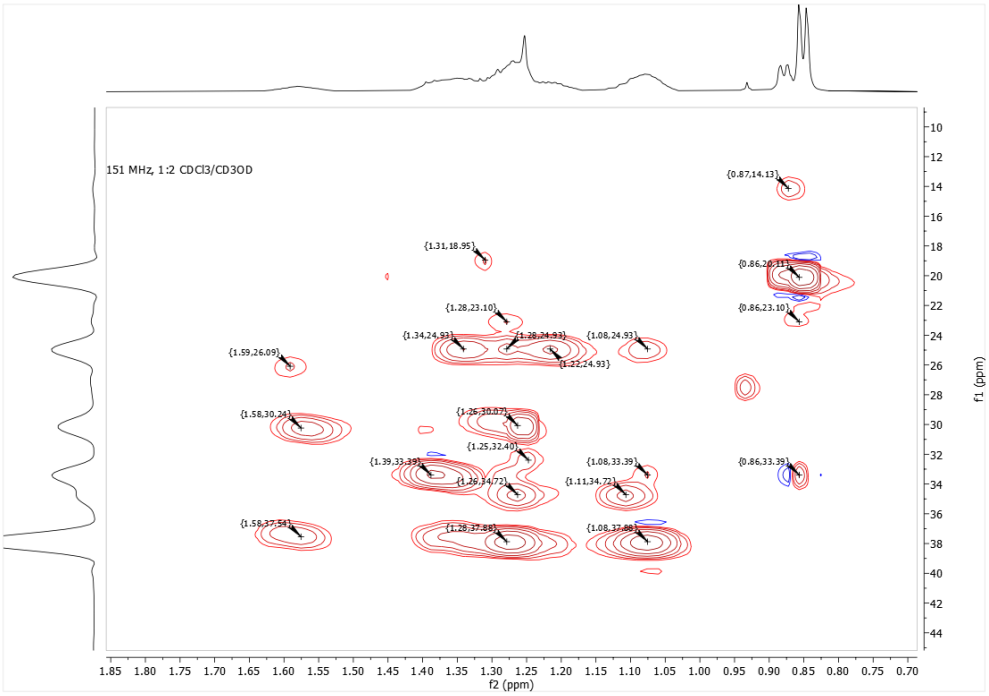

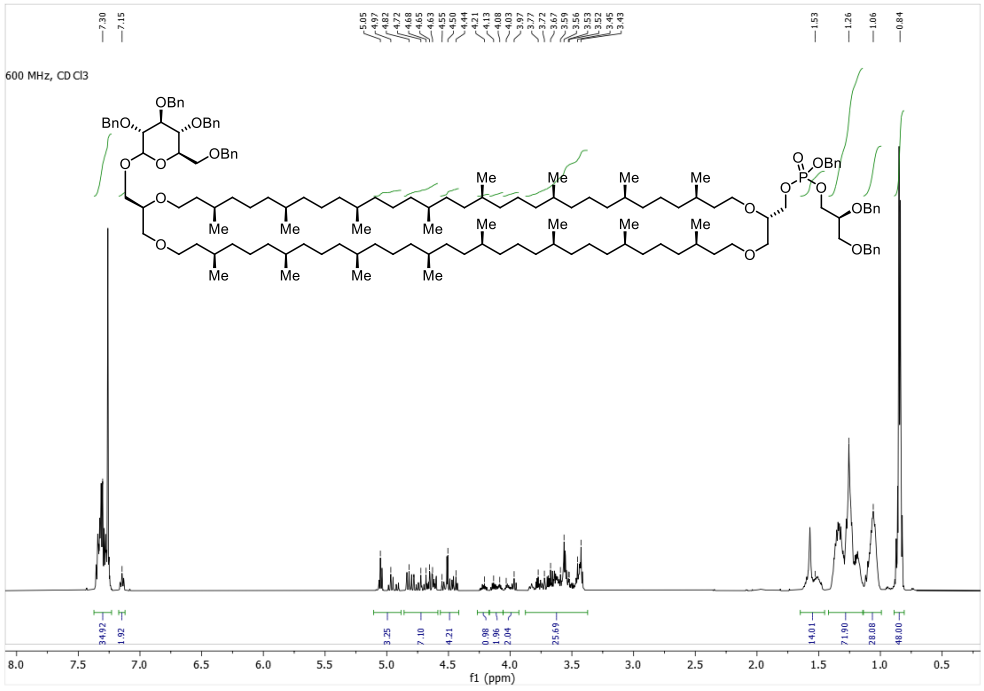

^{1}H NMR spectrum of compound **5**.

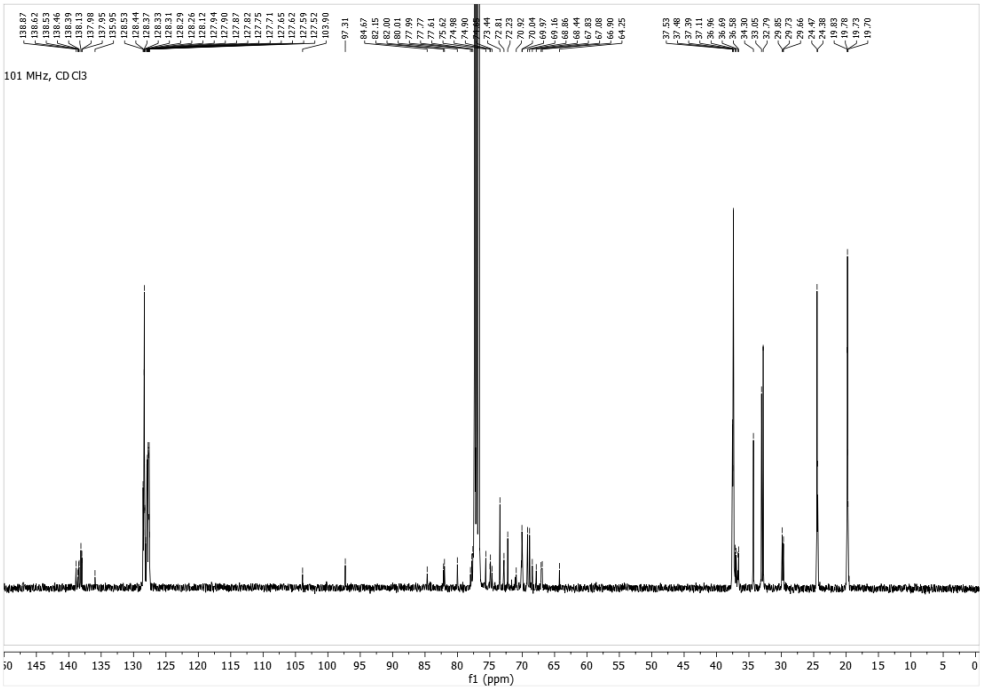

^{13}C NMR spectrum of compound **5.**

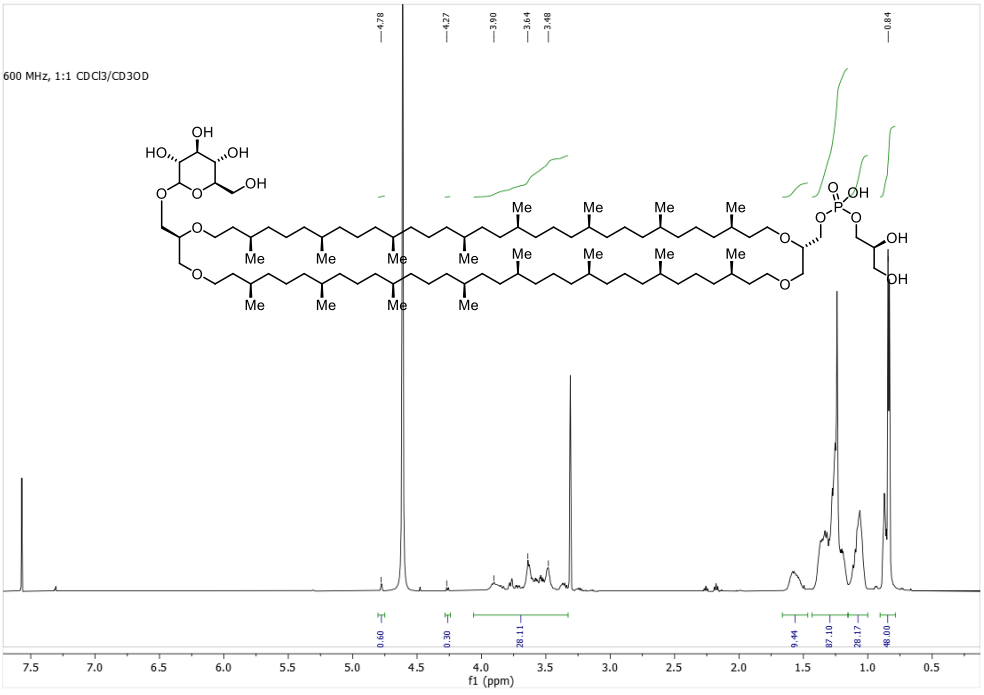

^{1}H NMR spectrum of compound **PG1Glc**.

HSQC Data for **PG1Glc**:

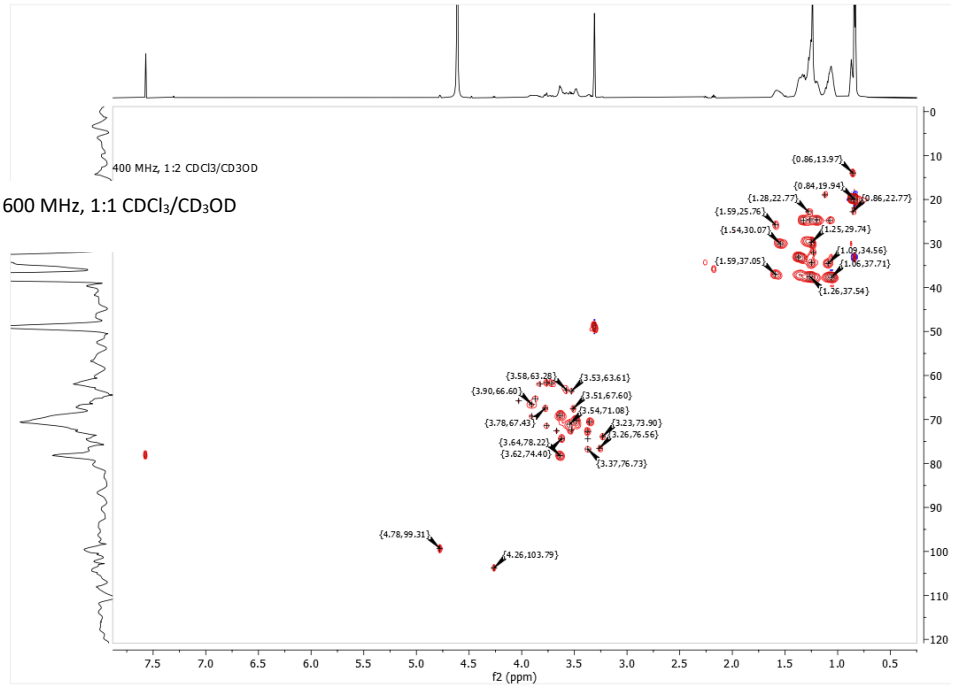

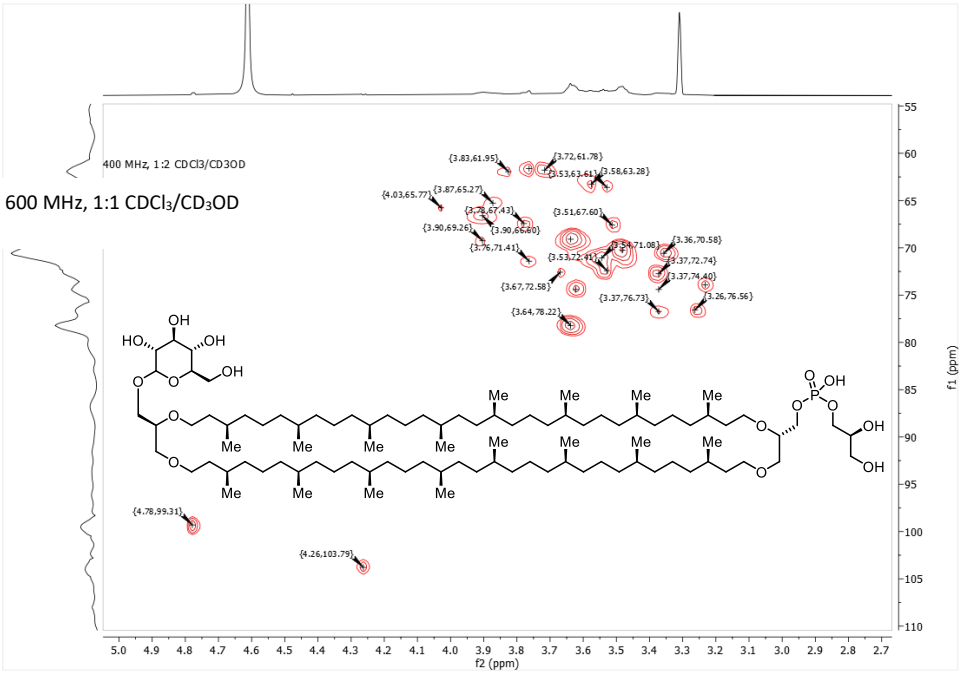

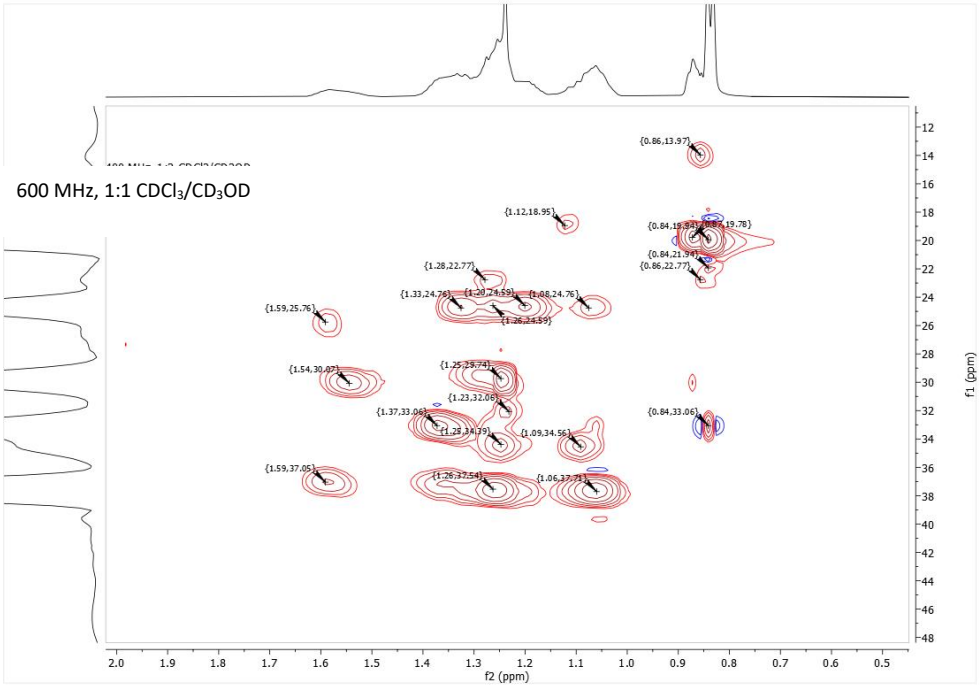

600 MHz, 1:1 $CDCl_3/CD_3OD$